Reaction Current Phenomenon in Bifunctional Catalytic Metal-Semiconductor Nanostructures

BY

MOHAMMAD AMIN HASHEMIAN
B.S., Sharif University of Technology, Iran, 2009

THESIS

Submitted as partial fulfillment of the requirements
for the degree of Doctor of Philosophy in Materials Engineering
in the Graduate College of the
University of Illinois at Chicago, 2015

Chicago, Illinois

Defense Committee:

Eduard Karpov, Chair and Advisor
J. Ernesto Indacochea
Michael McNallan
Didem Ozevin
Alexander Yarin, Mechanical & Industrial Engineering

This thesis is dedicated to my parents for

their endless love, support, and encouragement.

ACKNOWLEDGMENTS

First and foremost, I would like to express my deepest appreciation to my advisor, Dr. Eduard Karpov, for his continuous advice and encouragement throughout the course of this thesis, and especially for his confidence in me. Completing this thesis would have not been possible without his patience, enthusiasm, and immense knowledge.

I would also like to express my sincere gratitude to my thesis committee members, Prof. J. Ernesto Indacochea, Prof. Michael McNallan, Prof. Didem Ozevin, and Prof. Alexander Yarin, for their kind support and invaluable guidance.

I would like to thank National Science Foundation for funding this project. Also I would like to thank Nanotechnology Core Facility (NCF) for help with the preparation of samples. I would like to thank Nathan Ray, who as a good friend was always willing to help and give his best suggestions.

I would also like to thank my parents, brother, and sister. They were always supporting me and encouraging me with their best wishes.

Most importantly, I would like to thank my wife, Jennifer. She was always there cheering me up and stood by me through the good times and bad.

CONTRIBUTION OF AUTHORS

Chapter 1 is a literature review and highlights the significance of my research question.

Chapter 2 describes the experimental work performed to fabricate catalytic metal-semiconductor nanostructures devices (Pt/TiO_2). It also describes the experimental equipments used for measuring the direct conversion of surface released chemical energy into continuous electrical signals.

Chapter 3 represents a published manuscript (*Karpov, E.G., Hashemian, M.A., and Dasari, S.K.: Chemistry-Driven Signal Transduction in a Mesoporous Pt/TiO2 System. Journal of Physical Chemistry C, 117 (30): 15632–15638, 2013*) for which I was the second author. Suhas Dasari assisted me for XRD and SEM images. My research advisor, Dr. Eduard Karpov contributed to the writing of the manuscript.

Chapter 4 represents a published manuscript (*Hashemian, M.A., Palacios, E., Nedrygailov, I.I., Diesing, D., and Karpov, E.G.: Thermal Properties of the Stationary Current in Mesoporous Pt/TiO_2 Structures in an Oxyhydrogen Atmosphere. ACS Applied Materials & Interfaces, 5 (23): 12375–12379, 2013.*) for which I was the first author. Edgar Palacios assisted me for XRD and SEM images. Ievgen Nedrygailov, Detlef Diesing and my research advisor, Dr. Eduard Karpov contributed to the writing of the manuscript.

Chapter 5 represents a published manuscript (*Hashemian, M.A., and Karpov, E.G.: Hydrogen Sensing Behavior of Pt-coated Mesoporous Anodic Titania. Materials Chemistry and Physics, 148(3): 579-584, 2014.*) for which I was the primary author and major driver of the research.

Chapter 6 represents the overall conclusions of this dissertation and includes the future directions of this research.

TABLE OF CONTENTS

CHAPTER **PAGE**

LIST OF TABLES

TABLE **PAGE**

LIST OF FIGURES

FIGURE **PAGE**

LIST OF FIGURES (Continued)

LIST OF FIGURES (Continued)

LIST OF FIGURES (Continued)

SUMMARY

Energy transfer processes accompany every elementary step of catalytic chemical processes on material surface including molecular adsorption and dissociation on atoms, interactions between intermediates, and desorption of reaction products from the catalyst surface. Therefore, detailed understanding of these processes on the molecular level is of great fundamental and practical interest in energy-related applications of nanomaterials. Two main mechanisms of energy transfer from adsorbed particles to a surface are known: (i) adiabatic via excitation of quantized lattice vibrations (phonons) and (ii) non-adiabatic via electronic excitations (electron/hole pairs). Electronic excitations play a key role in nanocatalysis, and it was recently shown that they can be efficiently detected and studied using Schottky-type catalytic nanostructures in the form of measureable electrical currents (chemicurrents) in an external electrical circuit. These nanostructures typically contain an electrically continuous nanocathode layers made of a catalytic metal deposited on a semiconductor substrate.

The goal of this research is to study the direct observations of hot electron currents (chemicurrents) in catalytic Schottky structures, using a continuous mesh-like Pt nanofilm grown onto a mesoporous TiO_2 substrate. Such devices showed qualitatively different and more diverse signal properties, compared to the earlier devices using smooth substrates, which could only be explained on the basis of bifunctionality. In particular, it was necessary to suggest that different stages of the reaction are occurring on both phases of the catalytic structure. Analysis of the signal behavior also led to discovery of a formerly unknown (very slow) mode of the oxyhydrogen reaction on the Pt/TiO_2(por) system occurring at room temperature. This slow mode was producing

surprisingly large stationary chemicurrents in the range 10-50 $\mu A/cm^2$. Results of the chemicurrent measurements for the bifunctional Pt/TiO_2(por) transducers were unusual in many regards. Addition of various H_2 amounts to the initial 160 Torr O_2 atmosphere over the sample led to well repeatable chemicurrents of both transient and steady-state characters, depending on a specific H_2 addition procedure.

It is suggested that adsorption of hydrogen on Pt/TiO_2 structures leads to dissociation of hydrogen molecules on Pt surface followed by "spillover" of hydrogen atoms from Pt toward TiO_2 support. In contrast to oxygen, hydrogen manifests donor properties by giving electrons to the TiO_2 conductance band and adsorbing as H^+ ions. This effect is well illustrated with the I-V curves, showing highly conductive Ohmic characteristics of the samples in H_2 atmosphere. Two versions of the spillover process leading eventually to H^+ ion adsorption on TiO_2 will be considered: H-atom and proton (pre-ionized H-atom) spillover.

This research work is a pioneering effort to challenge the direct utility of the non-adiabatic electronic processes in catalytic nanomaterial systems, paving the road toward novel energy conversion devices, solid-state chemical sensors and signal transducers.

CHAPTER 1

LITERATURE REVIEW

1.1 Renewable Versus Non-renewable Energy

Although there are many ways to classify energy, it is broadly categorized into two groups: non-renewable and renewable. Non-Renewable energy sources such as natural gas, oil, coal, etc supply 80 % of total world energy demands (Abuelnuor et al. 2014). These sources are taken from sources that exist on the earth in limited volumes and consequently at risk of complete consumption. One of the most significant disadvantages with the use of non-renewable energy is that it is not environmentally friendly. When it is burnt, carbon emission is released into the atmosphere that can have serious effects on human health and global warming. It has been reported that 98% of carbon emission is due to burning of fossil fuels (Balat et al. 2009). Also, the concentration of carbon dioxide has been increased from 280 to 370 ppm over the last decades (H. Lund 2007).

In recent years, renewable energies (also known as alternative sources of energy) have attracted much attention as alternative sources of energy that can replace fossil fuels (Brennan and Owende 2010; Balat 2011). Renewable energies can be generated from many natural sources and can be used over and over without being depleted. These sources are available in the abundant quantity and produce no pollutants into the environment; therefore they are considered as clean energies. Many renewable energy sources can be utilized instead of conventional fossil fuels. Presently, the sources of renewable energy include sunlight, geothermal, tides, hydropower, wave, wind and

biomass which are mostly used in electricity generation, heating and motor fuels. Tidal energy is harnessed by generators that utilize the flow of water controlled by tidal streams. Although this type of energy is not widely used, it is an ideal energy source for island countries (Charlier 2003). In addition, generation of electricity can be achieved when the energy of ocean surface waves is captured by a wave energy converter. Wind power can be converted to electricity or mechanical energy through wind turbines. To date about 2% of worldwide electricity is provided by the wind turbines (Pazheri et al. 2014). Hydropower is used for generation of hydroelectricity via either the movement of water through rivers and lakes or the potential energy of falling water. Hydropower systems are constructed on small and large scales. Due to policies and regulations in many countries, small-scale hydropower stations are preferred in rural areas whereas large-scale hydropower is utilized when massive production of electricity is needed (Koutsoyiannis 2011). Geothermal energy is a reliable way to take advantage of the thermal gradients between the earth's surface and core. At a geothermal power plant, underground reservoirs of hot water or steam are transported to the surface through a well under high pressure. Due to its cleanness and sustainability, geothermal energy is used in applications such as geothermal heat pumps, space heating, greenhouse heating, aquaculture ponds, agricultural crop drying, and snow melting (Lund et al. 2005). Biomass energy refers to any living or recently living plant and animal materials that can be used for heat and power generation through thermal, chemical, and biochemical processes such as combustion, gasification, and pyrolysis (Gebreegziabher et al. 2014). It has been postulated that biomass has the global potential to become one of the most powerful and efficient sources of renewable energy in both industrialized and developing

countries during the next century (Fischer and Schrattenholzer 2001; Berndes et al. 2003). Direct combustion of wood, leaves and animal waste for non-commercial uses, i.e. cooking and space heating, refers to traditional biomass energy whereas conversion of biomass to biofuels (solid, liquid, or gas fuels) for electricity generation or transportation is called modern biomass energy (Faaij 2006). The direct conversion of sunlight to electricity through photovoltaic (PV) cells is being considered as one of the fastest growing renewable energy technologies (Ginley et al. 2008). Photovoltaic cells are prepared by forming a junction between n-type and p-type semiconductors, where n-type denotes semiconductors in which majority carriers in the conduction band are electrons and p-type represents semiconductors in which majority carriers in the valance band are holes. A potential energy barrier exists at the interface between the n-type and p-type semiconductors (p/n junction). There are four different types of energy barriers: homojunctions, heterojunctions, heteroface structures, and Schottky barriers. In homojunctions and heterojunctions, p/n junctions are created within the same semiconductor and between different semiconductor materials, respectively. Heteroface structures are similar to homojunctions but with larger bandgap semiconductors. A Schottky barrier is a metal-semiconductor junction. The conversion of sunlight into electricity in a photovoltaic solar cell is based on four major processes (Dhankhar et al. 2014):

- Absorption of photons from sun light.
- Generation and transport of electron-hole pairs (charge carriers) in a semiconductor.
- Separation of charge carriers by the potential energy barrier.
- Collection of electron-hole pairs at the solar cell contact.

Although 80% of the solar energy is absorbed by solar cells, only a fraction of the absorbed energy can be converted into electricity. In the past few years, most efforts have focused on improving the performance of solar cells (Pala et al. 2009; Bhaumik et al. 2014). Depending on the semiconductor materials used in the manufacturing of solar cells, their theoretical efficiency can reach 86% under high intensity light (Makki et al. 2015). However, commercial solar cells have energy conversion efficiencies between 15 and 25% (Günes and Sariciftci 2008).

To date, three generations of solar cells have been introduced to the market. In 1954, the first generation solar cells, also known as conventional cells, were introduced (Chapin et al. 1954). They are based on crystalline silicon (i.e. monocrystalline, polycrystalline, and ribbon). Due to their high efficiency (15−20%), these types of photovoltaic cells commercially dominate the solar cell technology, accounting for more than 86% of the solar cell market. However, they require expensive manufacturing processes (Green et al. 2012). In order to reduce the production costs, the second generation solar cell technologies were introduced to the market (Shah et al. 2004; Chopra et al. 2004). They are based on thin film technology, namely amorphous silicon, cadmium telluride (CdTe), and copper indium gallium selenide (CGIS). Most thin film solar cells are about 2−3% less efficient compared to silicon wafer-based cells (Shalav et al. 2007). Improving the efficiency and reducing manufacturing costs of existing solar cells have been the topics of research in the past few years. These efforts led to the advent of third generation solar cells (Snaith 2013). Presently, the third generation technologies include: nanocrystal, photo electrochemical, solid state dye-sensitized, polymer, quantum dot-sensitized, nanoparticle sensitized semiconductors, and organic-inorganic hybrid

solar cells (Yang et al. 2014). However, relatively low efficiency of these types of solar cells renders them unable to compete commercially with the current silicon-based cells and thin film technologies. For example, the power conversion efficiency of quantum-dot-sensitized solar cells (QDSSCs) is only 6% (Pan et al. 2013).

Among all renewable energy sources mentioned above, solar energy is one of the most promising energies because it is abundant and inexhaustible (Ludin et al. 2014). However, high manufacturing and installation costs and complicated technology have constrained wide-spread implementations of solar cells. As a result, the last decades have seen a renewed interest in other solid-energy conversion devices such as fuel cells, thermoelectric, and thermionic generators.

1.1.1 Principle Mechanism and Types of Fuel Cells

Development of fuel cells is being considered as one of the most important aspects of material science and engineering (Chandan et al. 2013). Fuel cells are used in a broad range of applications, namely portable power generation, transportation, stationary power generation, and mobile technologies (laptop computers, cellular phones, etc.) (Kerres 2005). A fuel cell is an electrochemical conversion device that converts the chemical energy into electrical work via a chemical reaction between a fuel (hydrogen, natural gas, or methanol) and an oxidizing agent (oxygen, air, or hydrogen peroxide) (Winter and Brodd 2004). Most commercial fuel cells operate with hydrogen and oxygen gases. Since water is the only by–product of this reaction, fuel cells have a significant contribution in reducing greenhouse carbon dioxide emissions. Also, in contrast to conventional fossil fuels, no combustion is required for production of electricity in fuel

cells. Similar to batteries, in fuel cells electrical energy is produced through oxidation-reduction (redox) reactions at the boundary of electrode/electrolyte interface. Fuel cells are open systems where the reactants are supplied externally. This means that fuel cells are able to continuously generate electricity as long as hydrogen and oxygen sources are supplied to the electrodes. However, batteries are closed systems in which chemical energy is stored inside of batteries. Once this stored chemical energy is consumed, batteries should be recharged (i.e. lead-acid, lithium ion, nickel cadmium, etc.).

Each fuel cell consists of an electrolyte and two electrodes: an anode (negative electrode) and a cathode (positive electrode). The electrodes are separated by the electrolyte and connected via an external circuit. At the anode, hydrogen molecules are separated into protons and electrons. The electrolyte allows only protons to pass through it to the cathode. The electrons must move along an external circuit, producing electricity. At the cathode, the electrons react with protons and oxygen molecules, generating water and heat. The electrode reactions and overall fuel cell reaction are as the following:

$$\text{anode:} \qquad H_2 \rightarrow 2H^+ + 2e^- \qquad (1\text{-}1)$$

$$\text{cathode:} \qquad O_2 + 4H^+ + 4e^- \rightarrow 2H_2O \qquad (1\text{-}2)$$

$$\text{overall:} \qquad O_2 + 2H_2 \rightarrow 2H_2O \qquad (1\text{-}3)$$

Fuel cells are generally classified by their operating temperature and the chemical properties of the electrolyte they use (Lucia 2014). Table I shows the most common types of fuel cells.

Table I. Fuel cells classification (Lucia 2014)

Fuel cell type	Operating temperature (˚C)	Electrolyte	Electrodes	Catalyst	Interconnect	Charge carrier
Polymer electrolyte membrane	40–80	Hydrated polymeric ion exchange membrane	Carbon	Platinum	Carbon or metal	H^+
Alkaline	65–220	Mobilized or immobilized potassium hydroxide in asbestos matrix	Platinum	Platinum	Metal	OH^-
Phosphoric acid	205	Immobilized liquid phosphoric acid in SiC	Carbon	Platinum	Graphite	H^+
Molten carbonate	650	Immobilized liquid molten carbonate in $LiAlO_2$	Nickel and nickel oxide	Electrode material	Stainless steel or nickel	CO_3^+
Solid oxide	600–1000	Perovskites (ceramics)	Perovskite and perovskite/metal cermet	Electrode material	Nickel, ceramic or steel	O^-

Alkaline fuel cells (AFCs), polymer electrolyte membrane fuel cells (PEMFCs), and phosphoric acid fuel cells (PAFCs) are known as low-temperature fuel cells because they operate at temperatures less than 220˚C. The high-temperature fuel cells include molten carbonate fuel cells (MCFCs) and solid oxide fuel cells (SOFCs) that operate at temperatures above 650˚C. It has been shown that high-temperature fuel cells are generally more efficient than low-temperature fuel cells (Tomczyk 2006). AFCs use potassium hydroxide (KOH) as the alkaline electrolyte which enhances the oxygen reduction compared to acid fuel cells. The concentration of KOH is usually in the range of 30−45 wt%. The formation of carbonates resulting from the interaction between the electrolyte and CO_2 in air can significantly reduce the performance of AFCs (Geeter et al. 1999). This reaction can be shown as the following:

$$CO_2 + 2OH^- \rightarrow (CO_3)^{2-} + H_2O \qquad (1\text{-}4)$$

The electrolyte in PEMFCs is an acidic polymer membrane which conducts only protons. On the other hand, neither electrons nor gasses are allowed to pass through the electrolyte. Low operating temperature (40−80˚C) and high power density (20−250 kW) are the main advantages of PEMFCs. These features are being utilized for the power sources in various modes of transportation, including light-weight vehicles, buses, etc. (Wang et al. 2011). Recently, TiO_2 composite membrane use has been reported as a new technology for improving the performance of PEMFCs (Abdullah and Kamarudin 2015). PEMFCs containing TiO_2 have higher proton conductivity compared to the conventional PEMFCs. Also, these modified PEMFCs have higher thermal resistivity and stability and they can be used at elevated temperatures (up to 250˚C) (Gandhi et al. 2012).

PAFCs, which use phosphoric acid as the electrolyte, were the first commercial fuel cells (Ellis et al. 2001). They are primarily used in stationary power generators with output in the 5 to 20 MW range (Carrette et al. 2001). The electrical efficiency of PAFCs is about 37%, but it can be increased up to 70% when they are used in combined heat and power applications (Sammes et al. 2004).

MCFCs usually use molten LiK or LiNa carbonates as the electrolyte which is suspended by a ceramic matrix such as $LiAlO_2$. Stationary power plants and heat cogeneration are their main applications (Buonomano et al. 2015). In contrast to low-temperature fuel cells that use hydrogen as fuel, other types of fuels such as natural gas, methane, and biogas can be used in MCFCs. Also, porous nickel as an anode and porous nickel oxide (NiO) as a cathode are used in MCFCs instead of noble metals (Minh 1988). It has been reported that doping of nickel with Cr or Cu can improve the stability and creep resistance of the cathode (Dicks 2004). One of the disadvantages of MCFCs is the dissolution of nickel oxide in the electrolyte due to operating at high temperatures (650˚C). The use of additives such as MgO, $BaCO_3$, and $SrCO_3$ has been suggested to reduce the solubility of NiO in molten metal carbonates (Scaccia 2005). When MCFCs are combined with other electric generators, their efficiency can be reached up to 50% (Carrette et al. 2001).

SOFCs use a solid oxide material as the electrolyte instead of a liquid electrolyte. This electrolyte conducts oxygen ions (O^{2-}) that are reduced at the cathode. Yttria-stabilized zirconia (YSZ) is the most commonly used ceramic for the electrolyte due to its high ionic conductivity, mechanical strength, and chemical stability at elevated

temperatures (Ormerod 2003). Unlike low-temperature fuel cells which require separate fuel processors to produce hydrogen needed for fuel cells, in SOFCs internal reforming of hydrocarbon fuels (catalytic conversion of a hydrocarbon fuel to H_2 and CO) can be directly obtained on the anode. This is due to their elevated operation temperatures of 600−1000˚C. H_2 and CO produced from internal reforming are oxidized to H_2O and CO_2, generating electricity and high temperature heat. Furthermore, this heat can be used in a gas turbine or a combined heat and power system, increasing the overall efficiency of SOFCs. The basic reactions described above can be shown as the following:

cathode: $O_2 + 4e^- \rightarrow 2O^{2-}$ (1-5)

anode: $H_2 + O^{2-} \rightarrow H_2O + 2e^-$ (1-6)
$CO + O^{2-} \rightarrow CO_2 + 2e^-$

overall: $H_2 + O_2 + CO \rightarrow H_2O + CO_2 + Heat$ (1-7)

1.1.2 Thermoelectric and Thermionic Generators

Thermoelectric (TE) generators are another type of solid-state device that converts thermal energy directly into electrical energy by employing temperature gradients across low bandgap semiconductors. TE generators are composed of p-type and n-type semiconductors that are connected electrically in series. Figure 1.1 shows the schematic of a thermoelectric generator. When a temperature difference is applied to the junctions of n-type and p-type materials, charge carriers (electrons and holes) are driven from the hot side (T_h) to the cold side (T_c) of a TE generator. The diffusion of charge

carriers produces electricity through an external load. This physical process is widely known as Seebeck effect.

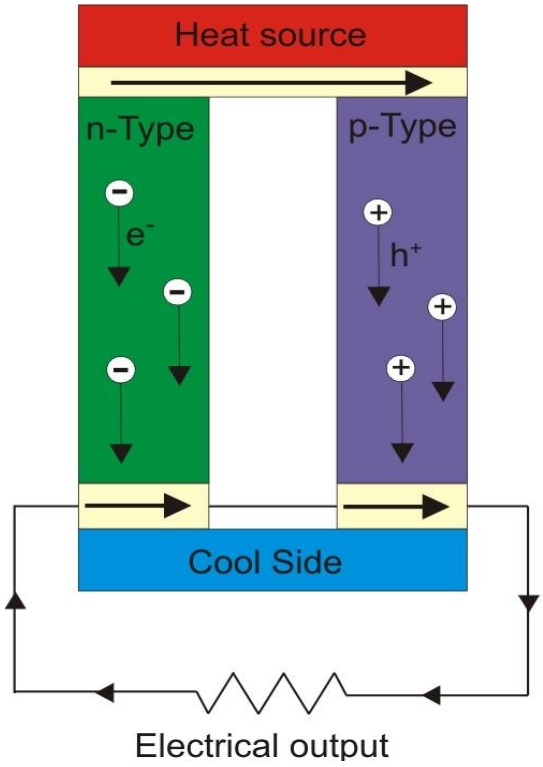

Figure 1.1. Schematic of a thermoelectric generator made of n-type and p-type semiconductors

The efficiency of a thermoelectric generator is expressed as (Snyder 2008):

$$\eta = \frac{\Delta T}{T_h} \cdot \frac{\sqrt{1+ZT}-1}{\sqrt{1+ZT}+T_c/T_h} \tag{1-8}$$

where $\Delta T/T_h$ and ZT are the Carnot efficiency and figure of merite of TE materials, respectively. ZT is a dimensionless parameter that expresses the performance of

thermoelectric materials. It relies directly on material properties and operation temperature as the following:

$$ZT = \frac{\alpha^2}{\rho\kappa} T \tag{1-9}$$

where α is the is the Seebeck coefficient of the material ($V \cdot K^{-1}$), ρ is the electrical resistivity of the material (Ω·m), κ is the thermal conductivity of the material ($W \cdot m^{-1} \cdot K^{-1}$), and T is the absolute Temperature (K). Older TE materials such as bismuth telluride alloys (Bi_2Te_3) have a ZT of about 1 that can provide the efficiency of only 4−7% (Sofo and Mahan 1994). The efficiency of thermoelectric generators can be improved by increasing ZT of TE materials. One method to acquire this result is to increase the Seebeck coefficient by using nano-structured, nanowires, thin-film superlattice, and quantum well materials (Snyder and Toberer 2008). Recent advances in the field of thermoelectric materials have demonstrated that materials with ZT above 2 can increase the TE generators efficiency up to 15 % (Baranowsk et al. 2014). Due to their low efficiency, to date thermoelectric generators have not been able to compete commercially with other solid-state devices in energy conversion applications. Instead, they have been limited to harvesting high temperature energy through the recovery of industrial waste heat in small-scale applications (Wang et al. 2014).

Thermionic generators, similar to thermoelectric devices, use a temperature difference to convert thermal energy into electricity. A thermionic generator consists of two electrodes: an emitter cathode and a collector anode. When the cathode is heated to a sufficiently high temperature, it will emit high energy electrons. This process is known as

thermionic emission. These hot electrons ballistically move over the internal potential barrier toward the cold anode (Humphrey et al. 2005). The potential barrier between the hot cathode (with a high work function) and the cold anode (with a low work function) is used to separate the electric charge. Although both thermionic and thermoelectric generators utilize a temperature gradient for generation of high energy electrons, thermionic generators are generally more efficient than thermoelectric devices due to their different current flow mechanisms. In thermionic generators, the movement of electrons is ballistic whereas the current flow in thermoelectric generators is diffusive (Mahan et al. 1998; Xuan and Li 2003).

A great research effort has been devoted to employ internal thermionic emission into the thermoelectric materials via development of semiconductor superlattice nanostructures (Whitlow and Hirano 1995; Hyldgaard and Mahan 1997; Zeng et al. 2006). It has been demonstrated that the intrinsic potential barrier of heterogeneous metal-semiconductor structures can serve as a filter to selectively pass only electrons with high energy. Consequently, phonons and lower energy electrons are prevented from going ballistically over the barrier. This internal potential barrier combined with Seebeck effect can significantly enhance the efficiency of thermionic generators. The thermionic current per unit area can be calculated using the Richardson equation (Lough et al. 2001):

$$J=AT^2\exp(\frac{-W}{k_BT}) \tag{1-10}$$

where A = 120 A/cm^2 K^2 is the effective Richardson constant, T is the temperature, W is the work function of the metal and k_B is the Boltzmann constant. Since all electrons are in thermal equilibrium, increasing the work function (potential barriers) of the metal will reduce the thermionic emission current in accordance with the Richardson equation.

1.2 Electronic Excitations Induced by Exothermic Reactions on Catalytic Metal Surfaces

Energy can be dissipated into electronic levels of a metal surface via exothermic chemical processes, inducing the following primary electronic excitations (Greber 1997; Nienhaus 2002):

- Phonons emission
- Photons or surface chemiluminescence
- Exoelectrons emission into vacuum
- Electron-hole (e-h) pairs

Phonons energies are much smaller compared to chemical energies. This implies that phonons should be excited in multiple excitation steps for the direct dissipation of energy. The direct transfer of the chemical energy into the phonons system of the metal is called *adiabatic* process. When the electronic subsystem of a metal is excited through exothermic reactions, electrons or photons with energies greater than the metal work function can leave the metal surface. The emission of excited electrons and photons are referred to as exoelectron emission and surface chemiluminescence, respectively. Also, exothermic surface reactions may lead to the creation and ballistic traverse of electron-

hole pairs in metals. These electronic excitations are known as *nonadiabatic* processes (Bottcher et al. 1990). Figure 1.2 illustrates the schematic of these elementary excitations for an exothermic reaction (adsorption process).

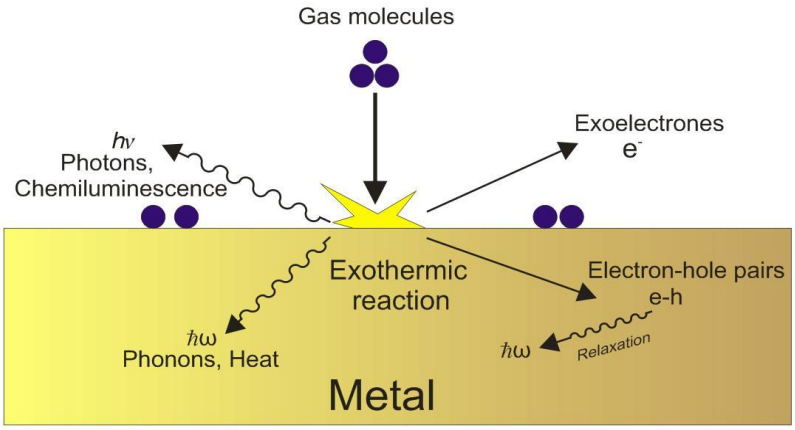

Figure 1.2. Schematic of elementary excitations in a metal including exoelectrons, photons, phonons, and electron-hole pairs (Nienhaus, H 2002)

The direct detection of exoelectron emission and surface chemiluminescence has been challenging for a long time because they can only be excited in a metal with a work function less than 3 eV, while most catalytic metals have higher work functions. One example of exoelectron emission is the reaction of halogen gases with alkali metals (Böttcher and Niehus 2001). However, the detection of excited electrons or holes by the use of metal-semiconductor structures (Schottky diodes) has gained much attention in the past few years (Nienhaus 2002; Park et al. 2007; Karpov et al. 2013). In particular, hot electrons and hot holes with energies larger than the Schottky barrier can be detected in n-type and p-type semiconductors, respectively. In the n-type semiconductor, the Schottky barrier height (Φ_n) is defined as the difference between the interfacial

conduction band minimum and the Fermi energy. In the p-type semiconductor, the Schottky barrier height (Φ_p) is the difference between the valance band maximum and the Fermi level at the interface. The principle of hot charge carriers is schematically depicted in Figure 1.3. In the following sections, the properties of these hot charge carriers will be discussed.

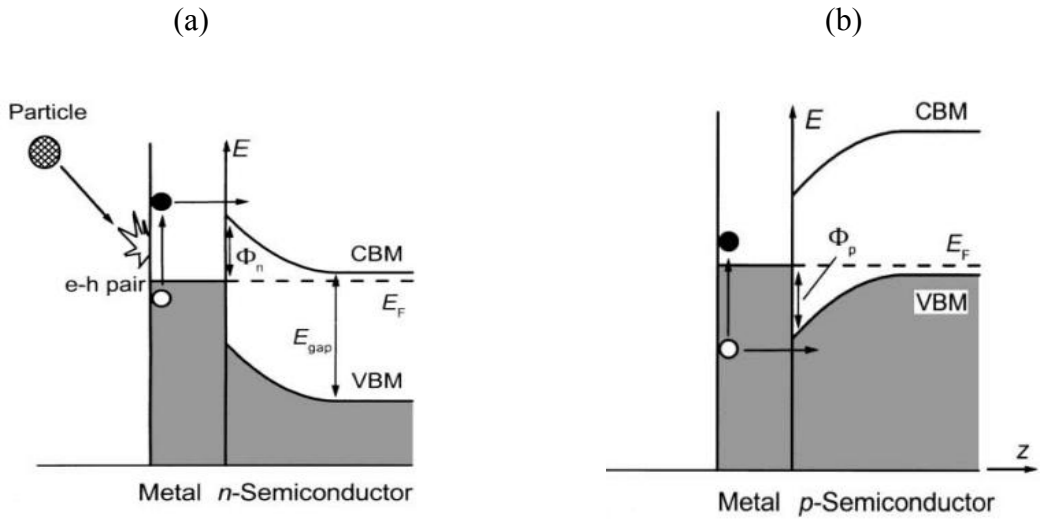

Figure 1.3. Principle of hot charge carriers in the (a) n-type Schottky diode, (b) p-type Schottky diode (Nienhaus, H et al., 2002)

1.2.1 Mean Free Path of Electrons in Metals

The theoretical mean free path of electrons (λ) in metals is defined as (Frese and Chen 1992):

$$\lambda = \frac{\sigma m_e v_F}{ne^2} \tag{1-11}$$

where e is the electron charge, n is the volume density, σ is the electrical conductivity, and $m_e v_F$ is the momentum at Fermi level. The mean free path of electrons at 295 K in some metals is presented in Table II. Exothermic reactions generate hot electrons with energies of 1–3 eV and very short period of lifetimes in the reorder of tens of femtosecond (Park et al. 2007). In this range of chemical energy, the mean free path of electrons in metals is typically 10 nm. Consequently, a catalytic metal with the thickness of ~ 5–15 nm can be used to collect the hot electrons as they traverse ballistically across the metal-semiconductor interface.

Table II. Mean free path of electrons at 295 k in some metals (Frese and Chen 1992)

Metal	λ (nm)
Ag	52.5
Al	14.5
K	30.0
Na	30.0
Au	38.0
Cu	39.0
Ni	10.5
Pd	10.5
Pt	7.8

1.2.2 Chemicurrent Detection with Metal-semiconductor Structures

When an exothermic chemical reaction such as oxidation of hydrogen to water occurs on the catalytic cathode (e.i palladium), the electrons that carry energies above the

Fermi level will overcome the potential barriers and move towards the n-type semiconductor anode (i.e. monocrystalline silicon carbide). The electrons will then be relaxed and returned to the cathode via the back Ohmic contact of an external circuit. The current generated through this process is called *chemicurrent*. Since an *in-situ* chemical process can only be initiated on the cathodes with high catalytic activities, this device is referred to as the *catalothermionic* power generator (Karpov and Nedrygailov 2009). Figure 1.4 shows the schematic of this device.

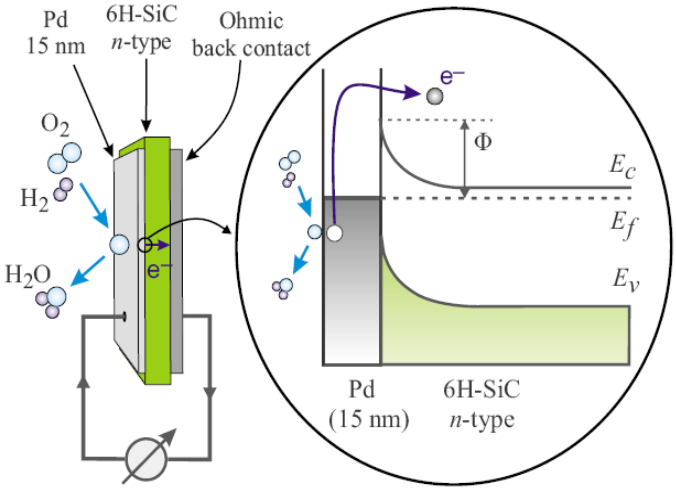

Figure 1.4. Schematic of a catalothermionic power generator. Φ, E_c, E_f, and E_v are the barrier height, conduction band bottom, Fermi level and valence band top, respectively (Karpov and Nedrygailov 2009)

The *in situ* exothermic chemical reaction in Schottky nanostructures could not only provide required temperature gradients but also enhance the excitation of hot electrons from the metal to semiconductor. The quantum efficiency of catalothermionic power generators is defined as the number of hot electrons received by an external load to the number of water molecules produced during the process of hydrogen oxidation. It has been shown that a quantum efficiency of 0.2 could be achieved for the catalytic oxidation

of hydrogen on Pd/n-SiC-6H nanostructures at temperature T= 660 K (Karpov and Nedrygailov 2009). This value is significantly larger than the quantum efficiency of 10^{-6} for emission of excited electrons into vacuum (Greber T 1997). The magnitude of chemicurrent strongly depends on gas molecules participating in surface reactions, the catalytic activity of metals, operating conditions such as temperature and total pressure, the metal film thickness, the potential barrier height of semiconductors and etc. It has been demonstrated that the chemicurrent value for Cu/n-Si(111) Schottky diode upon exposure to atomic hydrogen was about 2.5 pA (Nienhaus et al. 2002). The chemicurrent was increased about 10 times after annealing of the diode. The enhancement of current was contributed to an increased of the mean free path of hot electrons in the annealed sample. The same researchers investigated the effect of metal film thickness on chemicurrent measurements for Ag/n-Si(111) Schottky diode during atomic hydrogen exposure. Their results showed that chemicurrent values of 12 and 100 pA could be obtained for the Ag thickness of 22 and 7.5 nm, respectively. This implies that the detection of chemicurrent can be increased if the metal film thickness is in the order of the mean free path of hot electrons (~ 10 nm). The influence of metal surface temperature on chemicurrent measurements was studied during oxidation of carbon monoxide with a mixture of 100 Torr of O_2 and 40 Torr of CO on Pt/TiO_2 and Pt/GaN Schottky diodes (Park et al. 2007). In the case of Pt/TiO_2 the chemicurrent increased exponentially from 60 to 200 nA in the 473−553K range. However, the chemicurrent for Pt/GaN sample was found to be 120 nA at 553K. It was suggested that chemicurrent measurements could be influenced by the interface roughness of metal-semiconductor at high temperatures.

In this work, it will be demonstrated that the catalytic oxidation of hydrogen on a continuous 15 nm Pt film deposited on mesoporous TiO_2 structures results in a surprisingly high stationary chemicurrent in the range of 10−50 μA at room temperature. It will be shown that the chemicurrent highly depends on the properties of metal-semiconductor interface and concentration of hydrogen molecules.

1.3 Catalytic Combustion Processes

Catalytic combustion has become one of the primary routes for the production of energy and heat due to rising environmental and economic concerns (Groppi et al. 2009). Catalytic combustion of oxidizing fuels has been extensively investigated both experimentally and computationally in the past few years. From a practical viewpoint, catalytic combustion reactions are useful in numerous engineering applications such as large thermal power plants, micro-reactors for portable power generation, car exhaust emission control, catalytic afterburners and household burners (Trimm 1983; Schmidt 1990). The main difference between conventional (homogeneous) combustion and catalytic combustion is that the former can only operate within specific air to fuel ratios (flammability limits), while the latter is known as a flameless process. High-temperature stability and low-temperature activity of catalysis should be considered as the main criteria for developing and improving of combustion processes.

1.3.1 Catalytic Combustion of Methane

Complete combustion of methane, the main component of natural gas, has advantages over other hydrocarbons regarding environmental concerns such as low

emission of NO_x. Mass and heat transfer are the most important parameters in the kinetics of catalytic combustion of methane. The principle trend of methane conversion versus temperature can be described as the following (Lee and Trimm 1995): initiation of oxidation occurs as temperature is increased. This temperature depends on the concentration of methane and catalyst materials. By increasing the temperature, the rate of reaction increases exponentially and is instead controlled by the combustion-generated heat rather than the heat supplied. After this point, the reaction is controlled by mass transfer until all reactants will be completely consumed (light off temperature).

Many researchers have studied catalytic oxidation of methane on different metal oxides such as Co_3O_4, Al_2O_3, $ZnCrO_4$ and Cr_2O_3, noble and transition metals such as Pt, Pd, Rh, Fe, Co and Ni (Kul Ryu et al. 1999; Artizzu et al. 1999; Choudhary et al. 2002; Enger et al. 2008). Superior activity of noble metals compared to transition metal oxides make them better candidates for low-temperature combustion. These noble metals can be used either with or without a substrate. Supported catalysts improve the catalytic activity by increasing dispersion of noble metals in addition to preventing the aggregation of active metals at elevated temperature during combustion processes.

Platinum and palladium are the most common noble metals which have been used for the oxidation reaction, due to high volatility of other noble metals (Baldwin and Burch 1990; Pavlov and Qiao 2012). It was observed that the ratio of O_2:CH_4 had a significant impact on the oxidation of methane over Pt and Pd deposited on alumina substrate (Trimm and Lam 1980; Mouaddib et al. 1992). Carbon dioxide and carbon monoxide are formed under oxygen-rich and oxygen deficient atmospheres, respectively. Also, it was reported that presence of CO in the feed had no effect on the methane

conversion under both rich and lean oxygen conditions (Oh et al. 1992). Increases in size of Pt or Pd particles and the concentration of particles increase the overall rate of methane oxidation; this proves the reaction is sensitive to surface morphology.

The behavior of Pt-based catalysts during the oxidation and reduction of Pt has been shown to be strongly affected by the support material. For example, it has been reported that Al_2O_3 enhanced the reoxidation of Pt compared to ZrO_2 (Ciuparu and Pfefferle 2001). At low temperatures, Pt/Al_2O_3 shows the highest activity which is likely due to the greater surface area to volume ratio than exhibited by other support materials. At temperatures sufficiently high, however, the surface area of Al_2O_3 decreases due to sintering and other energy minimization mechanisms; at this point other catalysts gain more attention. It has been shown that Pt/ZrO_2 is a very active catalyst for temperatures between 620 and 800 ˚C, while for temperatures above 800 ˚C $Pt/LaMnAl_{11}O_{19}$ is a better candidate for combustion of methane (Persson et al. 2006). It is well known that palladium-supported catalysts show higher activity for methane combustion under lean conditions compared to platinum-based catalysts. There is a general consensus that several factors such as Pd loading, metal precursor and pretreatment conditions have great effect on activity of palladium-supported catalysts (Burch et al. 1996). An excess of oxygen during the oxidation of palladium reduces the particle size of Pd, further oxidation of these small crystallites leads to production of palladium oxide (PdO). It has been shown that PdO is the active form of palladium in methane combustion on Pd supported catalysts (Yang et al. 2000; Eguchi and Arai 2001). The catalytic behavior of palladium is affected by the type of the support regarding Pd dispersion and Pd-support interaction. For this purpose, various types of metal oxides such as SiO_2, NiO and CeO_2-

ZrO_2 have been extensively studied (Bozo et al. 2000; Yang et al. 2002). Due to high specific area and low manufacturing costs, Al_2O_3 is the most commonly metal oxide used in the methane combustion at low and moderate temperatures (Yang et al. 2000; Kucharczyk et al. 2004). However, at high temperatures alumina is not very stable and foreign ions such as lanthanum (LA) and barium (Ba) were added to improve the thermal stability of alumina which increased the catalytic activity of Pd/Al_2O_3 (Thevenin 2003). It was found that the methane conversion on Pd/Al_2O_3 was significantly affected by operation temperature depending on PdO activity (Persson et al. 2006). PdO forms between 300 and 400 ˚C and is the most active phase of palladium for methane conversion up to 770 ˚C, but beyond this temperature PdO transforms to less active catalytic form of Pd leading to decrease of conversion.

1.3.2 Catalytic Combustion of Hydrogen

Hydrogen, the most abundant element in the world, is known as one of the lightest and cleanest energy carriers that has been the subject of remarkable interest in many applications such as fuel cell and micro-combustion technologies (Dunn 2002). Significant use of hydrogen fuel over other conventional fossil fuels contributes to the reduction of greenhouse gas emissions such as CO, NO_x, SO_x, non-methane hydrocarbons (NMHC) and particulates in which outstandingly improves air quality, human health problems and climate changes (Jacobson et al. 2005). Water vapor is the only product of catalytic combustion of hydrogen when it is carried out in the mixture with pure oxygen. In addition to cleanliness and sustainability, other considerable characteristics of hydrogen combustion, such as wide range of flammability, high

diffusivity, low ignition energy, and high energy density have been utilized in both small and large catalytic combustors (Elam et al. 2003).

Due to complicated interactions between homogeneous (gas-phase) and heterogeneous (gas/catalyst interface) reactions, the two main processes during a combustion, kinetic mechanisms of many systems are not very well understood. An exception is the oxidation of hydrogen. A great many investigations have been devoted to address the role of homogeneous and heterogeneous chemistries in the bifurcation behavior of hydrogen combustion mechanism (Ikeda et al. 1995; Rinnemo et al. 1997; Brady et al. 2010; Fernandes et al. 1999). When the surface temperature is very low, neither gas-phase nor surface reactions occur. At very high surface temperature all of the hydrogen molecules are depleted due to severe homogenous reactions and no heterogeneous reaction is possible at the surface. Depending on the surface temperature of catalyst, ignition and extinction temperatures, surface activity of catalyst, concentration of H_2/O_2 mixture and flow-rate of reactant stream, several regimes are distinguished in oxidation of hydrogen as following:

(1) Only the surface reaction takes place.

(2) Only homogeneous reactions occur.

(3) The surface reaction is prevented by gas-phase reactions.

(4) Homogeneous reactions are prevented by the surface reaction.

There is a general agreement that heterogeneous chemistry controls the overall reaction at low temperatures, whereas homogeneous chemistry dominates at high temperatures. In particular for fuel-lean mixture, heterogeneous reaction can take place at the ignition temperature of 400 K and the room temperature extinction, whereas the

ignition and extinction temperature of homogeneous reactions occur at temperature around 1000 K (Park et al. 1998). The primary investigations on hydrogen oxidation chemistry revealed that 20 reactions and 9 species are involved in the homogenous process (Miller and Bowman 1989). Table III shows these 20 reversible reactions where M represents third-body species.

Table III. Kinetic mechanisms for homogeneous hydrogen oxidation (Miller and Bowman 1989)

Reaction No.	Reaction
1	$H_2 + O_2 \leftrightarrow 2OH$
2	$OH + H_2 \leftrightarrow H_2O + H$
3	$OH + O \leftrightarrow O_2 + H$
4	$OH + H_2 \leftrightarrow OH + H$
5	$H + O_2 + M \leftrightarrow HO_2 + M$
6	$HO_2 + OH \leftrightarrow H_2O + O_2$
7	$HO_2 + H \leftrightarrow 2OH$
8	$HO_2 + O \leftrightarrow OH + O_2$
9	$2OH \leftrightarrow H_2O + O$
10	$2H + M \leftrightarrow H_2 + M$
11	$2H + M \leftrightarrow H_2 + M$
12	$2H + M \leftrightarrow H_2 + M$
13	$H + OH + M \leftrightarrow H_2O + M$
14	$H + O + M \leftrightarrow OH + M$
15	$2O + M \leftrightarrow O_2 + M$
16	$HO_2 + H \leftrightarrow H_2 + O_2$
17	$2HO_2 \leftrightarrow H_2O_2 + O_2$
18	$H_2O_2 + M \leftrightarrow 2OH + M$
19	$H_2O_2 + H \leftrightarrow HO_2 + H_2$
20	$H_2O_2 + OH \leftrightarrow H_2O + HO_2$

Mass spectrometry and laser-induced florescence (LIF) techniques have been used to study the kinetics of individual steps of homogeneous and heterogeneous reactions over Pt surface (Williams et al. 1992). LIF technique provides more quantitative information about the chemistry and the kinetic of all species such as OH which is produced at slower rate compared to other radical species in the reaction. Also, LIF can be used at high surface temperature and any hydrogen-oxygen pressure; whereas other techniques can be applied only in ultra-high vacuum condition and low surface temperature. Table IV summarizes the heterogeneous reactions mechanism of hydrogen oxidation over platinum surface where (s) denotes surface adsorbed species.

Table IV. Kinetic mechanisms for heterogeneous hydrogen oxidation over platinum surface (Williams et al., 1992)

Reaction No.	Reaction
1	$H(s) + O(s) \leftrightarrow OH(s) + Pt$
2	$OH(s) + Pt \leftrightarrow H(s) + O(s)$
3	$H(s) + OH(s) \leftrightarrow H_2O(s) + Pt$
4	$H_2O(s) + Pt \leftrightarrow H(s) + OH(s)$
5	$2OH(s) \leftrightarrow H_2O(s) + O(s)$
6	$H_2O(s) + O(s) \leftrightarrow 2OH(s)$
7	$H_2 + 2Pt \leftrightarrow 2H(s)$
8	$2H(s) \leftrightarrow H_2 + 2Pt$
9	$O_2 + 2Pt \leftrightarrow 2O(s)$
10	$2O(s) \leftrightarrow O_2 + 2Pt$
11	$H_2O + Pt \leftrightarrow H_2O(s)$
12	$H_2O(s) \leftrightarrow H_2O + Pt$
13	$OH(s) \leftrightarrow OH + Pt$

It can be seen that the chemistry of heterogeneous hydrogen oxidation follows the Langmuir-Hinshelwood mechanism. When hydrogen and oxygen molecules adsorb on the platinum surface, they dissociate to adsorbed species of H(s) and O(s), respectively. H(s) and O(s) are combined to produce an unstable OH(s). Then, this active radical species is transformed to H_2O(s). Finally, desorption of H_2O(s) occurs at low temperature and H_2O is formed in the gas phase.

The role of surface temperature in the coverage of adsorbed species has been addressed (Vlachos and Bui 1996). Since hydrogen gas has both low molecular weight and high sticking coefficient, the adsorption rate of H_2 molecules is significantly higher compared to O_2 molecules at low temperatures. Below the ignition temperature, the H(s) is the dominant species sticking on the surface. As the surface temperature is increased, the system tends to ignite adsorbed hydrogen. Consequently, excessive O_2 molecules above the surface adsorb with a higher rate than that of H_2 molecules and they dissociate to O(s). After ignition up to high temperatures, a phase transition occurs and the surface is covered with O(s). Also, it has been shown that the coverages of surface species depend on the ratio of H_2/O_2 (Fernandes et al. 1999). In a fuel-rich mixture ($H_2/O_2 > 1$), excessive H(s) immediately reacts with OH(s), resulting in very low coverage of OH(s). The pathway for H_2O production is as the following steps:

$$H(s) + O(s) \leftrightarrow OH(s) + Pt \quad (1\text{-}12)$$

$$H(s) + OH(s) \leftrightarrow H_2O(s) + Pt \quad (1\text{-}13)$$

$$H_2O(s) \leftrightarrow H_2O + Pt \quad (1\text{-}14)$$

In a fuel-lean mixture ($H_2/O_2 < 1$), since excessive O(s) is the dominant species on the surface, OH(s) will be recombined with itself. High coverage of OH(s) leads to a different pathway which is slower than the surface reaction mechanism of a fuel-lean mixture. This surface reaction pathway can be expressed as the following:

$$2OH(s) \leftrightarrow H_2O(s) + Pt \quad (1\text{-}15)$$

$$H_2O(s) + O(s) \leftrightarrow H_2O + Pt \quad (1\text{-}16)$$

It has been shown that platinum provides a source of OH(s) in a fuel-lean mixture at high temperatures that assists homogenous combustion on the surface (Park et al. 1998). In contrast, this behavior has not been observed in a fuel-rich mixture.

In this work, the focus of our experiments was mainly on the heterogeneous reaction of a fuel-lean of hydrogen and oxygen mixture over a catalytic surface at low temperature. This approach helped us to avoid any possible gas-phase combustion in the system at elevated temperatures.

1.4 Properties of Titanium Dioxide Materials

Titanium dioxide (TiO_2), also known as titania, has been used extensively in many technological applications such as heterogeneous catalysis, photocatalysis, gas sensors, solar cells, white pigments, self-cleaning coatings, lithium-based batteries and memristors (Li et al. 2000; Diebold 2003; Lin et al. 2003). TiO_2 is found in three different mineral structures in nature: anatase, rutile and brookite. Anatase type TiO_2 has a tetragonal structure and its application is mainly in solar cells and photocatalysis because of its high electron mobility and low density (Carp et al. 2004). Rutile type TiO_2

also belongs to the tetragonal structure. It has been reported that this type of titania has very poor photocatalytic activities but it is mainly used in white pigments (Sclafani et al. 1990). Brookite TiO_2 has an orthorhombic crystal structure. Due to its complicated structure, it has been reported that brookite structure is not a preferred form of TiO_2 for experimental investigations (Thompson and Yates 2006).

Various methods are applied to synthesize titanium dioxide in the configuration of thin films, powder and crystals (Carp et al. 2004). Thin films can be prepared using precipitation methods (Poznyak et al. 1998; Pedraza and Vazquez 1999), solvothermal methods (Aruna et al. 2000), electrochemical synthesis (Matsumoto et al. 2000), chemical vapor deposition (CVD) and physical vapor deposition (PVD) (Jones and Chalker 2003). Microemulsion method is used for fabrication of nanoparticles (Chhabra et al. 1995). Sol-gel methods (Iwasaki et al. 1998), and spray pyrolysis deposition (Ahonen et al. 1999) are applied for the synthesis of both thin films and powders. Complicated techniques such as molecular beam epitaxy, ion implantation and dynamic ion beam mixing are used rarely compared to other methods mentioned above (Ong and Wang 2001; Herman and Gao 2001; Murakami et al. 2001).

1.4.1 Photocatalytic Properties of TiO_2

Titanium dioxide has been known as an ideal photocatalytic material in wastewater treatment technology, purification of air and water-splitting for hydrogen production because of its remarkable features, such as high chemical stability, large negative conduction band, non-toxicity and low cost. Anatase structure has a higher photocatalytic activity than that of rutile and brookite structure, due to higher Fermi level and larger hydroxyl groups on the surface (Tanaka et al. 1991). Although some

researchers have reported that a mixture of anatase (70−75%) and rutile (30−25%) shows higher activity than pure anatase (Muggli and Ding 2001; Ohno et al. 2001). Beside the crystal structure, several factors, such as noble metals doping on the surface, mean pore size, specific surface area, synthesis procedures and porosity can enhance the photocatalytic activity of TiO_2 (Harada and Ueda 1984). Among all different types of commercial TiO_2 photocatalysts, Degussa P25 is commonly used in photocatalytic reactions.

TiO_2 as an n-type semiconductor has a wide energy band gap of 3.2 and 3.02 eV for the anatase and rutile structures, respectively (Wold 1993). A photon with energy equal or greater than the band gap is required to excite the electrons in the valance band into the conduction band of TiO_2 structure. For electron excitation to the conduction band, TiO_2 is only able to absorb photons with wavelengths equal to or less than 384 nm. This implies visible light is not a suitable light source for photocatalytic activity of TiO_2; hence numerous experiments have been carried out under UV radiation for excitation processes (Legrini et al. 1993; Hoffmann et al. 1995; Alfano et al. 2000). When TiO_2 surface is illuminated by UV radiation, electron-hole pairs are generated due to the promotion of excited electrons to the conduction band and formation of positive holes in the valance band. These electron-hole pairs can recombine on the TiO_2 surface. The recombination of electrons and holes leads to the generation of heat or photons that decreases the photocatalytic activity of TiO_2. However, the electrons and holes that are not recombined in the bulk can migrate to the surface and participate in oxidation-reduction processes. Therefore, the competition between electron-hole recombination and electron-hole trapping indicates that the latter improves the photocatalytic activity of

TiO_2 (Wold 1993). It has been shown that the formation of electron-hole pairs is very useful in either hydrogen production from water splitting or photocatalytic degradation of organic or inorganic pollutants (Wold 1993; Ni et al. 2007; Thiruvenkatachari et al. 2008).

The potential of a semiconductor band structure plays a crucial role in photocatalytic water splitting process. For efficient photocatalytic hydrogen production, the valence band of a photocatalys should be more positive than the oxidation potential of water and its conduction band level should be more negative than the potential of hydrogen evolution. It has been reported that semiconductors such as TiO_2, ZrO_2, $CaTiO_3$, $KTaO_3$ and Ta_2O_5 can satisfy this thermodynamic condition (Hashimoto et al. 2005). However, TiO_2 is much more effective compared to other semiconductors because of its more photocatalytic activity. The mechanism of water splitting for hydrogen production using TiO_2 photocatalyst is very similar to electrolysis. Water molecules react with generated positive holes to produce O_2 and H^+. Consequently, H^+ ions are reduced by the exited electrons to form hydrogen molecules. The principle mechanism described above can be shown as the following steps (Hashimoto et al. 2005):

$$TiO_2 + h\nu \rightarrow e^- + h^+ \quad (1\text{-}17)$$

$$2H_2O + 4h^+ \rightarrow O_2 + 4H^+ \quad (1\text{-}18)$$

$$2H^+ + 2e^- \rightarrow H_2 \quad (1\text{-}19)$$

The overall reaction is

$$2H_2O + 4h\nu \rightarrow O_2 + 2H_2 \quad (1\text{-}20)$$

Photocatalytic water splitting by TiO_2 has been used in energy conversion devices. Compared with the conventional fuel cells, the energy conversion efficiency of these devices is still low. The main reasons for low efficiency of solar photocatalytic devices can be listed as (Ni et al. 2007):

- Short lifetime and fast recombination of conduction band electrons with valance band holes
- Quick backward reaction of hydrogen and oxygen
- Limited utilization of solar radiation energy

In order to enhance the solar photocatalytic activity of TiO_2, several techniques have been developed (Litter 1999; Takeuchi et al. 2000; Subramanian et al. 2001). These techniques are categorized into two broad groups: modification techniques and chemical additives (Ni et al. 2007). The photocatalytic modification techniques include noble metal loading (Liu et al. 2004), transitional metal ion and anion doping (Wilke and Breuer 1999; Chen et al. 2004), dye sensitization (Jana 2000) and metal-ion implantation (Yamashita et al. 2002). Loading of noble metals, such as Pt, Au, Ni, and Cu on TiO_2 surface can increase its photocatalytic activity by preventing of electron-hole pairs recombination; whereas other techniques mentioned above are applied to promote its activity by broadening of TiO_2 response to the visible light range. Addition of chemical additives, such as electron donors (particularly organic compounds) and carbonate salts are used to inhibit fast backward reaction of hydrogen and oxygen and electron-hole pairs recombination, respectively.

It has been shown that TiO_2 photocatalysis can be used in the degradation of organic pollutants in an aqueous solution (Matthews 1988; Tanguay et al. 1989). The principle mechanism of this process is very similar to the photocatalytic water splitting reaction. Electron-hole pairs are generated when TiO_2 surface is illuminated by UV radiations. When electrons and holes on the surface are separated, adsorbed oxygen molecules react with the excited electrons, whereas positive holes react with either organic pollutants or water molecules. If positive holes participate in oxidation of water molecules, OH° radicals will be produced. Furthermore, OH° radicals decompose the pollutants. CO_2 is produced when positive holes oxidize the organic pollutants. The mechanism scheme can be expressed as (Thiruvenkatachari et al. 2008):

$$TiO_2 + h\nu \rightarrow e^- + h^+ \quad (1\text{-}21)$$

$$e^- + O_2 \rightarrow O_2^- \quad (1\text{-}22)$$

$$h^+ + H_2O \rightarrow OH^{\circ} + H^+ \quad (1\text{-}23)$$

$$h^+ + \text{Organic pollutants} \rightarrow CO_2 \quad (1\text{-}24)$$

$$OH^{\circ} + \text{Organic pollutants} \rightarrow CO_2 \quad (1\text{-}25)$$

Deposition of gold metals on TiO_2 surface has been reported to enhance the photocatalytic activity up to 30% compared with films without gold particles (Albert et al. 1992). It has been demonstrated that a superior efficiency in photocatalytic degradation of organic compounds can be achieved if the rate of oxygen reduction is fast (Gerischer and Heller 1991).

1.4.2 Memristive Behavior in TiO_2

Beside the existing three classical circuit elements (the resistor, capacitor and inductor), in 1971 the memristor as the fourth fundamental circuit element was introduced; based on the theory of symmetry (Chua 1971). From the theoretical point of view, resistors, capacitors and inductors are defined by the well-known relationship of the current (I) – voltage (V) curve, charge (q) – voltage curve and flux linkage (φ) – charge curve, respectively. A memristor (a contraction of memory–resistor) is characterized by the flux linkage-charge curve and works as a nonlinear two-terminal electrical device. The electrical resistance of a memristor is not constant and depends on the amount of charge that had previously flowed through it, polarity of the voltage and the time integrals between the voltage and current (Miller et al. 2010). In contrast to a resistor, capacitor and inductor, under sinusoidal excitations a memristor exhibits a unique bipolar switching behavior in the I−V plane that is called "pinched-hysteresis loops". Due to this I−V characteristic, the resistance of the doped and undoped layers is switched between the low resistance (R_{ON}) and high resistance (R_{OFF}).

A memristor is defined by (H. Kim et al. 2012):

$$v(t) = R(t)i(t) = \frac{d\varphi}{dt} \cdot \frac{dt}{dq} i(t) \tag{1-26}$$

The relation between the voltage and the current can be expressed as:

$$v(t) = \left(R_{\mathrm{ON}} \frac{w(t)}{D} + R_{\mathrm{OFF}} \left(1 - \frac{w(t)}{D} \right) \right) i(t) \tag{1-27}$$

where D and w represent the thickness of undoped (TiO_2) and doped layers (TiO_{2-x}), respectively. Also, the resistance of a memristor (known as memristance M) is defined as:

$$M = \frac{d\varphi}{dq} = R_{OFF}\left\{\left[1 + \frac{w}{D}\left(\frac{R_{ON}}{R_{OFF}} - 1\right)\right] - \frac{\mu_v R_{ON}}{D^2}\left(1 - \frac{R_{ON}}{R_{OFF}}\right)q(t)\right\} \qquad (1\text{-}28)$$

where μ_v =10^{-14} $m^2s^{-1}V^{-1}$ is the ion mobility coefficient (Hu et al. 2011).

The theoretical concept of a memristor device was successfully developed for many years. However, the memristor did not receive much attention until the existence of a physical solid-state memristor was claimed by the Stanley Williams group at Hewlett-Packard (HP) Labs in 2008 (Strukov et al. 2008). It was announced that TiO_2 in the nanoscale crossbar architecture performed as a promising memristor, showing remarkable switching characteristics and an extremely high memory capacity. Since then, memristors have been widely used in numerous applications, such as nonvolatile memory; also known as resistance random access memory (RRAM), programmable logic, signal processing, neural networks and pattern recognition circuits (Yang et al. 2008; Jo et al. 2009; Robinett et al. 2010). Recently, it has been shown that various types of materials can be used for fabrication of memristors including metal oxides (TiO_2, SiO_2, CoO, Fe_2O_3 and VO_2) (Yang et al. 2008), perovskite-type oxides (Nian et al. 2007), amorphous silicon (Jo and Lu 2008), sulfides (Ag_2S) (Waser and Aono 2007) and metal/organic monolayer/oxide (Stewart et al. 2004). However, TiO_2 has been the most common material used in memristor applications due to its inexpensive and simple fabrication and its unique properties as well.

The memristive behavior is determined by the electroforming processes that occur during the TiO_2 preparation. Since the electrical resistance of TiO_2 is high (in the order of GΩ), it initially behaves as an insulator. In order to activate its bipolar resistive switching, the electrical resistance should be degraded by applying a voltage, known as an electroforming voltage. It has been shown that during the electroforming process several parameters including the magnitude and time interval of applied voltages, the compliance voltages and the ambient atmosphere have significant impacts on the memristive behavior of TiO_2 (Jeong et al. 2008). The electroforming voltage divides TiO_2 into two different layers; one layer with a perfect ratio of oxygen to titanium (2:1) and one layer with oxygen vacancies (TiO_{2-x}). The former works as an insulator and is known as the undoped region while the latter is termed as the doped region. Low mobility and diffusivity of oxygen deficiencies make TiO_{2-x} to show better ionic conductivity compared to TiO_2. When a positive voltage is applied, oxygen vacancies migrate from the metallic TiO_{2-x} region to the TiO_2 insulator layer. This increases the conductivity of TiO_{2-x} and thus the entire memristor. When a negative voltage is applied, the positive oxygen deficiencies are drawn out of TiO_2 layer; causing the whole system works as a resistor. Once either a positive or negative voltage is turned off, the boundary between the TiO_2 and TiO_{2-x} layers is frozen and oxygen vacancies do not move anymore and stay in their current state. That is the main reason why a memristor can recall the last applied voltage (Yang et al. 2008).

CHAPTER 2

EXPERIMENTAL PROCEDURE

This chapter describes the experimental equipments used during catalytic oxidation of hydrogen to water for chemicurrent measurements. The methods performed for the fabrication of metal-semiconductor nanostructures will be discussed. Also, the characterization techniques are mentioned in the following sections.

2.1 Experimental Setup

The experimental setup used for chemicurrent studies is shown in Figure 2.1. This system consists of a mass-spectrometer, ultra high vacuum chamber, multichannel temperature controller, Keithley 2400 source meter, vacuum pumping system, and absolute pressure transducers. The following sections describe briefly each of these components.

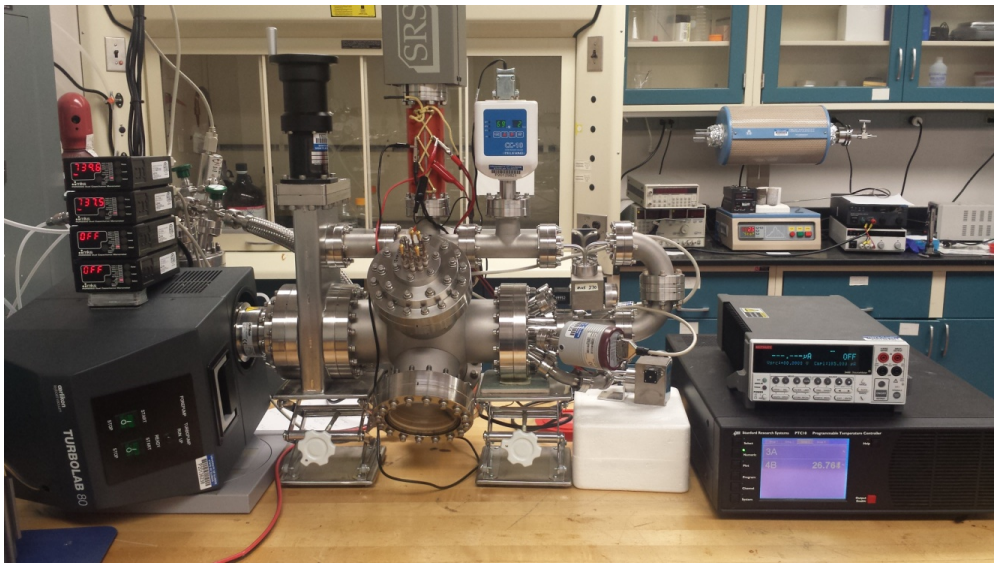

Figure 2.1. The experimental setup for chemicurrent measurements

2.1.1 Mass-Spectrometer

The mass-spectrometer is an instrument that analyzes the molecular weight and type of individual gas molecules by measuring the ratio of mass-to charge (m/z) of gas-phase ions. There are many different types of mass-spectrometers, but all follow the same principle operation. The charged particles (positive ions) are formed by bombardment of gas molecules with high energy electrons. Then, these ions are filtered and quantified by their m/z ratios. In our experiments, SRS RGA Model 200 is used as the mass-spectrometer that is shown in Figure 2.2.

(a)

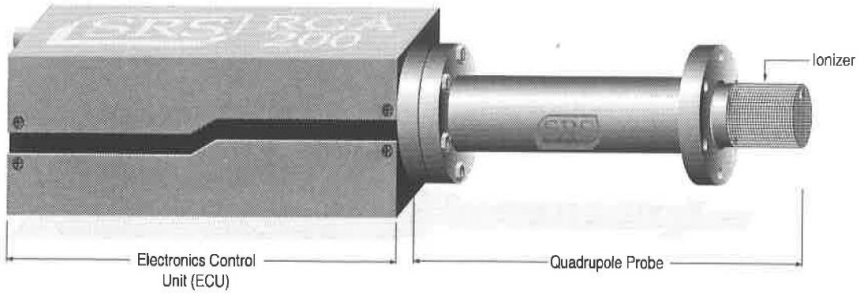

(b)

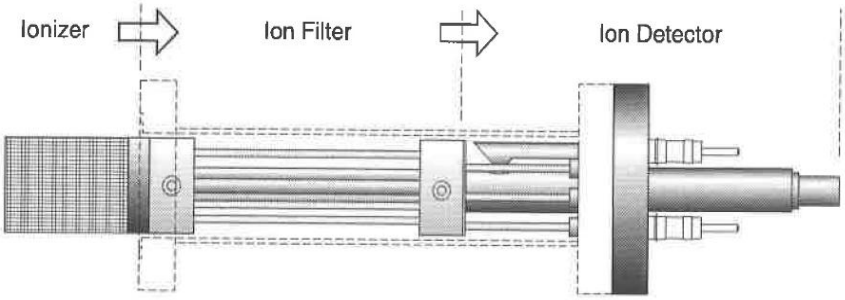

Figure 2.2. Schematic of (a) SRS RGA Model 200 (b) probe components (Stanford Research System, Inc. 1996)

The SRS RGA consists of an Electronics Control Unit (ECU) and a quadrupole probe which assembles directly on the ultra high vacuum chamber. The ECU regulates the

function of the RGA and transfers its data for further analysis to the computer. The quadrupole probe includes three fundamental components:

- The ionizer which converts the gas molecules to positive ions via a heated filament.
- The ion filter which separates the positive ions based on their m/z ratios.
- The ion detector that measures the separated ions according to their abundance.

In this work, SRS RGA is used to monitor the ignition and extinction of hydrogen oxidation to water on the catalytic nanofilm surfaces. Also, SRS RGA provides the partial pressure of gases presented in the oxidation processes such as hydrogen, oxygen and water molecules.

2.1.2 Multichannel Temperature Controller

The Programmable Temperature Controller (PTC 10) is used to monitor and control the surface temperatures inside the ultra high vacuum chamber during the oxidation of hydrogen to water. The resolution of PTC 10 is in the milliKelvin range. The different sensor types and their temperature ranges are listed in Table V.

Table V. Compatible sensors for PTC 10 (Stanford Research System, Inc. 2010)

Sensor Type	Temperature range (K)
Diode	1.0−500
cheRuthenium oxide	0.05−300
Resistance Temperature Detector (RTD)	48.15−1173.15
Thermistor	193.15−523.15

Resistance Temperature Detectors (RTDs) are used due to their wide temperature range and accurate measurements as well. In particular, RTD Omega F2020-100 with a dimension of 2×2×0.8 mm^3 is used in our experiments. In this sensor, the resistance of platinum wires is used to measure the surface temperature. The resistance of RTD is recorded in a Pico high resolution data logger and converted to the temperature in Celsius using the following equation:

$$T = \frac{1}{2} \cdot \left\{ \left(\frac{-A}{B} \right) - \sqrt{\left(\frac{A}{B} \right)^2 - \frac{4}{B} \cdot \left(1 - \frac{R}{R_0} \right)} \right\} \quad (2\text{-}1)$$

where: $A = 3.90833 \times 10^{-3}\ ^\circ C^{-1}$

$B = -5.7753 \times 10^{-7}\ ^\circ C^{-2}$

R = Resistance of RTD recorded in the data logger

R_0 = Resistance of RTD at 0 ˚C which is 100 Ω

T = Surface temperature in ˚C

2.1.3 Source Meter

The current-voltage characteristic (I−V curve) of our samples is measured using a Keithley 2400 source (Figure 2.3) meter under varying operation conditions. This instrument works either as a voltage/current/ohm meter or voltage/ current source with the following source and measurement ranges:

- Source current in the range of 50 pA to 1.05 A.
- Measure current in the range of 10 pA to 1.055 A.
- Source voltage in the range of 5 μV to 210 V.

- Measure voltage in the range of 1 μV to 211 V.
- Measure resistance in the range of 100 μΩ to 211 MΩ.
- Maximum source power of 22 W.

Figure 2.3. Keithley 2400 Source Meter

Keithley 2400 source meter can be used in a broad range of devices, including resistors, diodes, photodetectors, photovoltaic cells, thermistors, connectors, switches and etc. In the present study, this device is primarily used for the electrical characterization of Schottky diodes created between the metal (i.e. platinum) and the semiconductor (i.e. titanium dioxide). Also, the change of Pt/TiO_2 resistance with time during the exposure to hydrogen and oxygen gases is recorded with the Keithley 2400 source meter in its voltage source mode (Chapter 5).

2.1.4 Absolute Pressure Transducer

In order to measure the absolute pressure of gases inside the analytical chamber, three different types of pressure transducers are used: MKS Types 722A, 722B, and 626. A pressure transducer consists of two components: a variable capacitance sensor and signal conditioner. The sensor is composed of a pipe attached to a cell in the transducer. One side of this cell is made of an elastic diaphragm positioned opposite the pipe. The gas pressure is measured when it is exposed to the front side of the diaphragm. The back side of the diaphragm is connected to a ceramic disc containing two electrodes. The back side is persistently evacuated (10^{-7} Torr) and a chemical getter system maintains its vacuum. Changing pressure causes a deflection in the diaphragm. This deflection results a variation in the capacitance of the sensor electrode. An oscillator converts this capacitance variation to a DC voltage. In order to produce an output signal scaled to the transducer range, an electronic signal conditioner is required to linearize and amplify resultant signals. Finally, a gauge controller (MKS Type PDR 2000) is used for the pressure readout.

2.1.5 High Vacuum Pumping System

The chemicurrent studies, electrical characterization of samples and mass-spectrometry measurements are carried out under ultra high vacuum (UHV) conditions using a Turbomolecular Pump System (TURBOLAB 80). It consists of two components: a diaphragm vacuum pump (DIVAC 0.8 T) and a turbomolecular pump (TURBOVAC

SL 80 H). The diaphragm vacuum pump works as the backing system and turbomolecular pump is used for reaching UHV levels. TURBOLAB 80 has the following specifications:

- Pumping speed of the diaphragm pump: 0.7 m^3/h
- Ultimate pressure of the diaphragm pump: 3 mbar
- Run-up time of the turbomolecular pump: 1.5 min
- Attainable ultimate pressure: 10^{-7} mbar
- Pumping speed for N_2: 65 I/s

2.1.6 Ultra High Vacuum Chamber

The central component of our laboratory system is an ultra high vacuum chamber where the catalytic oxidation of hydrogen to water takes place. This spherical chamber has a volume of 4.5 L and is made of 304L stainless steel. The chamber is connected to the turbomolecular pump via a ConFlat (CF) flanged standard gate valve. For chemicurrent measurements, hydrogen and oxygen gases are admitted to the chamber through two different Nupro BK gas shut-off valves.

The sample is placed on a sample holder using a copper clamp and mounted inside the chamber via a 2.75″ CF electrical feedthrough flange (Figure 2.4). The feedthrough flange contains 12 copper pins (2.4 mm diameter) and transfers the chemicurrent, pressure and temperature data to the Pico data logger across the vacuum wall.

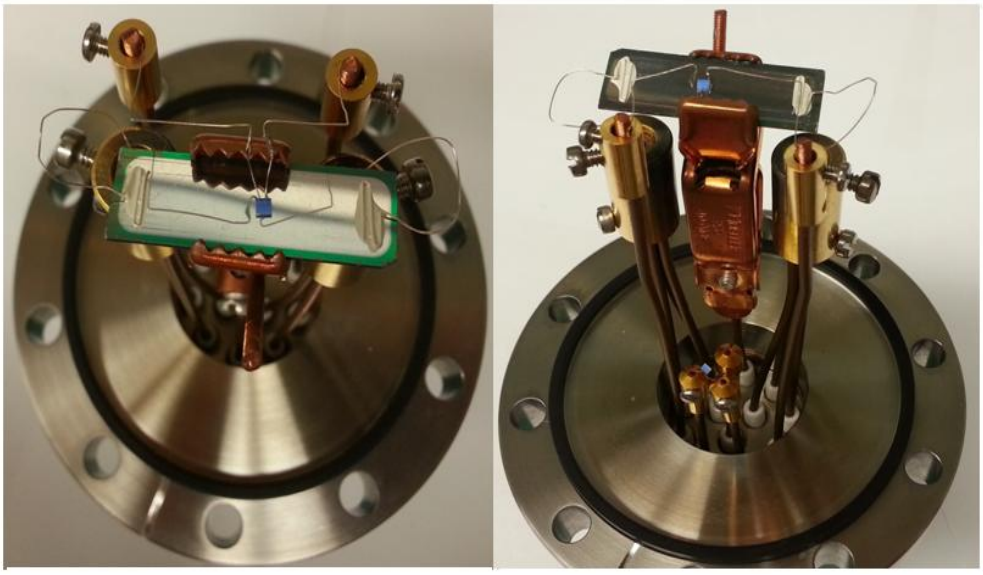

Figure 2.4. Sample holder

2.2 Sample Fabrication Procedure

This section describes the synthesis techniques utilized for fabrication of our samples used in chemicurrent measurements. In the first step, a mesoporous semiconductor layer is prepared by plasma electrolytic oxidation method (section 2.21). Next, the Schottky barrier is made by deposition of a catalytic metal (Pt) on top of the semiconductor layer using the electron beam physical vapor deposition (section 2.2.2).

2.2.1 Plasma Electrolytic Oxidation Process

Plasma electrolytic oxidation (PEO), also known as spark anodizing, anodic spark oxidation, or micro-arc oxidation (MAO) is an electrochemical process for conversion of a metal surface to an oxide ceramic layer. This method is commonly applied to produce an oxide layer on metals such as aluminum, titanium, magnesium, tungsten and

zirconium in order to improve their mechanical, thermal, dielectric and corrosion properties (Yerokhin et al. 1999; Ma et al. 2006; Duan et al. 2007). Compared to conventional anodic oxidation, PEO employs a higher voltage and current. For example, it has been reported that at least 200 V is required for the plasma electrolytic oxidation of aluminum (Snizhko et al. 2004). In the PEO process, the metal (anode) is immersed in an aqueous electrolyte of an electrochemical cell and a high voltage/current is applied between the electrodes. Due to this high-applied voltage/current, the plasma/discharge phenomenon occurs on the metal surface resulting in a thick oxide layer (tens of hundreds of micrometers).

In this study, PEO method is used to produce mesoporous TiO_2 and films on Ti substrates. A titanium strip is inserted as an anode into an electrochemical cell containing an aqueous electrolyte (H_2SO_4) and a graphite electrode as a cathode. A power supply (Sorensen XHR 300-3.5 DC) at a constant current mode is applied to pass a high current through the metal until a specific voltage is reached. In order to maintain temperature low, the electrochemical cell is placed in a 4.5 L container filled with water. Figure 2.5 shows the schematic of this set up for anodization of titanium in H_2SO_4.

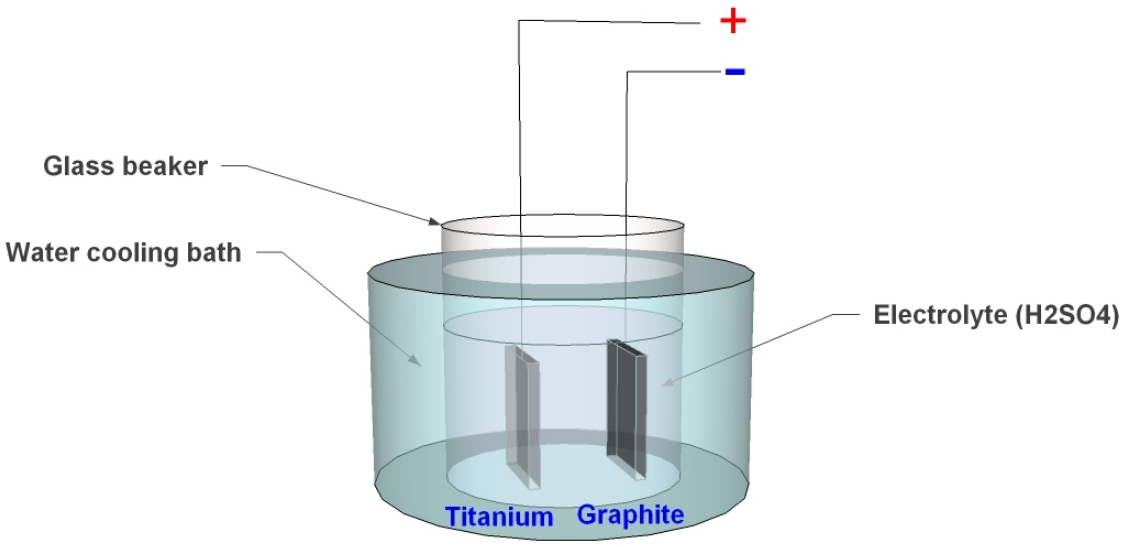

Figure 2.5. Schematic of the titanium anodization cell

Several parameters effect on the PEO process: anodizing voltage, anodizing current, time duration, electrolyte temperature, electrolyte type and concentration. By varying each of these parameters, samples with different thicknesses and properties would be obtained that will be discussed in the following chapters.

2.2.2 Electron Beam Physical Vapor Deposition

Physical vapor deposition (PVD) is a vacuum deposition method in which thin films (in the range of few nanometers to several micrometers) are deposited onto various surfaces such as semiconductor substrates. There are different types of PVD including: pulsed laser deposition, sputter deposition, evaporative deposition, cathodic arc deposition, and electron beam physical vapor deposition.

In the current study, the electron beam physical vapor deposition (EBPVD) technique is used to deposit the catalytic metal onto a semiconductor, resulting into

creation of a Schottky contact between the metal and semiconductor interface. In this technique the target (source) metal is evaporated to the gas phase by bombardment of its surface with high-energy electrons driven from a tungsten filament. Then, the gas phase is transported and condensed on a substrate surface. The deposition rate in EBPVD process can be varied from 1 nm/min to 100 mm/min depending on materials and desired structures. After preparation of TiO_2 substrates, 15 nm Pt layer at a rate of 0.02 nm/s is deposited on these substrates using VARIAN e-beam depositor equipment at the Nanocore Facility of UIC (Figure 2.6). This deposition is done under high vacuum (10^{-6} Torr) and the surface temperature is maintained at 100 ˚C.

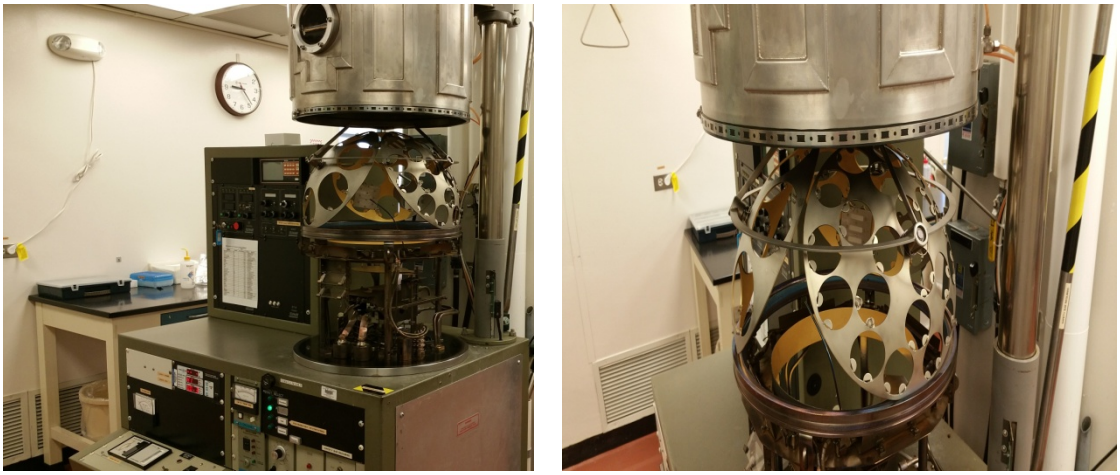

Figure 2.6. VARIAN e-beam depositor equipment used for deposition of 15 nm Pt on TiO_2 substrates

2.3 Characterization Techniques

2.3.1 X-Ray Diffraction (XRD)

X-ray diffraction (XRD) is a non-destructive technique used to analyze crystalline compounds and identify the crystallographic structure and atomic composition of various materials such as metals, thin film coatings, ceramics, and semiconductors. An x-ray tube, a sample holder, and a detector are the main parts of an x-ray diffractometer. An x-ray tube contains two basic elements: a metal target and a tungsten filament which are used as a cathode and an anode, respectively. When a high voltage is applied between the tungsten filament and metal target (usually Cu), a beam of high-energy electrons will be emitted from the hot filament and will bombard the metal target. This results in creation of x-rays that exit the tube via a window which provides a monochromatic x-ray source. A beryllium window is commonly used for this purpose. As these monochromatic x-rays interact with the sample surface, they will be diffracted when Bragg's law is satisfied:

$$n\lambda = 2d\,sin\,\theta \tag{2-2}$$

where,

n = is an integer called the order of reflectance

λ = is the wavelength of monochromatic x-rays

θ = is the angle between the incident rays and normal to the crystalline plane

d = is the space between two adjacent atomic planes (lattice spacing) used to identify the structure and atomic composition of the crystalline material

Constructive interference occurs when the path difference traveled by the incident rays reflected off of two crystalline planes is equal to an integer number of the wavelength. The mean size of crystallites within powder samples can be calculated by the Scherrer equation:

$$L = \frac{K\lambda}{\beta \cdot cos\,\theta} \tag{2-3}$$

where L is the mean crystalline size, K is the shape factor typically between 0.9 and 1, λ is the wavelength, and β is the line broadening at half of maximum intensity.

In the current study, a Siemens D5000 XRD Diffraktometer is used to investigate the crystal structure of the oxide layers formed on titanium substrates. Also, the relationship between anodization parameters (applied voltage, concentration of the electrolyte, time duration, etc.) and the thickness of oxide layers will be discussed in the following chapters.

2.3.2 Scanning Electron Microscope

A scanning electron microscope (SEM) generates magnified images of a surface sample using a focused beam of electrons produced by an electron gun placed inside a vacuum chamber, rather than light waves used in conventional light microscopes. The electron beam moves downward through electromagnetic fields and is focused into a very fine spot on the surface of the object being investigated. As the beam strikes the sample, secondary electrons, backscattered electrons, diffracted backscattered electrons, photons, and visible light are ejected from its surface. Consequently, secondary electron (SEI) and

lower secondary electron (LEI) detectors collect the secondary electrons and create final three-dimensional SEM images. Although SEM is an expensive technique and may damage the sample due to interactions between the incident electrons and its surface, it has remarkable advantages including: a large depth of field, a highly resolved and magnified topographical image, and minimal sample preparation actions.

In this thesis, a Hitachi SEM S-3000N model at the research resource center of UIC is used to scan the Pt-coated TiO_2 samples. It will be shown that the Pt metal is deposited on an uneven and mesoporous TiO_2 surface.

CHAPTER 3

CHEMICAL TO ELECTRICAL ENERGY CONVERSION IN MESOPOROUS Pt/TiO_2 SYSTEMS

(Figures 3.19, 3.20, 3.21, 3.22 and the related discussion were previously published as Karpov, E.G., Hashemian, M.A., and Dasari, S.K. "Chemistry-Driven Signal Transduction in a Mesoporous Pt/TiO_2 System". *J. Phys. Chem. C*, 2013, 117 (30), 15632–15638.)

3.1 Introduction

Direct observations of reaction-induced electric charge flow between the metal and semiconducting phases of composite nanocatalytic systems are instrumental for understanding chemical surface dynamics, development of smart chemical sensors, and in situ monitoring and control of catalytic reactions (Mildner et al. 2006; Krix et al. 2007; Karpov and Nedrygailov 2009; Hagemann et al. 2010). Hot electron currents (chemicurrents) in catalytic Schottky structures, using a continuous Pt or Pd nanofilm grown on a single-crystal semiconductor substrate, were discussed recently as evidence of nonadiabaticity in surface reactions (Park and Somorjai 2006; Hervier et al. 2009; Karpov et al. 2013). The possibility of direct conversion of surface released chemical energy into continuous electrical signals was investigated using the Schottky barrier to separate the chemically induced electric charges. Such Schottky structures can be viewed as models of the actual industrial catalysts, and their chemicurrent signals can be representative of the adsorptive and catalytic processes on the surface. However, realization of practical transducer applications of the chemicurrents in the continuous

Schottky structures was mitigated with the low hot electron yield at normal surface temperatures and also contamination of the signal with thermally driven currents at elevated temperatures. These limitations could be overcome by significantly increasing catalytic activity of such transducer devices. In particular, usage of amorphous and porous semiconducting oxide layers, rather than single-crystal supports, could enhance surface diffusion of reactants and increase concentration of centers of adsorption and recombination. In this view, electrochemically grown titania layers can be of interest because well-defined and stable TiO_2 thin films can be fabricated using simple and reproducible procedures (Sedona et al. 2005; Diamanti and Pedeferri 2007; Sikora et al. 2011). Thin films and nanotubes of titania already attracted much attention as passive chemical sensors (Varghese et al. 2003; Shimizu et al. 2007; Chen et al. 2012). More recently, studies of anodic TiO_2 films in the context of reaction-driven currents and active (self-powered) devices were initiated as well (Schierbaum and Achhab 2011; Stella et al. 2011). A mesoporous TiO_2 layer grown on Ti foil with a Pt paste contact applied to the oxide surface was shown to give very strong reaction current responses, and three possible mechanisms were suggested to contribute to the observed EMF: thermal, hot electron, and hydrogen concentration effects (Iwahara 2004). A positive potential on the Pt contact was reported in all instances (Schierbaum and Achhab 2011).

In the present work, we aim to consider chemical transducer properties of a mesoporous Pt/TiO_2 system with a well-defined Pt phase that would be both nanodispersed on the oxide surface and also possess an electrical continuity for a proper charge collection function. For this purpose, a wide-area Pt mesh or grating layer of nanometer thickness was deposited onto a mesoporous TiO_2 layer grown on a solid Ti

substrate. Here, the entire Pt nanomesh and the Ti substrate serve as two electrical terminals of the chemical transducer device. The fabricated structure was able of a continuous oxidation of hydrogen gas to water starting at room temperatures. In contrast to the earlier studies (Schierbaum and Achhab 2011), a second (slow) mode of the reaction was clearly seen on the recorded reaction current kinetics in addition to the usual (fast) oxyhydrogen reaction on the nanodispersed Pt. This slow mode induces a strong and stationary reaction current at room-temperature conditions; the direction of this current corresponds to a negative potential on the Pt phase, and therefore its production cannot be explained with any of three mechanisms mentioned above. A mechanism of proton spillover from Pt to TiO_2 phases of the system is suggested in this thesis to explain the origin of the electromotive force of this current. Furthermore, the overall current kinetics contains many autonomously formed features, including peaks and alterations of the charge flow direction, corresponding to various transient and competing processes on the bifunctional catalytic surface. This behavior represents a potential of the discussed material system as a chemical transducer for analytical and sensing applications.

3.2 Experimental Procedure

3.2.1 Sample Fabrication

3.2.1.1 TiO_2 Preparation Using Plasma Electrolytic Oxidation Process

TiO_2 substrates were prepared by plasma electrolytic oxidation (mentioned in section 2.2.1) of 36 × 12 × 0.5 mm^3 strips of standard (ASTM B265) 0.989 pure Ti metal in 3 M sulfuric acid solution. During the anodization process, different samples were obtained by varying the cell voltage while the current was maintained at a constant value

(current-mode control). The anozization parameters are listed in Table VI. For example, sample 1 was prepared as the following: within the first 3 min of the process the cell voltage grew to 90 V, when the micro arcs in the electrolyte started to appear. After 12−15 min, the voltage went gradually to 150 V, and during the next 5 min it slowly approached a nearly constant value of 155 ± 2 V. The process was terminated abruptly after 20 min of total time, disregard of a particular value of the cell potential. The cell current was maintained at the constant value 1.2 A during the entire process. A 200 mL glass beaker containing the sample and electrolyte was cooled by placing it in a 4.5 L cuvette filled with water at room temperature. The same procedure was applied for the preparation of other samples.

Table VI. Anodization parameters and the measured thickness for different TiO_2 samples prepared in 3 M H_2SO_4

Sample	Current (A)	Voltage (V)	Thickness (μm)
1	1.2	150	6
2	0.85	150	6
3	0.85	155	10
4	1.2	162	11

In order to form micro arcs on the surface of titanium samples, the applied cell voltage must exceed the dielectric breakdown potential of the growing oxide film. After fabrication of TiO_2 samples, they were rinsed in DI water to remove the electrolyte from their surface.

3.2.1.2 Pt Deposition on top of the TiO_2 Substrate

In the next step, a wide-angle PVD sputtering of 0.9995 pure Pt was performed in a 10^{-6} Torr vacuum through a 34 × 10 mm^2 mask on top of the porous TiO_2 surface at the rate 0.02 nm/s. The deposited layer thickness was monitored with an Inficon quartz microbalance, and the source shutter was closed abruptly when the thickness reading reached 15 nm. This thickness of Pt was considered because its hot electron mean free path is on the order of tens nanometers (section 1.2.1). Finally, two Ag wires of 0.5 mm diameter were attached with an SEM grade Ag paste at the two opposite ends of the Pt nanomesh. The remaining (active) area of the Pt nanomesh not covered with Ag was about 2.8 cm^2. The Pt/TiO_2 sample is shown in Figure 3.1. In order to make an ohmic contact between Ti and TiO_2 substrate, a small portion of the oxide layer from the edges of the structure was removed prior chemicurrent measurements.

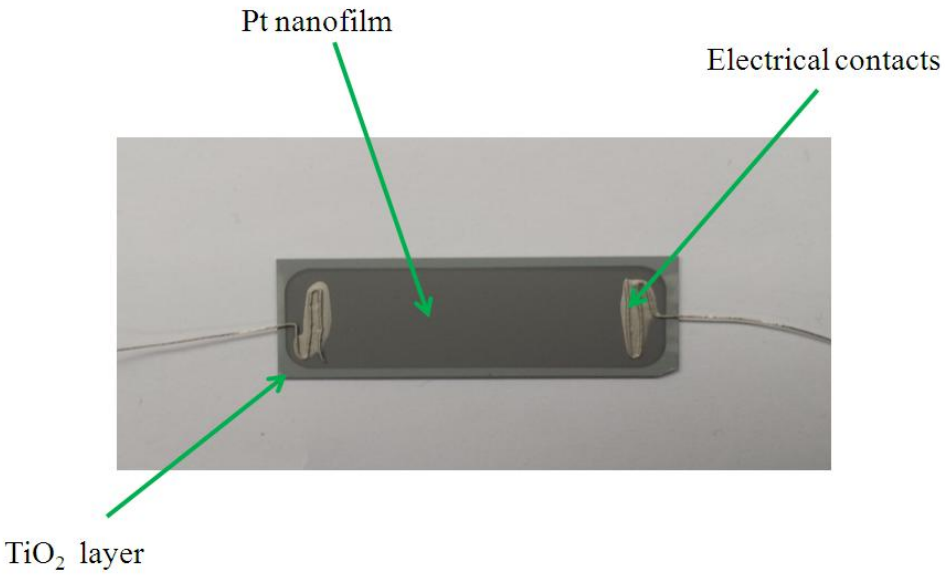

Figure 3.1. Image of Pt/TiO_2 /Ti sample

3.2.2 XRD and SEM of TiO_2 Layer

In order to understand the relationship between the chemicurrent generated and morphological properties of Pt/TiO_2 structure, XRD and SEM techniques were carried out. Figure 3.2 shows the XRD spectra for samples 1−4. It can be seen that the titanium oxide layer had higher amounts of rutile phase in samples 3 and 4 in comparison to samples 1 and 2. This implies that increasing the anodization voltage decreased the amount of rutile phase in TiO_2 layer. Also, the presence of the anatase peak at 25˚ in samples 3 and 4 indicates the less amounts of rutile phase formed on their surface. From this it could be inferred that the generation of chemicurrents depends on the TiO_2 thickness and amounts of rutile phase, thinner samples containing more rutile phase generated higher chemicurrents.

(a)

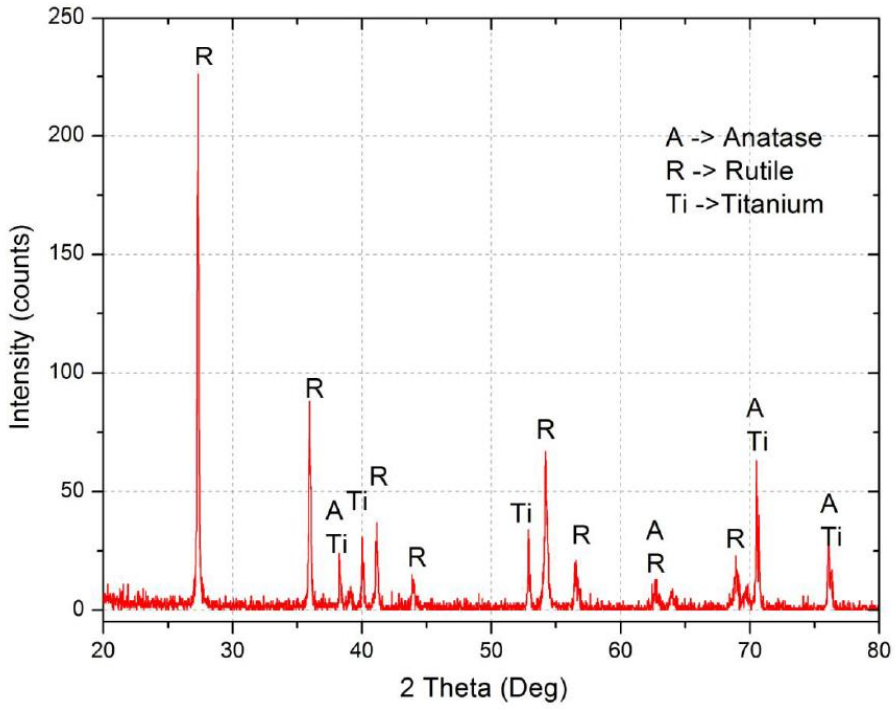

(b)

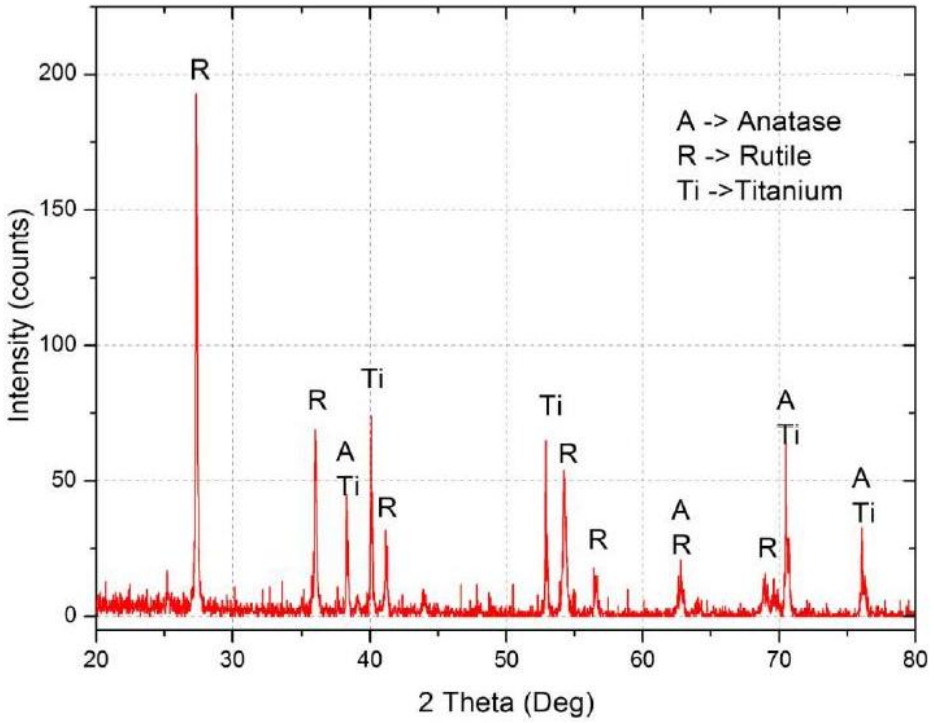
A -> Anatase
R -> Rutile
Ti ->Titanium
Intensity (counts)
2 Theta (Deg)
0
50
100
150
200
20
30
40
50
60
70
80
R
R
A
Ti
Ti
R
Ti
R
R
A
R
R
A
Ti
A
Ti

(c)

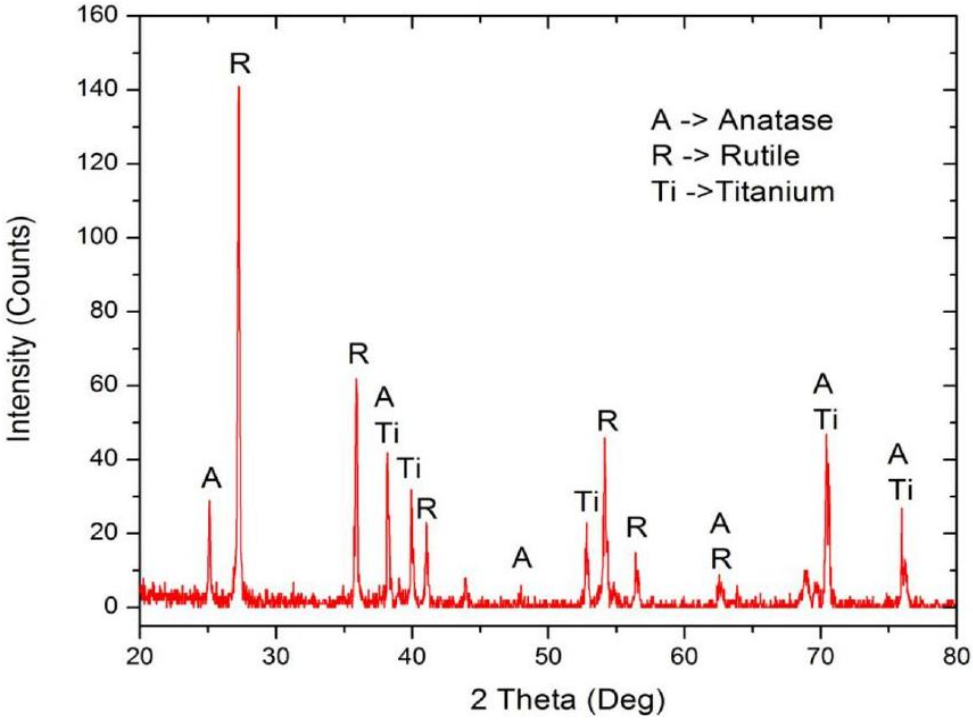
A -> Anatase
R -> Rutile
Ti ->Titanium
Intensity (Counts)
2 Theta (Deg)
0
20
40
60
80
100
120
140
160
20
30
40
50
60
70
80
R
A
R
A
Ti
Ti
R
A
Ti
R
R
A
R
A
Ti
A
Ti

(d)

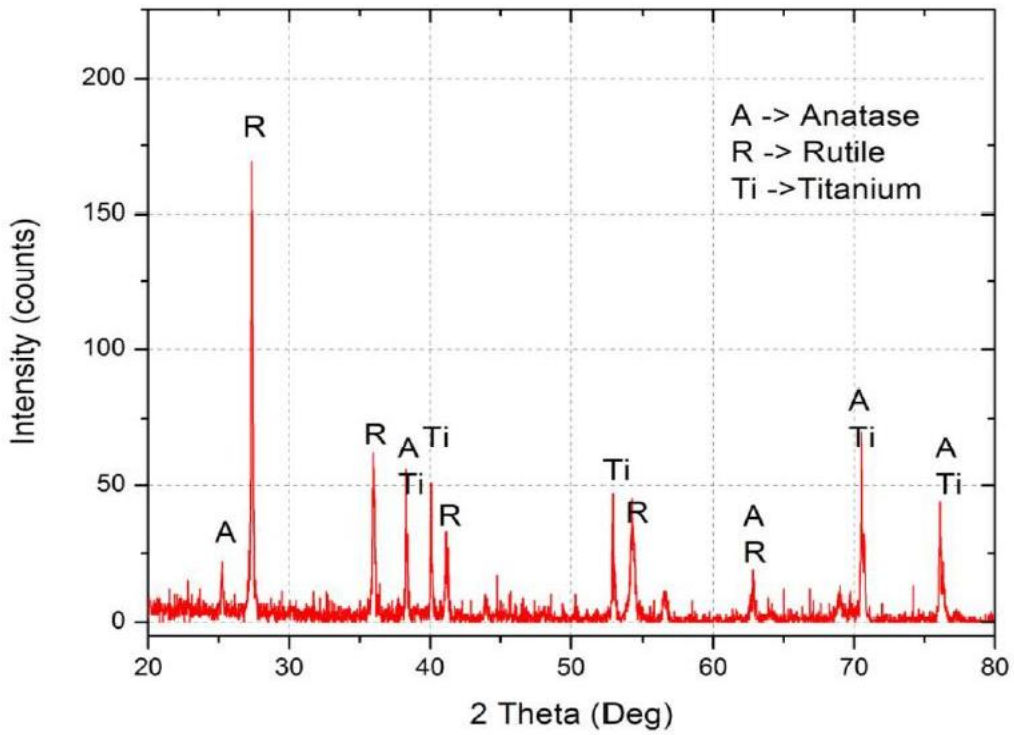

Figure 3.2. XRD spectra for (a): sample 1, (b): sample 2, (c): sample 3, and (d): sample 4

Figure 3.3 presents the SEM images of sample 1 obtained from 1 and 20 μm resolutions. SEM scans of the Pt-coated TiO_2 surface did not reveal any changes in the surface structure at the resolution of Figure 3.3a, implying that Pt metal was deposited as a nanometer thickness blanket layer with multiple openings (holes) at the positions of the TiO_2 surface pores (Figure 3.3b). We will refer to such a Pt nanophase as a nanomesh hereafter.

(a) (b)

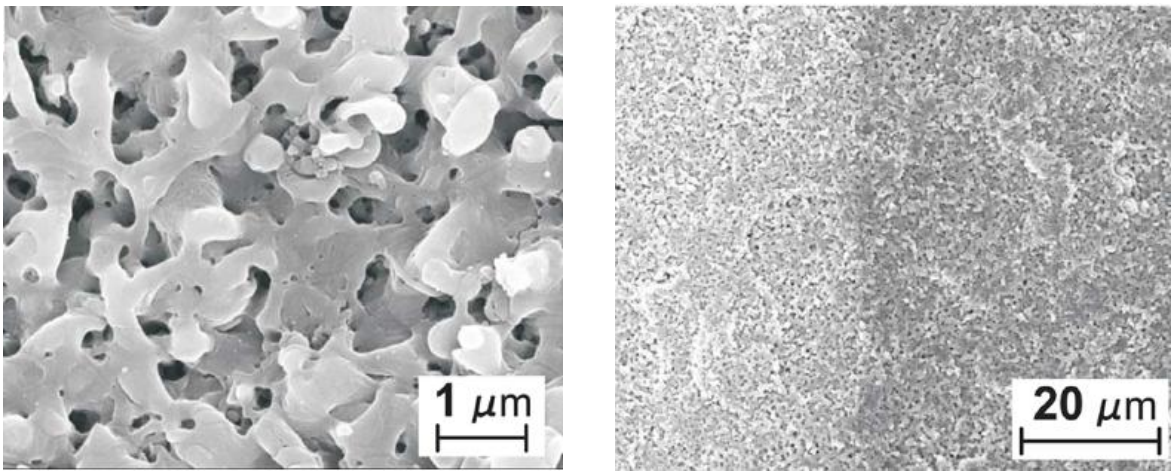

Figure 3.3. SEM scans of sample 1: (a) mesoporous TiO_2 phase and (b) the interface between the Pt-coated and pristine oxide surfaces

Figure 3.4 shows the SEM images of samples 1-4 with 10 μm resolution. As seen from this figure, a mesoporous TiO_2 layer was obtained for all samples. Once again it can be said that the deposited Pt nanolayer had an uneven mesh-like topography with multiple openings corresponding to the location of pores on the oxide surface. In order to correlate the relationship between the surface morphology and chemicurrent, better techniques must be used in the future.

(a)

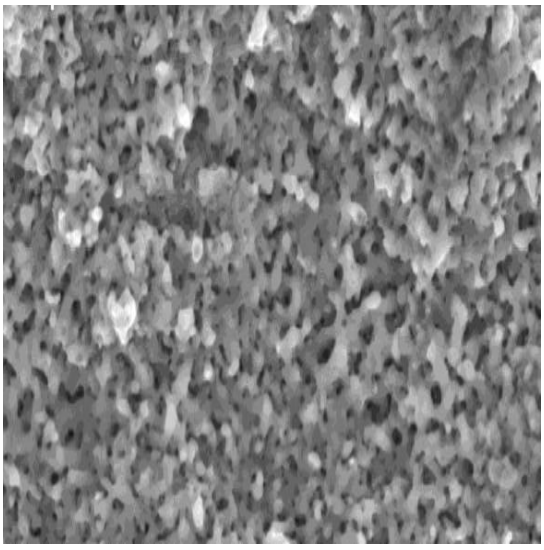

(b)

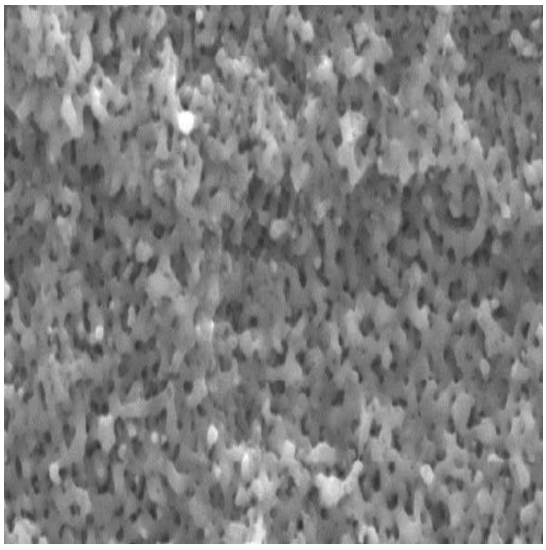

(c)

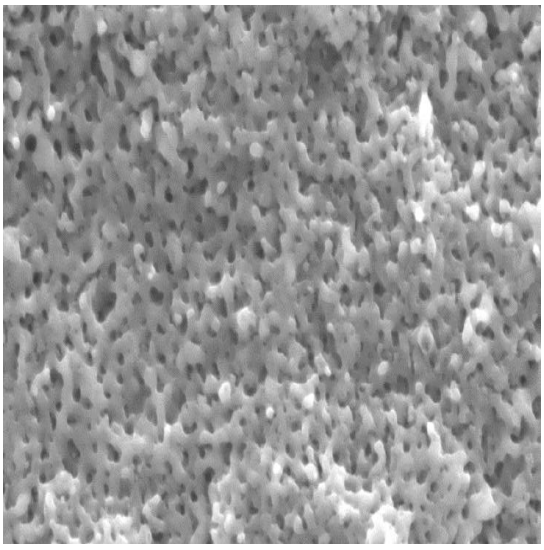

(d)

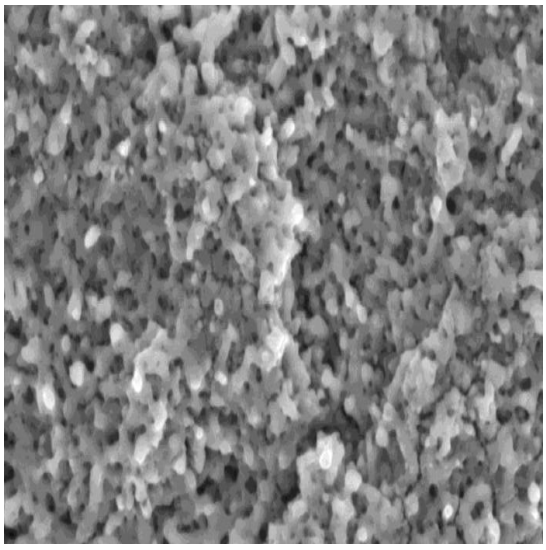

Figure 3.4. SEM imaging (10 μm resolution) for (a): sample 1, (b): sample 2, (c): sample 3, and (d): sample 4

3.2.3 Experimental Setup

The experimental setup used in this work is shown in Figure 3.5. For the reaction current studies, the Pt/TiO_2/Ti sample was mounted inside a spherical 4.5 L vacuum/environmental chamber using a copper clamp attached to one of the copper pins (2.4 mm diameter) of a 2.75″ CF electrical feedthrough flange. The nanomesh contacts (the Ag wires) and wires of a Pt resistance temperature detector (RTD) element were attached to four other pins of the same feedthrough flange. The RTD sensor had a ceramic body of dimension 2 × 2 × 0.8 mm^3 (Omega F2020-100).

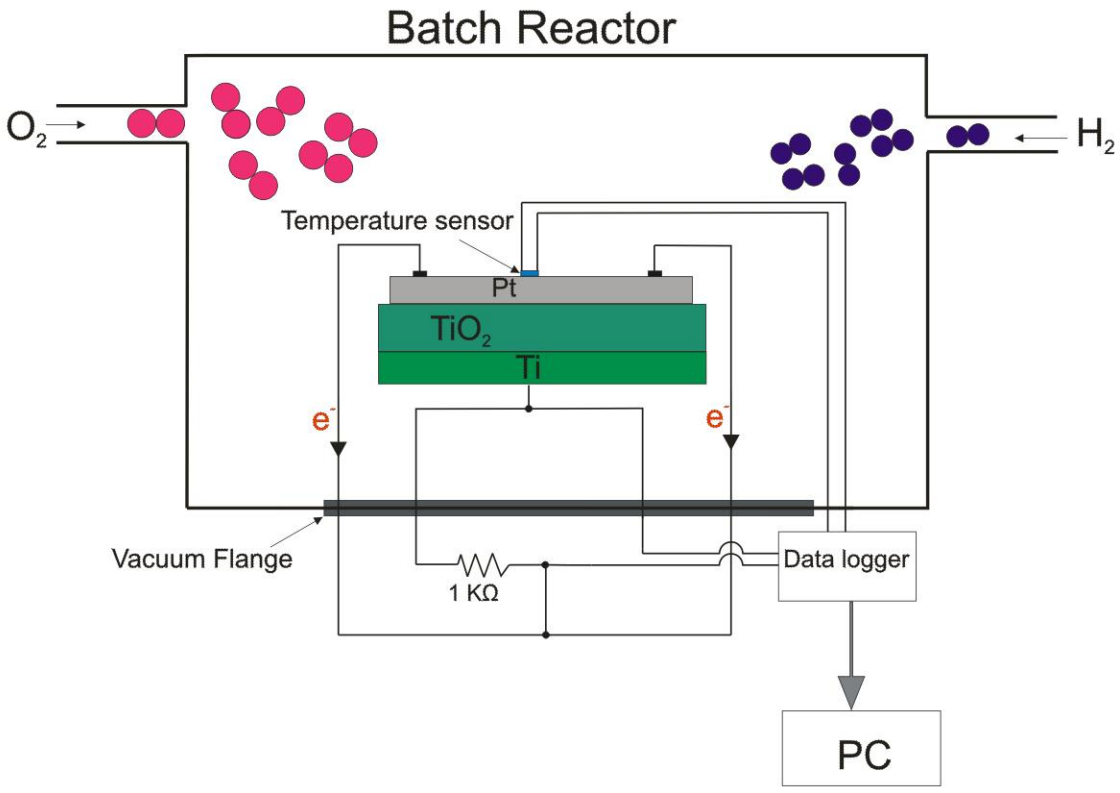

Figure 3.5. Schematic of vacuum chamber used for the chemicurrent measurements

The temperature sensor was brought in contact with the sample in the middle of the Pt nanomesh area and supported with its own connection wires only, avoiding usage of adhesive substances. Generally, an in situ temperature method based on the Pt layer resistance could give more accurate results, unless the oxide support showed such a dramatic resistance effect in a H_2-rich environment able to distort the Pt resistance readings (Karpov et al. 2012).

Electrical signals from the sample were registered on a 1 kOhm load resistor connected in parallel to a data logger (see Figure 3.5). A residual pressure of 10^{-7} Torr was reached in the chamber each time prior to addition of the reactive gases. The gases were admitted to the chamber when the sample surface was at room temperature; i.e., no external heating was used for reaction initiation purposes, and any observed sample heating was only due to the reaction process itself. In all experiments, gases were admitted to the chamber diffusively at a rate of 2−3 Torr/s. The chamber was also equipped with capacitive pressure transducers and a mass spectroscopy setup to record the total and partial pressure kinetics. All the reaction current studies were performed in the batch reactor mode, in which the analytical chamber was entirely cut off from the environment and the pumping unit prior to the admission of reactive gases.

3.3 Results and Discussion

3.3.1 Catalytic Combustion of O_2/H_2 Mixtures on a Pt/TiO_2 System

Several preliminary experiments were carried out on sample 1 (anodized at 1.20 A and 150 V) to understand the catalytic activity of this Pt/TiO_2 system. This was done by varying the concentrations of hydrogen and oxygen in the chamber which resulted in

different catalytic combustion regimes. Figure 3.6 shows the experimental data when 16 Torr of hydrogen was added twice to a pure oxygen atmosphere (160 Torr).

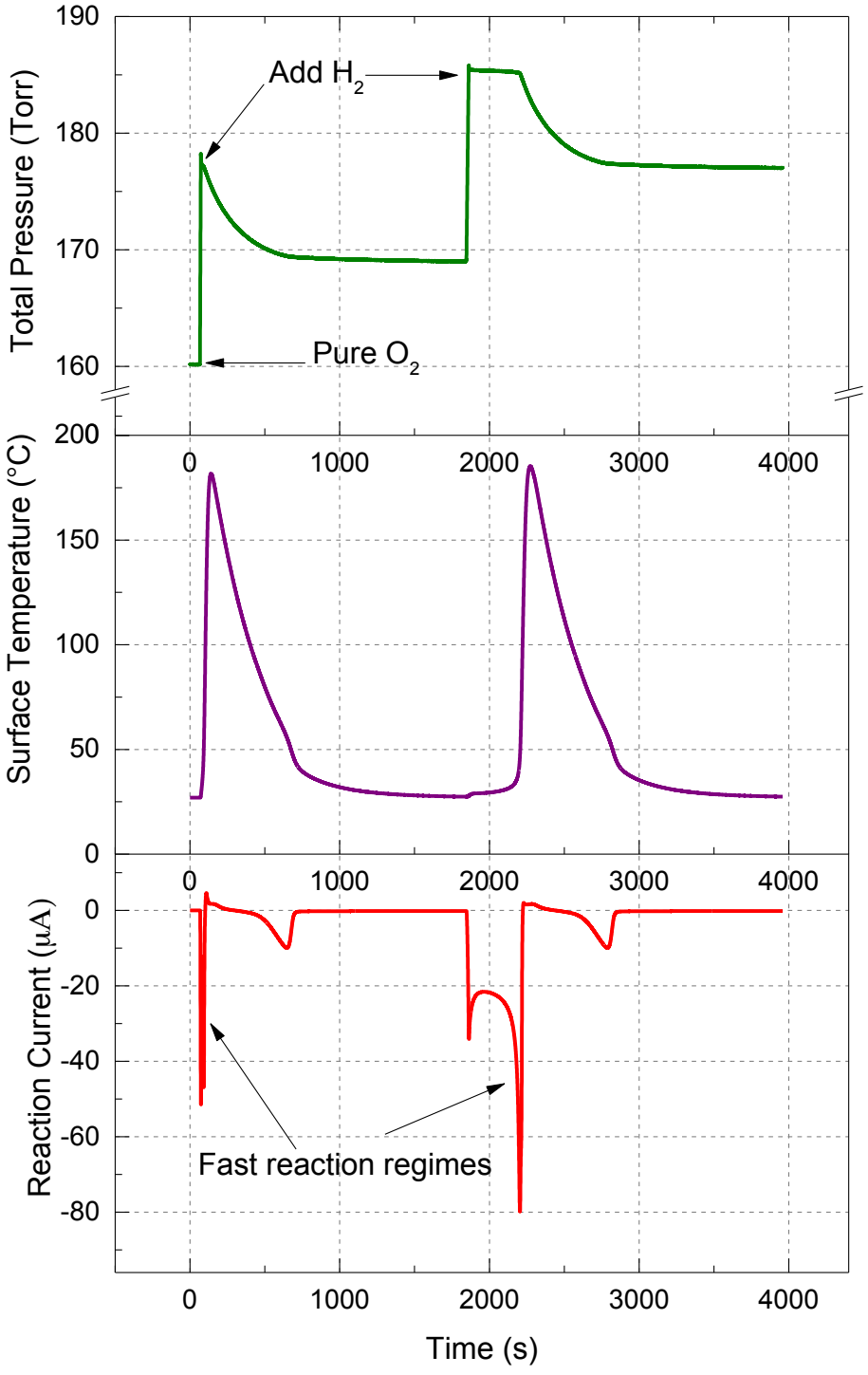

Figure 3.6. 16−16 Torr sequence of H_2 addition to 160 Torr of O_2

The temperature and total pressure kinetics indicate that after addition of first 16 Torr of H_2 the temperature increased immediately from 27 to 160 ˚C and the pressure dropped from 176 to 169 Torr. In this work, this catalytic initiation is refereed as a fast reaction regime. Furthermore, when the surface temperature was cooled down to the room temperature (27 ˚C), 16 Torr of hydrogen was again added to the existing mixture. The second addition of H_2 caused the fast reaction reinitiated and the temperature increased to about 165 ˚C. From Figure 3.6 it can be seen that the currents generated due to the fast reaction are about 50 and 80 μA for the first and second addition of hydrogen, respectively. This reaction-induced current is reproducible and can be attributed mostly to the hot electron mechanism. The autonomous features of this current will be discussed briefly in section 3.3.4.

Figure 3.7 represents the kinetics of the total pressure, surface temperature, and reaction-induced current of the sample when 10, 10, and 10 Torr of H_2 were added to 160 Torr of O_2. The first two addition of H_2 resulted in the fast reaction regimes, similar to the previous experiment. However, for this particular mixture the final values of surface temperature were smaller (110 and 125 ˚C) due to less amount of H_2 (20 compared to 32 Torr). After about 30 min the surface temperature reached to the room temperature and 10 Torr of hydrogen was added to the existing mixture. As seen from Figure 3.7, further addition of H_2 did not invoke the fast mode again but produced 10 μA current and lead to a new reaction mode, called the slow reaction regime. During the slow reaction mode, the surface temperature did not increase and maintained at room temperature. This is the main characteristic feature of the chemicurrent generated in the slow reaction regime.

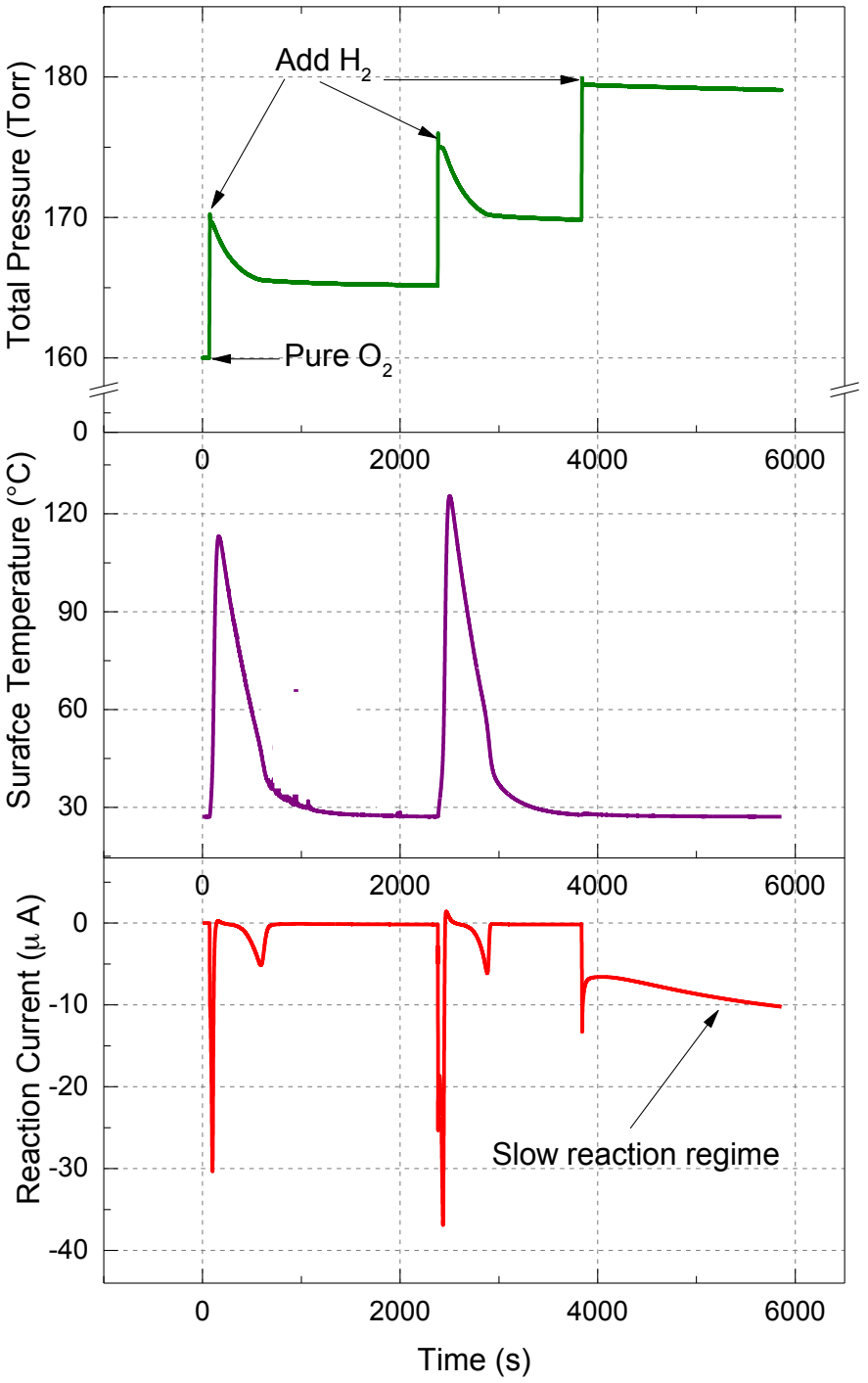

Figure 3.7. 10−10−10 Torr sequence of H_2 addition to 160 Torr of O_2

The results from Figure 3.6 and Figure 3.7 indicate that a minimum of 10 Torr H_2 is necessary for initiation of the fast reaction regime. Next, we decreased the amount of hydrogen and investigated the correlation between the pressure of H_2 and fast reaction mode. Figure 3.8 shows the results when 6, 5, 5, 6, and 10 Torr sequence of hydrogen were added to 160 Torr of oxygen, resulting in three fast and two slow reactions.

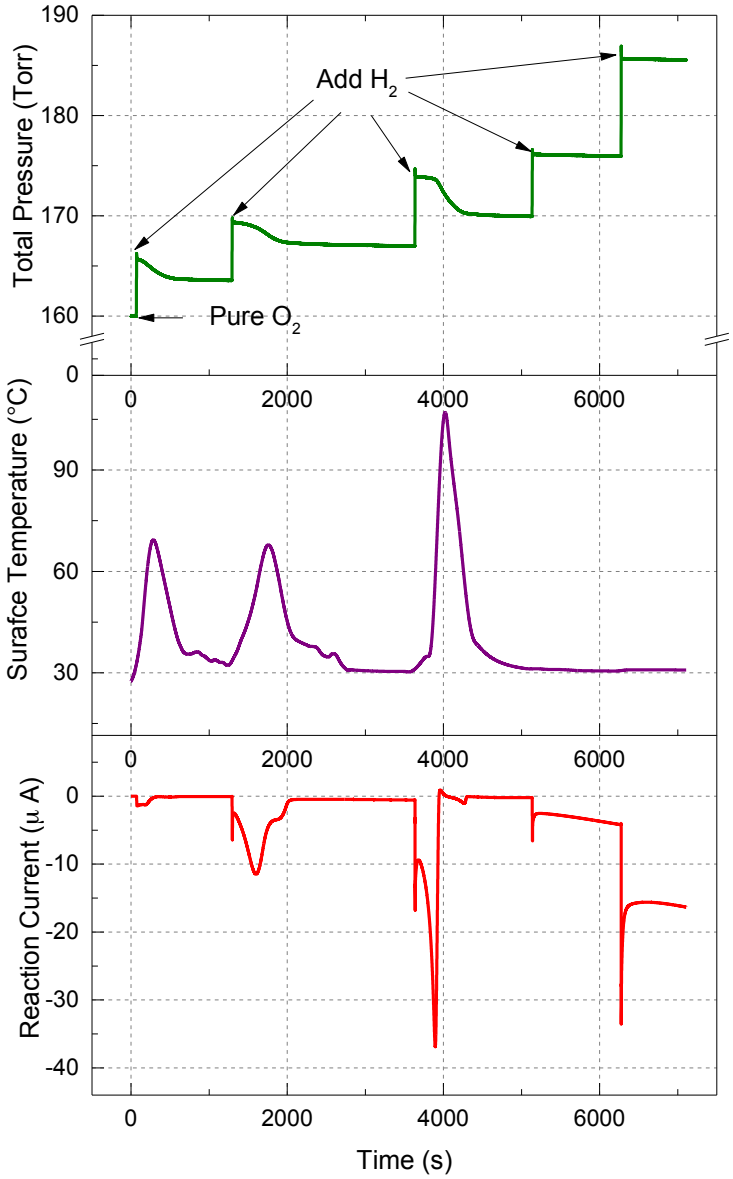

Figure 3.8. 6−5−5−6−10 Torr sequence of H_2 addition to 160 Torr of O_2

The results from Figure 3.6 and Figure 3.8 show that the fast reaction mode can occur by adding 16 Torr of hydrogen either in one step or multiple steps. It can be seen that the fast reaction initiated with adding only 6 Torr of hydrogen. Since this amount of hydrogen was not enough to react with the all existing oxygen, the fast reaction happened two more times by adding more hydrogen. After the third fast reaction, the overall surface reaction switched to the slow reaction mode by the step-like increase of chemicurrent at times 5136 and 6274 s, yielding 5 and 16 μA for the fourth and fifth addition of H_2, respectively.

In order to determine the effect of oxygen pressure on the fast and slow reaction modes, various amount of oxygen was added to 16 Torr of hydrogen existed in the chamber. Figure 3.9 shows the kinetics of the total pressure, surface temperature, and reaction current of the sample when 10, 10, 20, and 20 Torr of O_2 were added to 16 Torr of H_2. It can be seen that the fast reaction did not initiate until the fourth addition of O_2 (60 Torr). Also, the surface temperature increased sharply to 275 ˚C and the usual fast reaction current generated upon the fourth addition of O_2. It should be mentioned that the surface temperature increased slightly due to the third addition of O_2 (40 Torr), but it was not sufficient to initiate the fast reaction mode. These results are in good agreement with the experimental data that the fast reaction cannot be initiated in a mixture with less than 60 Torr of O_2 (it is not shown here).

Figure 3.10 shows the recorded data when 60 Torr of O_2 was added in one step to 16 Torr of H_2, resulting in the fast reaction and surface temperature of 200˚C. In this case, 50 min was needed for initiation of the fast reaction whereas it happened immediately in the condition of 160 Torr O_2 (see Figure 3.6).

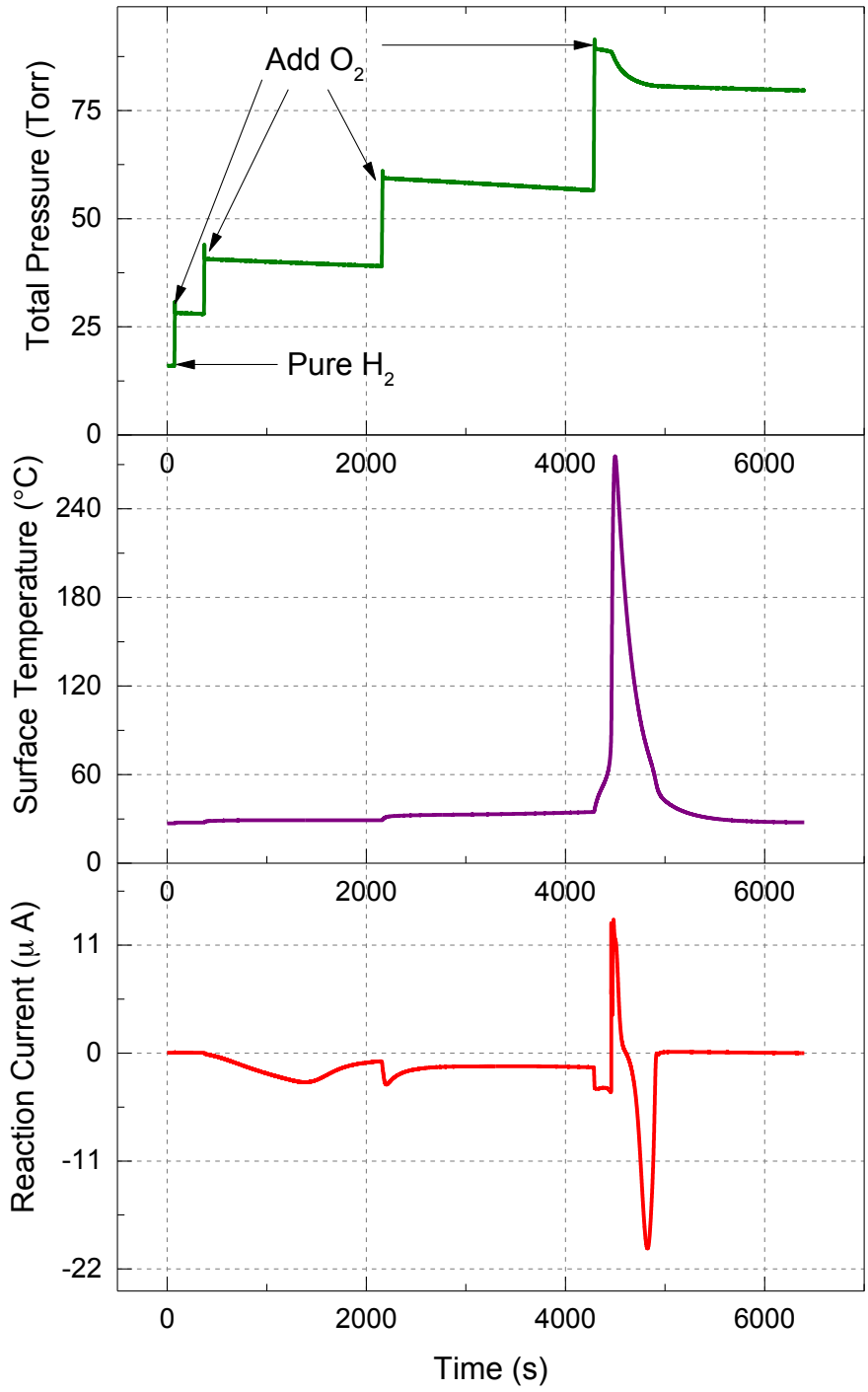

Figure 3.9. 10–10–20–20 Torr sequence of O_2 addition to 16 Torr of H_2

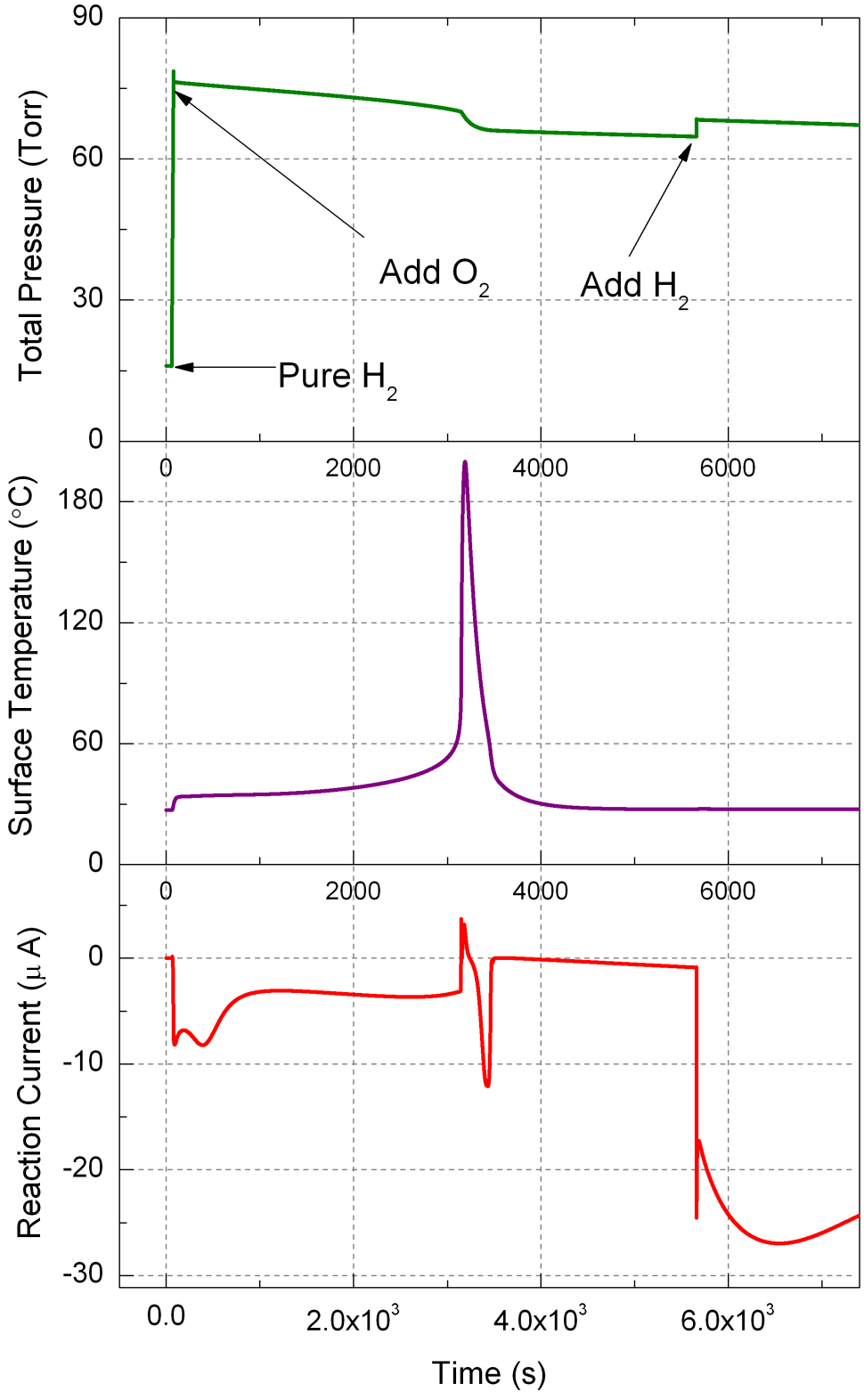

Figure 3.10. 60 Torr addition of O_2 to 16 Torr of H_2 (further addition of H_2 resulted in 27 μA chemicurrent)

As seen from Figure 3.10, a large chemicurrent (27 μA) was generated after the fast reaction regime upon admission of 5 Torr H_2. However, this current started to decrees after 17 min from addition of H_2 due to the small concentration of O_2 on the sample surface.

Figure 3.11 represents the surface temperature versus time when 16 Torr of H_2 was added to different pressures of O_2. It can be seen that the initiation (ignition) time of the fast reaction decreased with increasing of oxygen pressure. The fastest and slowest reactions occurred for 160 and 60 Torr of O_2, respectively. The surface temperature and ignition time for each pressure are presented in Table VI.

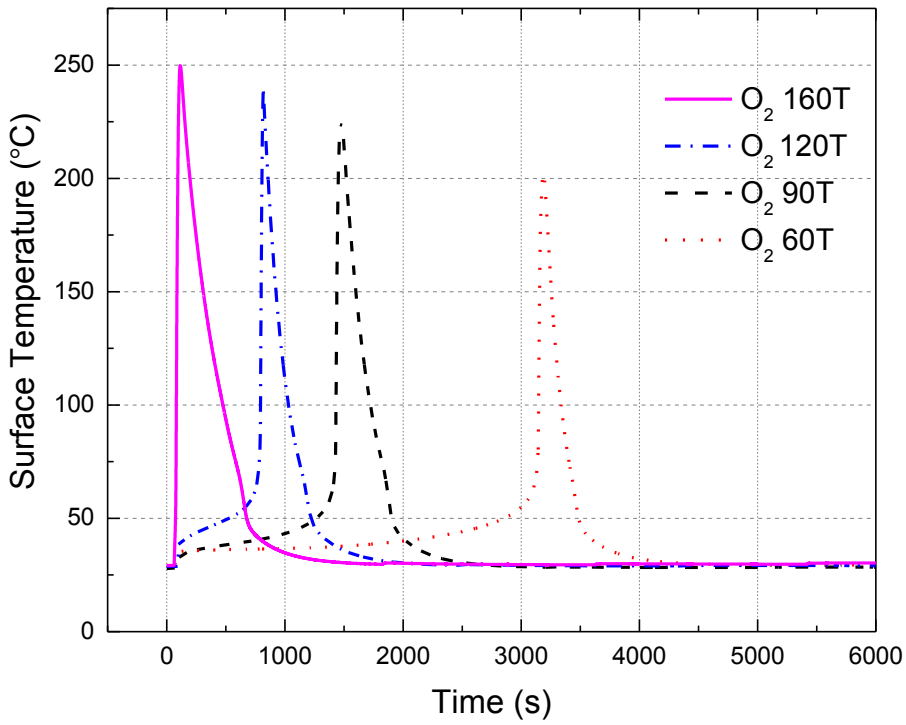

Figure 3.11. The surface temperature versus time for various pressures of O_2 with 16 Torr of H_2

Table VII. The surface temperature and ignition time obtained for different amount of O_2 in 16 Torr of H_2

O_2 Pressure (Torr)	Surface temperature (˚C)	Ignition time (min)
160	250	1
120	240	10
90	225	20
60	200	50

The data from Table VI indicate that the surface temperature had the same order of magnitude for all pressures of O_2 and the ignition time was strongly dependent on the concentration of O_2 in the mixture.

The preliminary results for chemicurrent measurements represented in Figure 3.6 to 3.11 were obtained from sample 1 and other samples showed the same qualitative behavior.

3.3.2 Chemicurrent Measurements in the Oxyhydrogen Mixture

The results obtained from the previous section revealed that 160 Torr of O_2 is the optimum pressure in the oxyhydrogen (O_2+H_2) mixture in the chemicurrent studies. This amount of O_2 initiates the fast reaction in a very short period of time and prevents further possible fast reactions when more H_2 is added to the mixture. Therefore, in this section we discuss about the chemicurrent measurements that were carried out only in 160 Torr of O_2 and different amounts of H_2. The experimental procedure for all fabricated samples (shown in Table VI) was similar. First, 160 Torr of O_2 was added to the pre-vacuumed

chamber where the sample is mounted. Then, 16 Torr of H_2 was added to initiate the fast reaction on the sample, resulted in high surface temperature in the order of 200 ˚C. After 30 min when the surface temperature cooled down and reached to the room temperature, 5 Torr of H_2 was added 5 times with an interval of 30 min between each step.

Figure 3.12 shows the kinetics of total pressure, surface temperature, and chemicurrent obtained from sample 1 (anodized at 1.20 A and 150 V). The data was recorded by the help of instruments explained in chapter 2. Upon the first (16 Torr) addition of hydrogen, the fast reaction was initiated immediately and a large current of 110 μA was produced. This value can be attributed to the thermal current since the oxidation of hydrogen to water is an exothermic reaction. As can be seen from Figure 3.12, the current in the fast reaction regime was generated when the surface temperature increased sharply due to addition of hydrogen. Then, it approached to zero once the temperature started to decrease. When the sample surface cooled down to the room temperature (27˚C), 5 Torr addition of hydrogen resulted in generation of 8 μA chemicurrent (first step) and the it increased from 8 to 30 μA by adding the next 5 Torr of hydrogen (second step). The third, fourth, and fifth step were formed with the similar procedure and resulted in 44, 48, and 60 μA, respectively. Although the magnitude of chemicurrent increased after addition of hydrogen in each step, the slope of stationary current started to decrease from the third step and reached to the saturation state. This indicates that sample surface was occupied with the oxyhydrogen gas mixture and adding more hydrogen could not enhance the slope of generated chemicurrent. Figure 3.13 shows the chemicurrent generated in oxyhydrogen atmosphere from sample 2 which was anodized at 150 V and 0.85 A in 3 M sulfuric acid electrolyte.

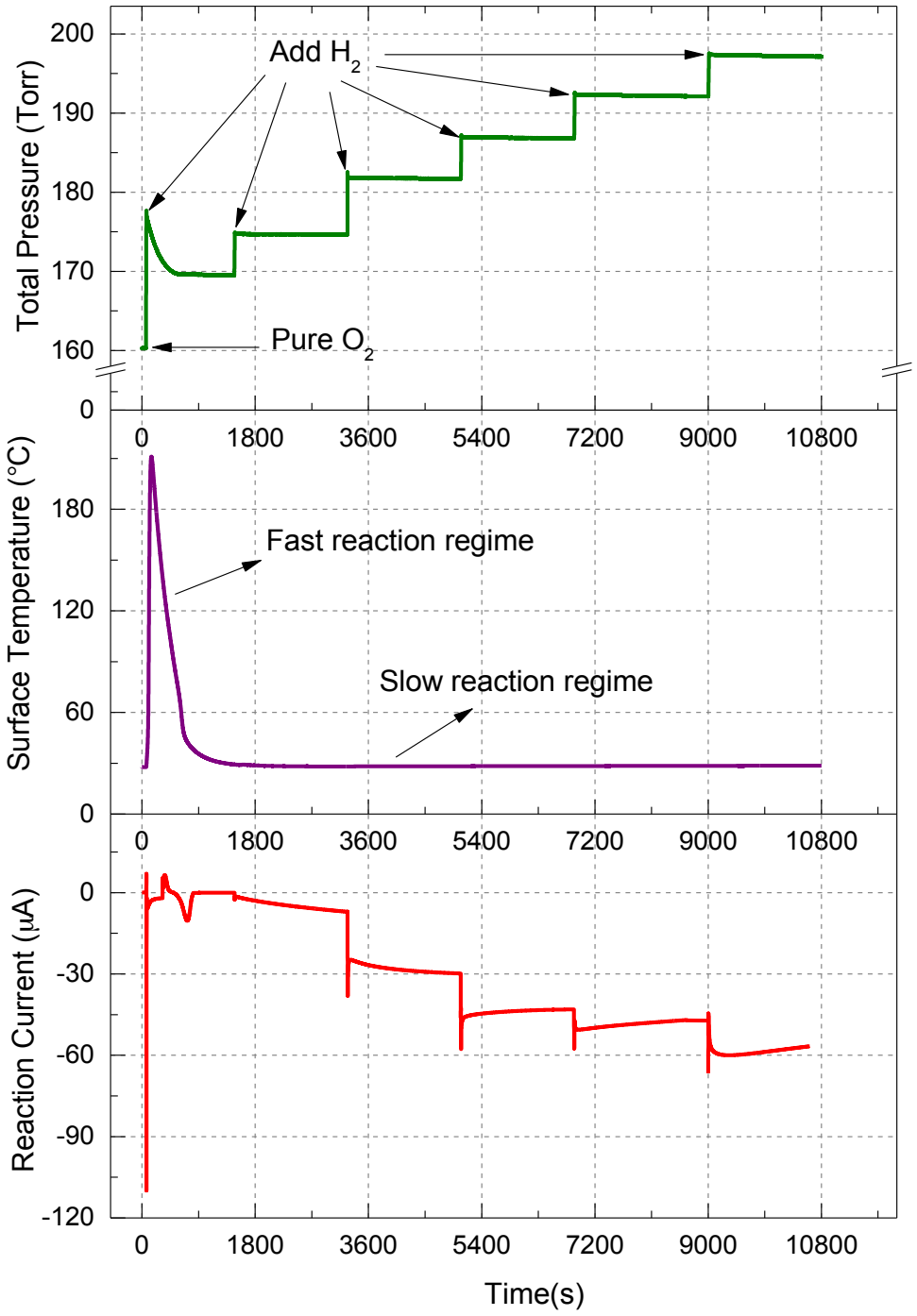

Figure 3.12. The kinetics of total pressure, surface temperature, and chemicurrent obtained in 5 steps addition of hydrogen to a pure oxygen atmosphere: sample 1

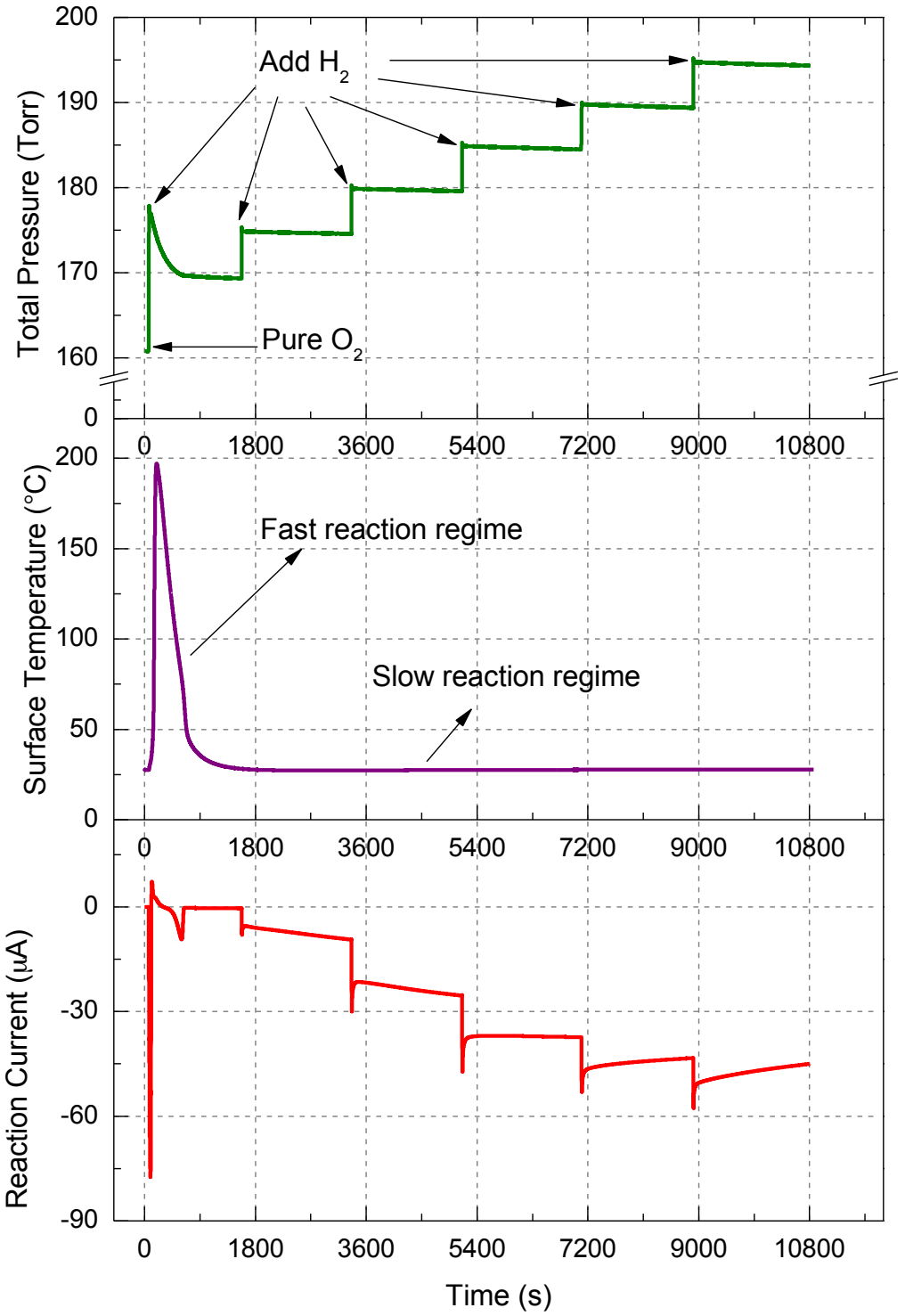

Figure 3.13. The kinetics of total pressure, surface temperature, and chemicurrent obtained in 5 steps addition of hydrogen to a pure oxygen atmosphere: sample 2

It can be seen from Figure 3.13 that the chemicurrent generated from sample 2 is in the same order of magnitude compared with sample 1 in the fast and slow reaction regimes. However, the stationary current slope of sample 2 in the third step remained almost constant during the slow reaction regime, in contrast to the third step of sample 1. Also, the ultimate value of chemicurrent obtained in the fifth step of sample 2 is slightly less than the current produced in sample 1 (see Figure 3.12).

Figure 3.14 and 3.15 show the kinetics of total pressure, surface temperature, and chemicurrent obtained from sample 3 (anodized at 0.85 A and 155 V) and sample 4 (anodized at 1.20 A and 162 V), respectively. The magnitude of currents generated from the fast reaction for these samples was in the same order with samples 1 and 2 and the surface temperature reached to 200−210˚C in all samples. However, the chemicurrents generated due to the slow reaction regime from samples 3 and 4 were smaller compared to samples 1 and 2. The maximum chemicurrents of 13.5 and 8.5 μA were observed for samples 3 and 4, respectively.

The generation of chemicurrent is related to the thickness of TiO_2 layer. As seen from Table VI, the oxide layer thickness of samples 3 and 4 (11 μm) were larger than samples 1 and 2 (6 μm). Although the Pt thickness was the same for all samples (15 nm), the thinner samples generated larger chemicurrents compared to the thicker ones. This indicates that the smaller Schottky barrier formed at the thinner TiO_2 oxide layer can enhance the chemicurrent generation in slow reaction mode.

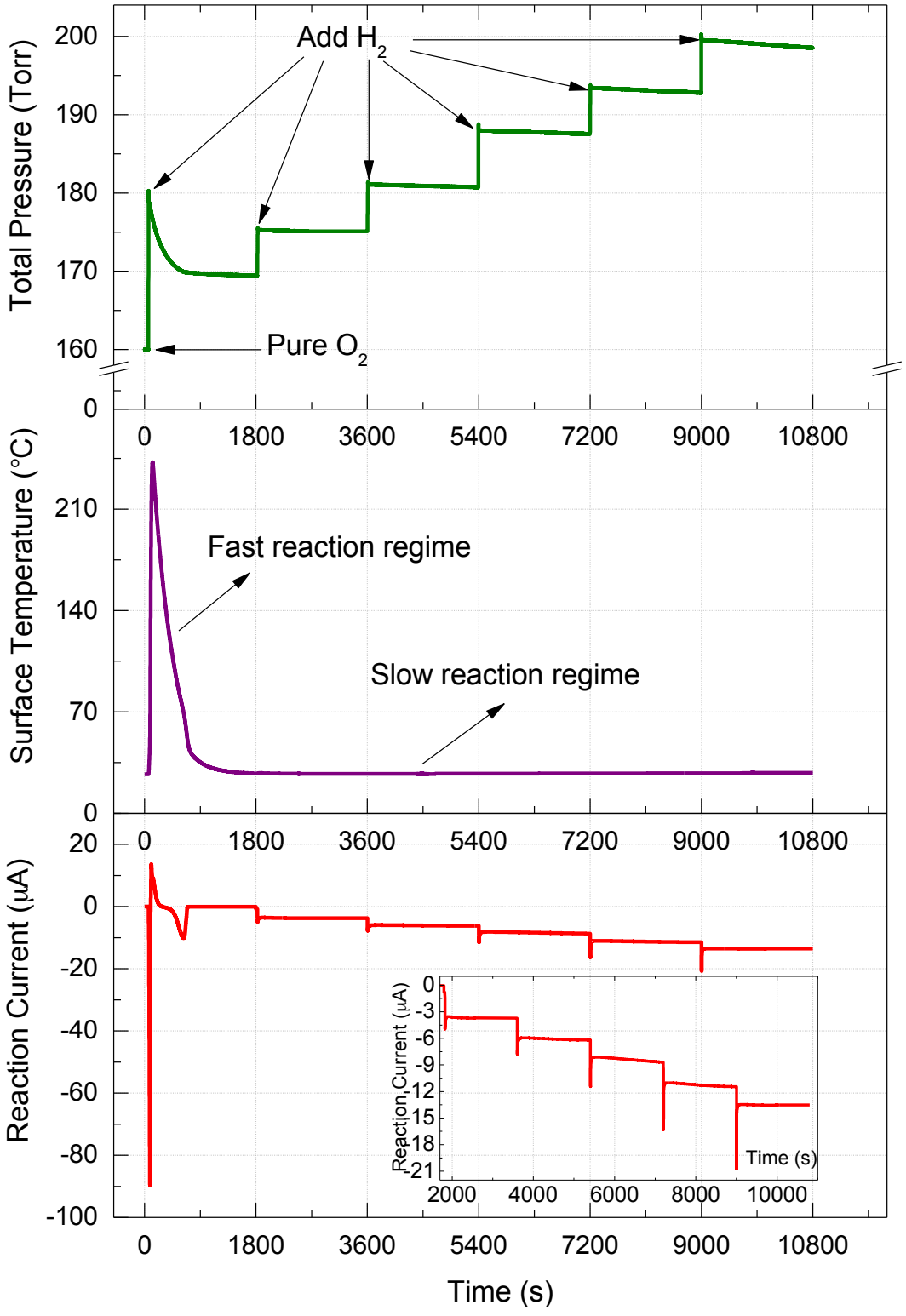

Figure 3.14. The kinetics of total pressure, surface temperature, and chemicurrent obtained in 5 steps addition of hydrogen to a pure oxygen atmosphere: sample 3

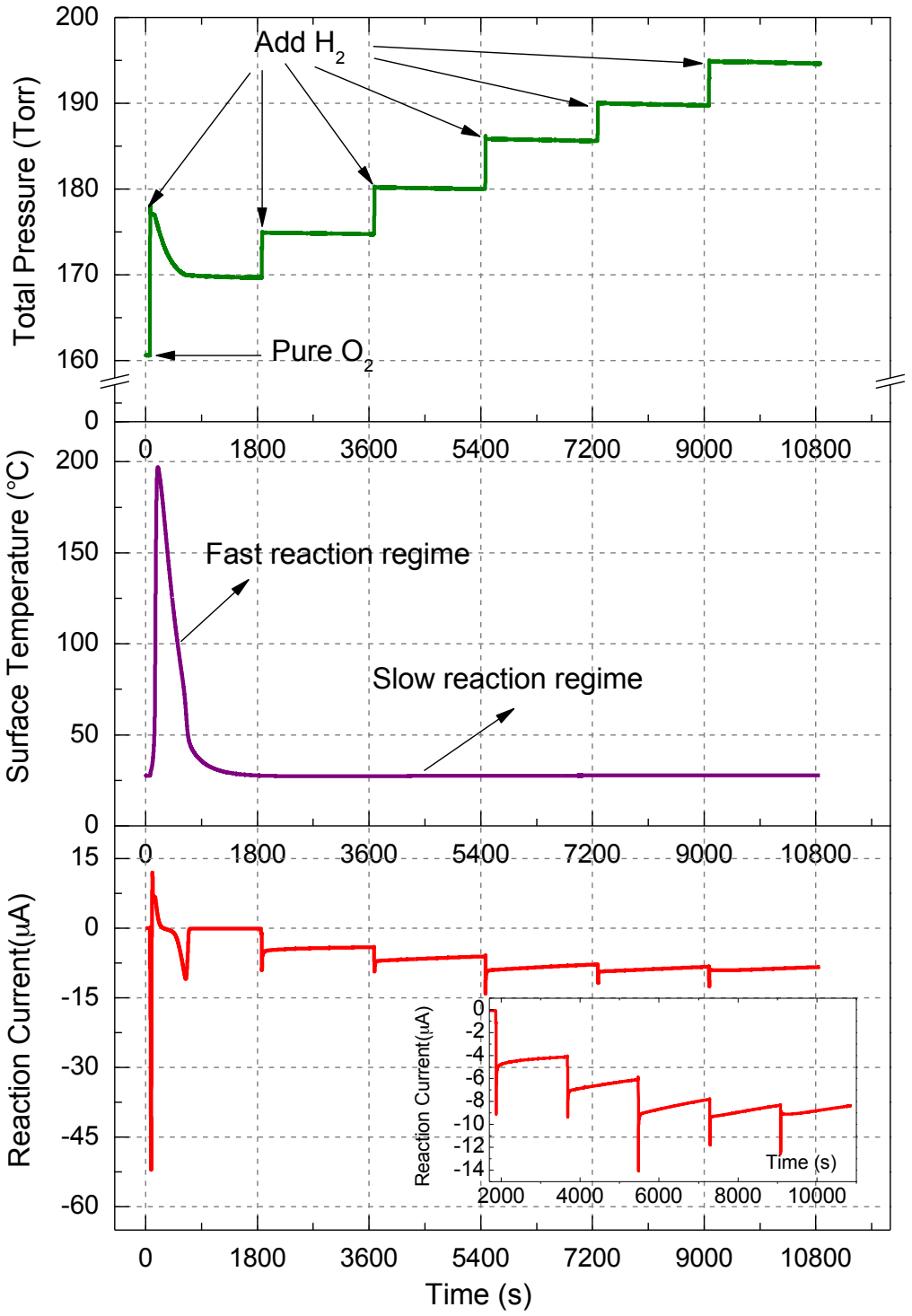

Figure 3.15. The kinetics of total pressure, surface temperature, and chemicurrent obtained in 5 steps addition of hydrogen to a pure oxygen atmosphere: sample 4

The chemicurrents generated after 30 min in each step for all samples are presented in Table VIII.

Table VIII. The chemicurrents produced in each step for samples 1−4

Sample	Chemicurrents generated for different steps (μA)				
	Step 1 (3600 s)	Step 2 (5400 s)	Step 3 (7200 s)	Step 4 (9000 s)	Step 5 (10800 s)
1	8	30	44	48	60
2	10	26	38	44	45
3	4	6	9	11	13.5
4	4	6	8	8.5	8.5

3.3.3 Long-term Kinetics of the Chemicurrent Generated During the Slow Reaction Regimes

The results obtained from section 3.3.2 revealed that the generation of chemicurrent depends on the reaction time and the amount of hydrogen added in each step. In order to investigate the effect of reaction time on the chemicurrent produced in the slow reaction mode, sample 1 was selected due to its high chemicurrent yield. Figure 3.16 shows the long-term kinetic of chemicurrent generated in the first step addition of H_2. Here, 5 Torr of H_2 was added to the chamber after the fast reaction (at time 1800 s) and kept for about 150 min, resulting in 8 μA chemicurrent. It can be observed that the

reaction current continuously increased (reverse polarity) while no more hydrogen was added to the system.

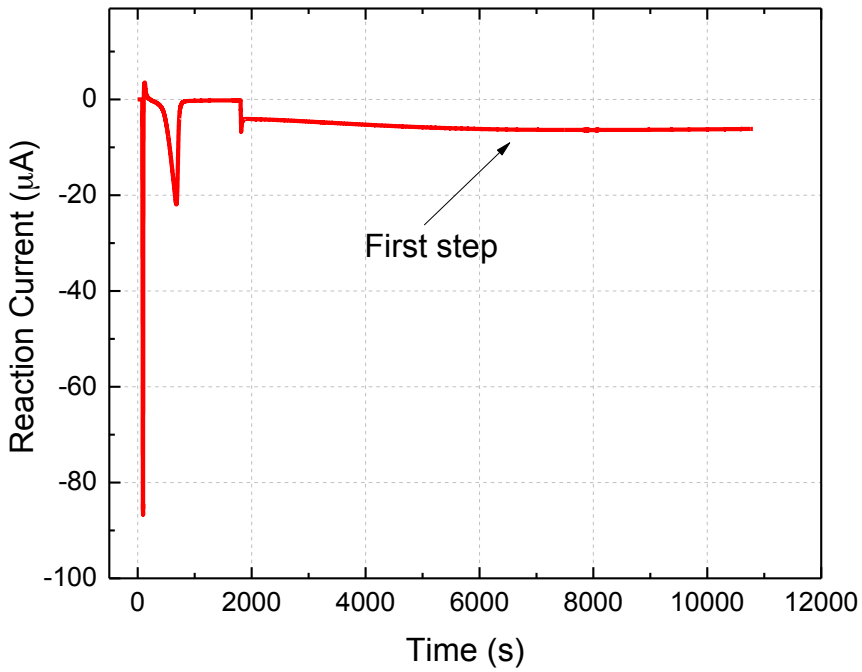

Figure 3.16. The long–term kinetic of chemicurrent generated in the first step

Figure 3.17 and 3.18 show the stationary reaction current generated in the third and fourth step, respectively. In both cases, a large chemicurrent of 38 μA was produced over long periods of time at room temperature. However, the chemicurrent decreased faster in the fourth step compared to the third step which can be due to the saturation of surface from hydrogen gas. These results are in good agreement with the results obtained from Figure 3.9 and Table VIII.

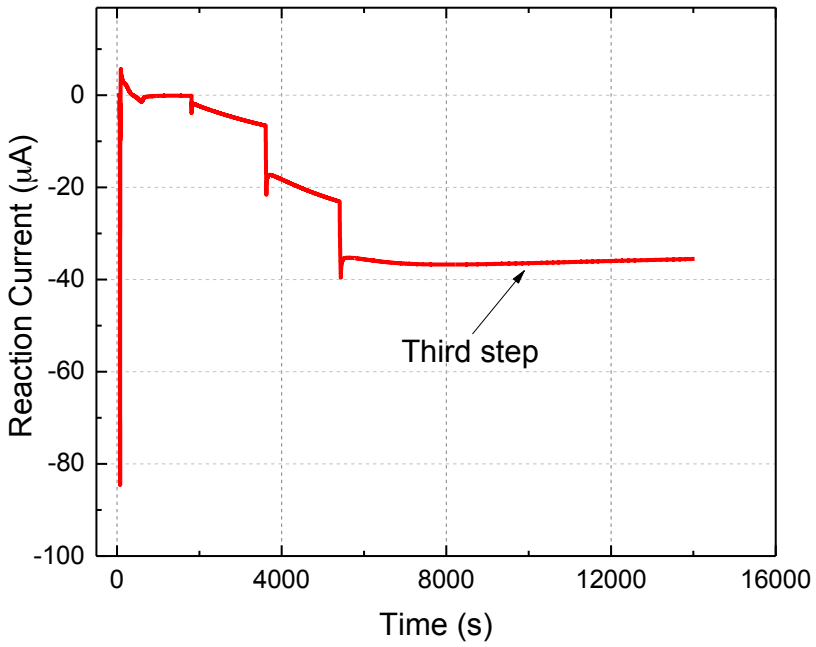

Figure 3.17. The long–term kinetic of chemicurrent generated in the third step

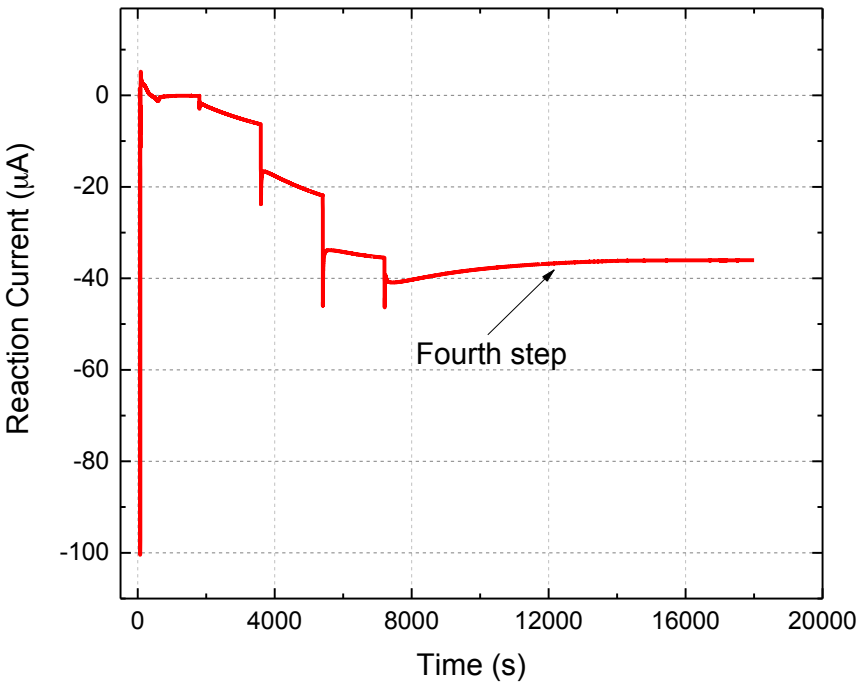

Figure 3.18. The long-term kinetic of chemicurrent generated in the fourth step

Perhaps the most interesting results were observed for a step like 16−5−5 Torr sequence of H_2 addition to a pure O_2 (160 Torr) atmosphere, as shown in Figure 3.19. Here, the temperature and total pressure kinetics indicate that a fast reaction resulting in 180 °C surface temperature occurs upon the first (16 Torr) addition of hydrogen, and this reaction seems to extinguish by the time 630 s. On the other hand, partial pressure of the remaining H_2 gas in the chamber at that time was typically 1 Torr. The fast reaction somewhat prepares the surface for the slow reaction mode that never occurs for the first hydrogen admission. The Pt phase may completely be covered with hydrogen adsorbate species by the 630 s turning point. Once started, the slow reaction occurs in a very robust manner. Further addition of H_2 by the 5 Torr portions performed upon cooling of the sample to room temperature does not invoke the fast mode again but increases the slow reaction rate as indicated by the step-like increase of the current at times 1850 and 3850. As can be seen, a large current of 30 μA was obtained over 150 min which is in good agreement with the results from Figure 3.19.

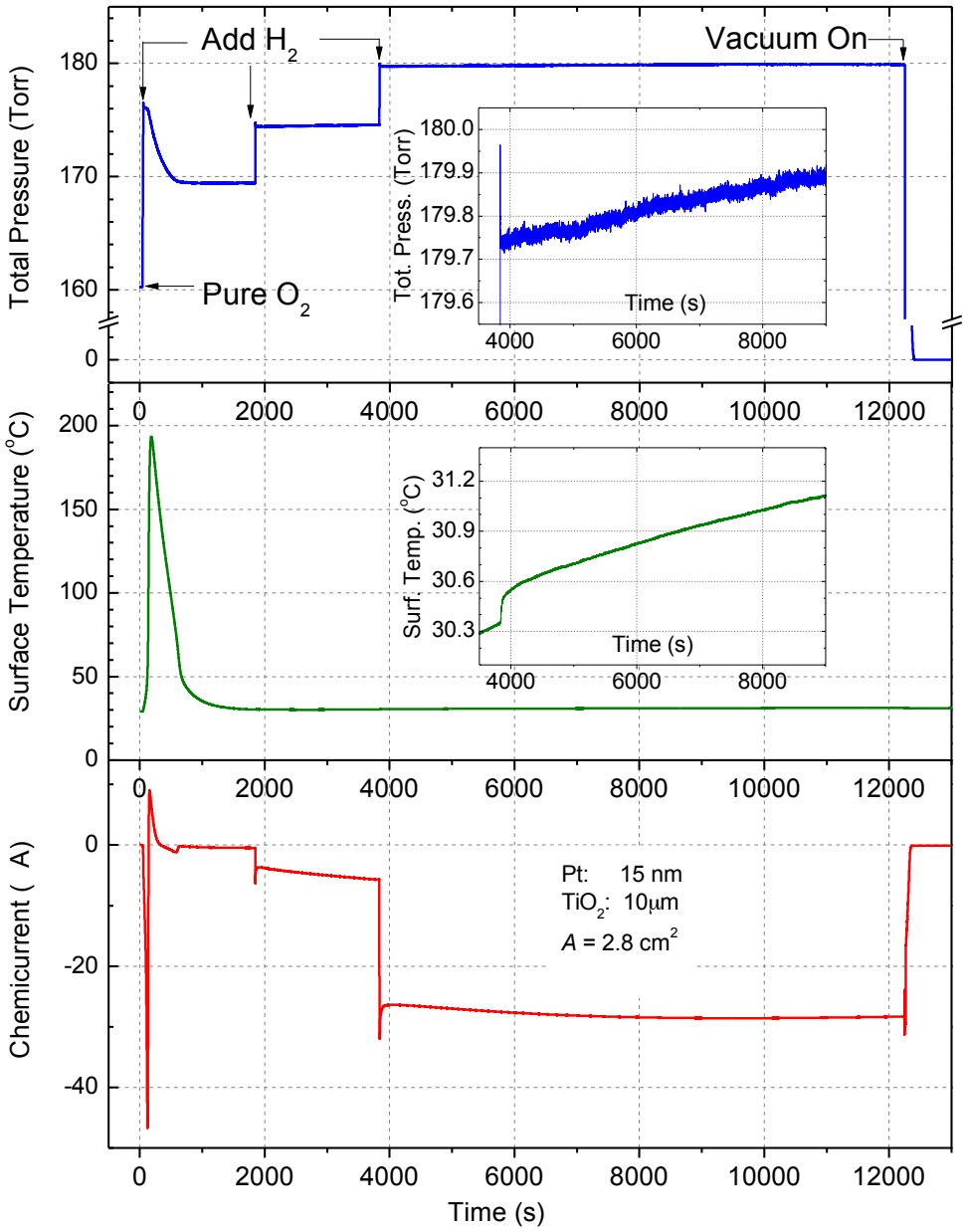

Figure 3.19. Result of a sequential (three-step) addition of H_2 to a pure O_2 environment. 16, 5, and 5 Torr H_2 was added to 160 Torr O_2 at times 50, 1850, and 3850 s, respectively

3.3.4 Fast Reaction Mode

The total pressure kinetics shown in Figure 3.19 indicate that the fast water production reaction occurs on the sample surface upon admission of the first (16 Torr) portion of hydrogen at rates up to 7×10^{18} molecules per second. No other external actions were performed over the system; while the resultant kinetics of the reaction-induced current showed a number of interesting autonomously formed features (see Figure 3.20). These include the initial negative peak (1) of 47 μA magnitude followed by a wider positive peak (2) of 9.5 μA value. After this peak, the current decreases, reverses its direction, and returns to the negative zone again without a delay or flexure at the zero level (3). Flexure points exist at other times between the positive peak (2) and the second negative peak (4). The reaction current then decreases to reach the turning point (5), where temperature drops below 60 °C, the fast reaction ends, and the current takes the stationary character (6). All these features of the current kinetics seen in Figure 3.20 must represent various elements and stages of the surface reaction process. For example, the initial peak (1) at 100 s could reflect an Eley−Rideal-type interaction of the adsorbate oxygen species and gas-phase hydrogen (Nienhaus 2002; Karpov et al. 2012) or/and a charge displacement effect as the device changes from a resistor to a diode. The wide positive peak (2) at 190 s is attributable to a combined effect of the thermoelectric and hot electron mechanisms discussed in the literature (Park and Somorjai 2006; Karpov and Nedrygailov 2009). These mechanisms correspond to a positive potential at the Pt terminal, should the structure be (naturally) heated at the Pt side only and have an n-type diode-like electrical characteristic in oxyhydrogen atmosphere. The current reversal points (3) and the second negative peak (4) at 580 s represent a competition of different

charge transfer processes between Pt and TiO_2 phases of the catalyst. Once the surface temperature drops below 60 °C, the turning point (5) occurs, after which the reaction current first acquires the stationary character (6). This stationary negative current recorded at room temperature at times beyond 630 s is the most unusual observation, and it is discussed in more detail in Sections 3.3.5−3.3.8.

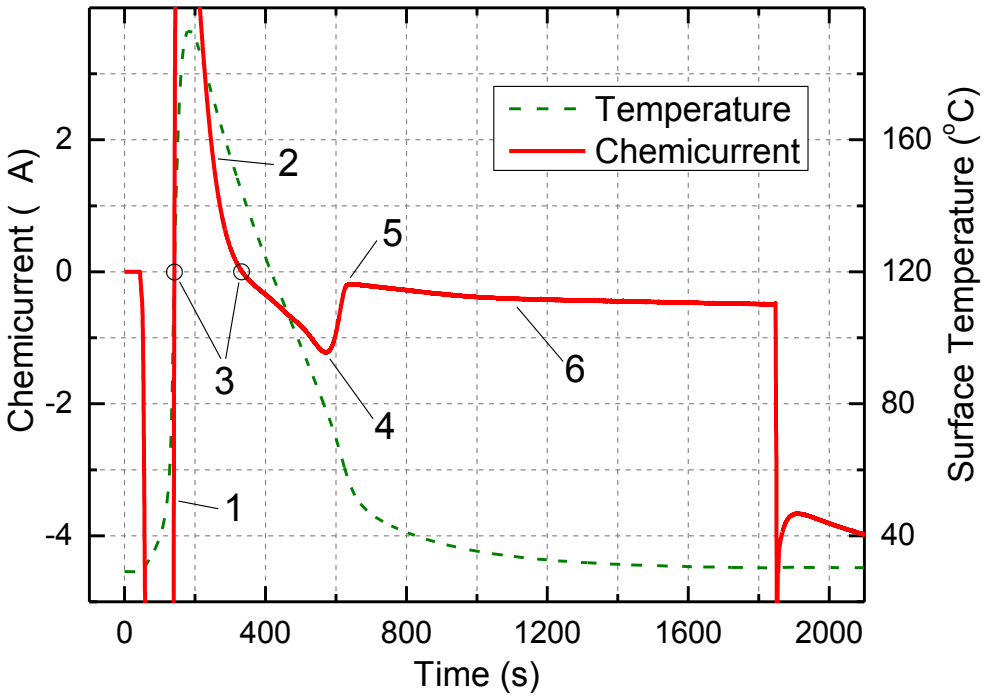

Figure 3.20. Autonomous features of the reaction-induced current formed between the first and second H_2 additions (50−1850 s): (1) initial negative peak due to adsorption and fast reaction initiation driven by the Pt phase, (2) positive peak by thermionic emission and hot electron currents at higher surface temperatures, (3) current reversals due to competing charge transfer processes on Pt and TiO_2 phases, (4) secondary negative peak–a quenching reaction effect, (5) fast reaction termination point (630 s), and (6) TiO_2-driven slow-rate process.

3.3.5 Slow Reaction Mode

The stationary negative current manifests a slow rate surface process accompanied by transfer of the negative charge from the n-type TiO_2 toward the Pt metal phase of the compound catalyst. Such a charge transfer corresponds to the forward bias current flow, and it is opposite in direction to the known hot electron chemicurrent (Krix et al. 2007; Karpov and Nedrygailov 2009). Admission of the further (5 Torr) portions of hydrogen gives the small transient peaks and step-like increase of this stationary current.

The maximum rate of this slow reaction was estimated in terms of hydrogen molecule consumption per unit time, k_{H_2}, using the pressure and temperature trends of Figure 3.19 insets and the ideal gas equation as the following:

$$k_{H_2} = \left(\dot{P} - \frac{P}{T}\right)\frac{2 \cdot V}{k_B \cdot T} \tag{3-1}$$

This estimate presumes a thermal equilibrium at temperature T between the sample surface and the gas phase of volume V and pressure p, which is a legitimate assumption for the slow reaction mode. This calculation gives k_{H_2}= 5.5 × 10^{15} s^{-1}, which is 1200 times lower than the maximal rate of the fast reaction discussed in Section 3.3.4. Due to the very low rate at which the slow reaction occurs, the nearly constant (room) temperature and pressure kinetics of Figure 3.19 alone might have been interpreted so that the entire reaction stops. However, observation of the large negative current clearly proves that the surface reaction is only switched between two different modes at the time 630 s. This second mode becomes better visible on the kinetics upon the subsequent

hydrogen addition at times 1850 and 3850 s. Thus, existence of the slow mode is realized here with the in situ observation of the reaction-induced current. Utility of the standard spectroscopic techniques for the same purposes would be complicated by the high pressure conditions in the gas phase. As a result, the observed slow mode of H_2 oxidation on micro-nanostructured Pt/TiO_2 surfaces might have been overlooked in the past.

3.3.6 Characterization of Electrical Properties

Room-temperature (RT) resistance of a freshly sputtered nanomesh measured between the Ag wires was about 560 Ohm, nearly independent of the source current and gas-phase conditions. A gradual decrease of the RT resistance was observed upon cyclic heating of the sample to 130 °C, and a stable value of about 340 Ohm was obtained. Resistance of the annealed nanomesh varied with temperature in a linear platinum-like manner. These observations proved the in-plane electrical continuity of the Pt nanomesh because resistance of the sample in vacuum measured across the oxide layer thickness was several orders of magnitude higher than the nanomesh resistance. For the discussion to follow, we note that the mesoporous sample morphology provides a very long interface of the two surface phases, Pt and TiO_2, and the reactive gas phase.

Electrical properties across the oxide layer thickness were significantly more complex, depending strongly on the gas phase conditions and the surface reaction flow. The I−V curve in vacuum or pure O_2 was about linear, low conductance, and symmetric for the positive (+V at Pt) and negative biases (see Figure 3.21 (curve A)). Also, a capacitance of 0.14 μF was measured separately with a Fluke 289 DMM for the sample in vacuum. In a pure H_2 atmosphere, an increase of conductance up to 6 orders of

magnitude depending on H_2 pressure was observed, while the overall I–V shape remained linear and symmetric (see Figure 3.21 (curves B, C, and D)).

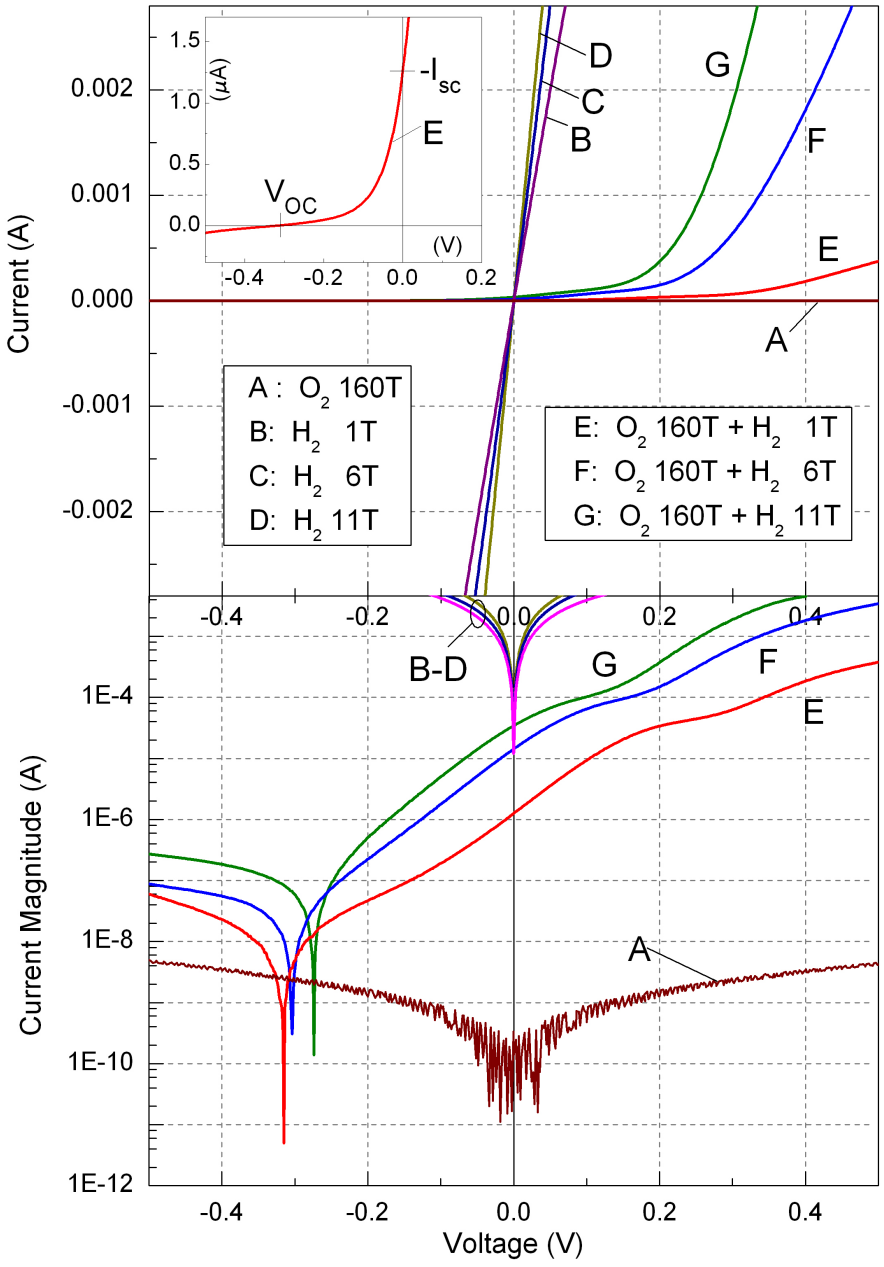

Figure 3.21. Current–voltage characteristics of the Pt/TiO_2(por)/Ti structure (+V at Pt) in pure O_2 (A), pure H_2 (B, C, and D), and reacting oxyhydrogen mixtures (E, F, and G). I_{SC} is the short-circuit current, and V_{OC} is open-circuit voltage (electromotive force) of the device in reactive mixtures.

This observation can be a result of dissociation of H_2 molecules on Pt and subsequent spillover of H-atoms from Pt onto the TiO_2 support (Conner and Falconer 1995; Roland et al. 1997; Knotek 1980). Chemisorption of the spilt H-atoms on the mesoporous TiO_2 surface leads to accumulation of electrons in the conductance band of the semiconductor. This process enhances conductivity of the TiO_2 phase to a nearly metallic behavior and therefore removes the potential barrier at the Pt/ TiO_2 interface.

As it was mentioned earlier, the present structure supports two types of catalytic oxyhydrogen reactions referred to as the fast and slow modes. The second of these yields a long-term effect of stationary reaction current production at room-temperature conditions (see Figure 3.19 data after the time 3600 s). This effect allowed taking slow I−V scans under the condition of oxyhydrogen reaction on the sample surface. Such scans are the curves E, F, and G in the Figure 3.21 plot, representing three different concentrations of H_2 gas in its mixtures with 160 Torr O_2 gas. Interestingly, these curves take the asymmetric diode-like shape (n-type Schottky) in contrast to the I−V curves taken in vacuum (A) and pure H_2 atmosphere (B, C, and D). Each of these "oxyhydrogen reaction" curves intersects the I-axis at the nonzero point $-I_{SC}$ representing the short-circuit current parameter. It also intersects the V-axis at the point V_{OC} being the open-circuit voltage or chemical electromotive force induced in the device. As can be seen from Figure 3.21, the values $-I_{SC}$ and V_{OC} and the overall shape of the curves E−G depend on the H_2 fraction in the oxyhydrogen mixture. The diode-like shapes E−G are reversible back to the symmetric low conductance shape A in vacuum or pure O_2. This behavior contrasts with the properties of the hot electron current devices based on single-crystal supports, which preserve asymmetry in any atmosphere. Since the I−V curve in

oxyhydrogen is not a mere average of the H_2 and O_2 curves, obviously the entire Pt/TiO_2 interface is experiencing reversible qualitative changes of the energy band structure under the influence of the catalytic surface reaction. Apparently, the surface reactants convert the TiO_2 phase from an intrinsic to a higher conductance n-type semiconductor by enriching it temporarily with donor species and therefore create a Schottky-type barrier at the Pt/TiO_2 interface. Meanwhile, a dedicated effort is required for a better understanding of this property transformation. The resultant barrier height and diode ideality factor were in the ranges 0.84−0.95 eV and 1.9−3.1 units, respectively, for mixtures of 1−11 Torr H_2 with 160 Torr O_2.

All the I−V curves were taken with a Keithley 2400 sourcemeter using linear voltage sweeps in the range −0.7 to 0.7 V and reverse at the scan speed 1.17 mV/s; no significant differences were observed for the forward and reverse scans for the voltage range of Figure 3.21 data.

3.3.7 Properties of the Stationary Current

We further looked into properties of the stationary negative current (after 630 s in Figures 3.19 and 3.20) in an attempt to unveil its physical origin and understand basic mechanisms of the slow reaction process. The most important property is the following: the slow reaction occurring at a rate 1200 lower than the fast reaction yields a current of the same order of magnitude as the latter (see Figure 3.19). This property holds promise for a high yield of electrons into the external circuit

$$\eta_e = \frac{I_{sc}}{e \cdot k_{H_2}} \tag{3-2}$$

and a notable chemical-to-electrical energy conversion efficiency

$$\eta = \frac{P}{e \cdot Q \cdot k_{H_2}} = \frac{U^2}{e \cdot Q \cdot k_{H_2}} \tag{3-3}$$

Here, I_{SC} is a short-circuit current; e is electron charge; U and P are voltage and power at the external load R_L; and eQ = 2.52 eV is the energy effect of $H_2^{(g)} + 1/2O_2^{(g)} \rightarrow H_2O^{(g)}$ per H_2 molecule (Williams et al. 1992). The reaction rate estimate, k_{H_2}= 5.5 × 10^{15} s^{-1}, was obtained in the previous section, and the Figure 3.21 data give the short-circuit current, I_{SC} = 35 μA, for the curve G. This corresponds to the electron yield η_e = 0.04. The voltage and power output was found for a wide range of load resistances varied in a step-like logarithmic manner, as given in Figure 3.22 plots. These data give the energy conversion efficiency η = 0.03% for the maximal 0.63 μW power of the output signal observed at the 4.1 kOhm load. The value 4.1 kOhm is the apparent internal resistance (R_0) of the transducer device. As can be seen from Figure 3.22 data, this parameter shifts to higher values for lower partial pressures of H_2 in the oxyhydrogen mixture.

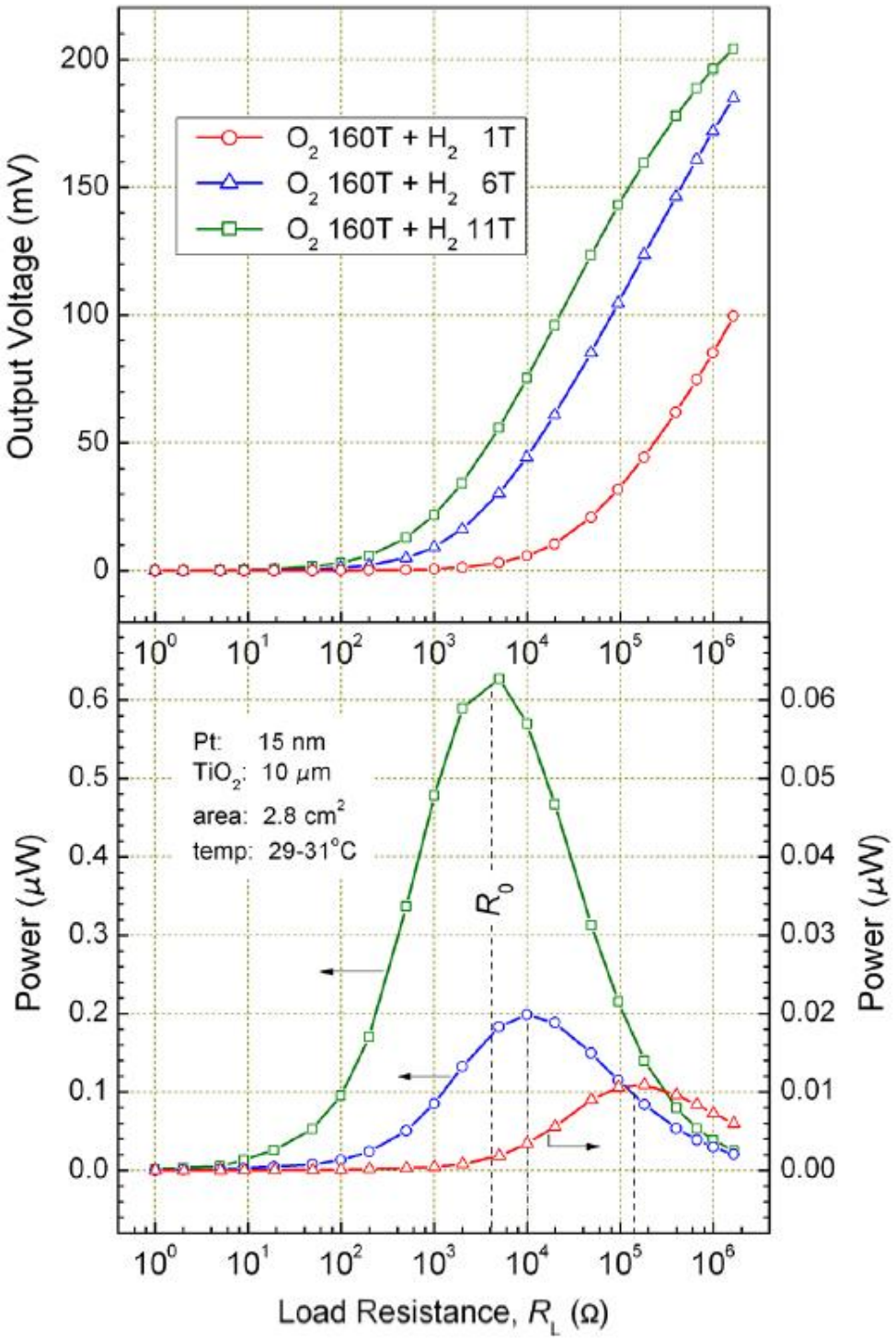

Figure 3.22. Dependence of the output signal's voltage and electrical power on load resistance. Position of the power curve maximum, R_0, represents internal resistance of the transducer, shifting to higher values at lower H_2 partial pressures.

Another property of interest for smart chemical sensor and transducer applications comes from the finding that the external load resistance R_L had no influence on the reaction rate k_{H_2}; i.e., the slow reaction is not maintained by electron flow through the external circuit, as in electrochemical batteries and fuel cells. In other words, the reaction determines the current, rather than vise versa. Also, this current cannot be related to the hydrogen concentration effect because the latter provides a positive potential on the Pt electrode by accepting protons (Schierbaum and Achhab 2011), rather than spilling them over.

3.3.8 Proton Spillover Mechanism

The high electron yield of the stationary (slow) reaction indicates that the electromotive force is produced in a surface-driven process of Langmuir−Hinshelwood or Harris−Kasemo (Nienhaus 2002) type involving transfer of the negative charge from TiO_2 and toward the Pt phase on the surface. The nanodispersed Pt phase can support various hydrogen species that may further migrate from Pt to TiO_2 via the well-known hydrogen spillover process (Knotek 1980; Conner and Falconer 1995). The split species can be protons, as was reported for various Pt/ metal oxide systems (Levy 1974; Roland 1997). Therefore, we suggest that the electromotive force of the slow mode current is a result of proton spillover from Pt to TiO_2 (see Figure 3.23).

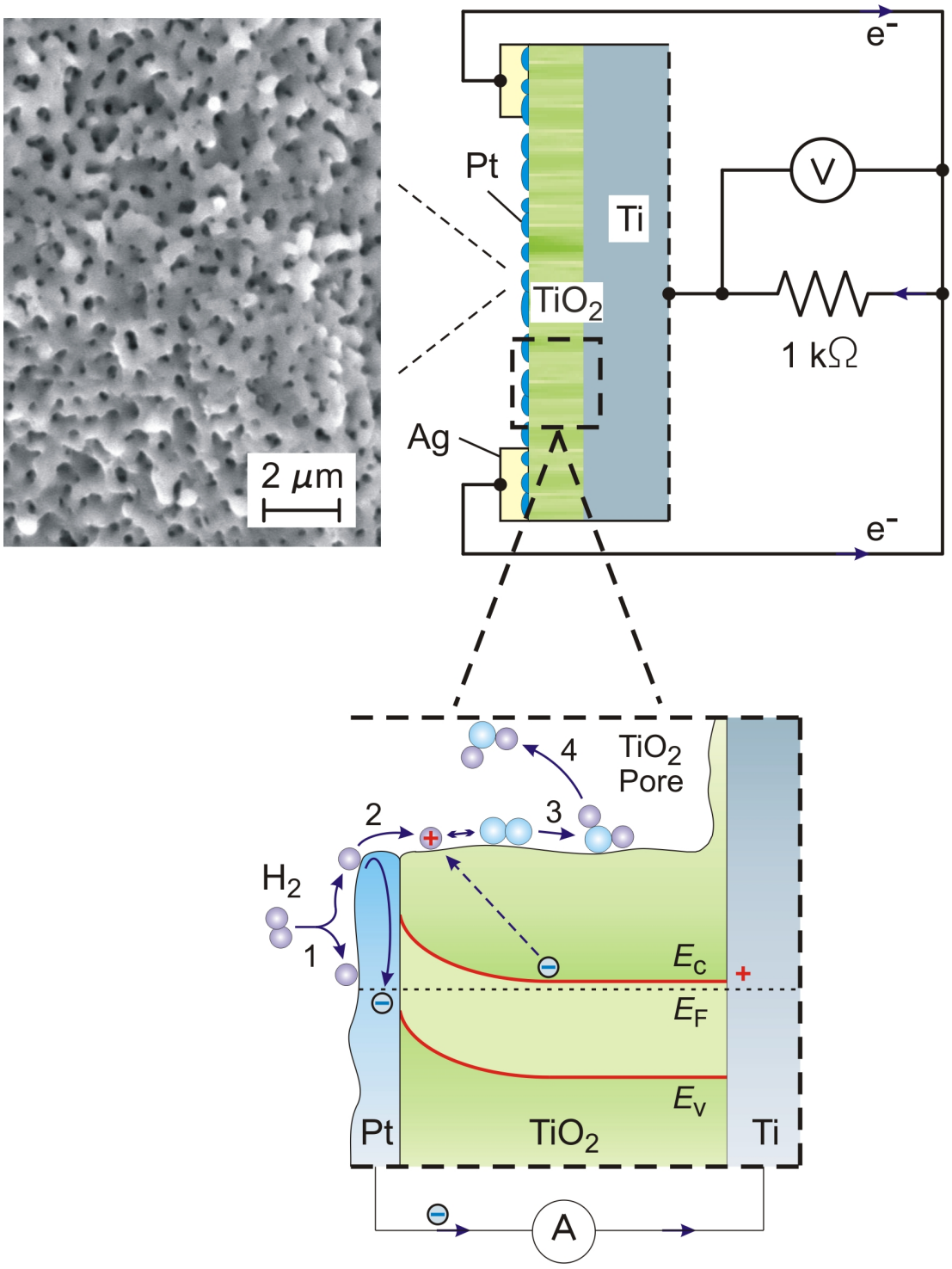

Figure 3.23. Proton spillover mechanism of chemi-EMF in Pt/TiO_2

Here, the high electronegativity of Pt could be the cause of ionization of energetic hydrogen precursors hopping (Barth et al. 1997; Wintterlin et al. 1997) on the surface across the Pt−TiO_2 boundary

$$2H^{(Pt)} \rightarrow 2H^{+(Pt)} + 2e^- \quad (3\text{-}4a)$$

$$2H^{+(Pt)} \rightarrow 2H^{+(TiO_2)} \ (\text{Spillover}) \quad (3\text{-}4b)$$

Next, the protons chemisorbed at the TiO_2 surface can participate in a typical cathode reaction

$$2H^+ + \frac{1}{2}O_2 + 2e^- \rightarrow H_2O \quad (3\text{-}5)$$

Here, electrons arrive to the TiO_2 conductance band from the Pt electrode via an external electrical circuit. This process is finalized by water desorption from the TiO_2 surface, which is possibly the key limiting step of the overall H_2 + 1/2O_2 → H_2O slow mode reaction. Thus, the Pt and TiO_2 phases of the composite catalyst serve as the anode and cathode of the electrical generator, separated only by a Schottky-type potential barrier for electrons and where the proton spillover creates the electromotive force.

It is worth recalling that oxidation of hydrogen on the Pt surface from the gas phase releases 76% of its energy as the heat of H_2 and O_2 dissociative adsorption (Williams 1992). The reaction mechanism of eqs 3-4 and 3-5 needs to utilize a significant portion of this energy to ionize the spilling hydrogen atoms. The independence of the

reaction rate on the load resistance R_L mentioned in the previous section is also compatible with such a reaction mechanism. Here, the spilling protons could be replaced with neutral H-atoms at higher R_L due to a buildup of charge in the structure, without affecting notably the overall reaction flow. In spite of the overall compliance of the data with the proton spillover mechanism, the latter should be viewed as one possibility only; further supportive evidence and other legitimate scenarios should be sought after.

Among the two distinct regimes of H_2 oxidation on Pt/TiO_2(por), only the slow mode can be relevant to the proton spillover process. Indeed, electron yield of the fast reaction is not higher than 5×10^{-5}, and therefore it is likely to occur on the Pt phase alone. On the contrary, the slow mode should involve reaction steps on both Pt and TiO_2 surfaces, as in eqs 3-4 and 3-5, to support the efficient charge transfer between the two phases elucidated from the reaction current kinetics. Conclusions of this kind would be difficult to substantiate with the use of standard methods of surface analysis, and they illustrate research potential of the chemical-electrical signal transduction studies. Reaction current based analysis of surface processes can be particularly useful at high pressure conditions typical for industrial catalysis, where application of the standard (vacuum-based) techniques, such as LEED, electron energy loss, Auger ion-scattering spectroscopy, and others, is complicated. Finally, the irregular mesoporous Pt/TiO_2 system discussed here is a closer model of actual industrial catalysts than the single-crystal-type Schottky structures.

3.4 Conclusions

In this study, an electrically continuous Pt mesh or grating layer of 15 nm thickness was deposited on top of a mesoporous TiO_2 layer grown on a solid Ti substrate by the plasma electrolytic oxidation method. Voltage-current characteristic of the resultant Pt/TiO_2/Ti micro-nanostructure was symmetric low conductance in vacuum or pure O_2, symmetric high conductance in pure H_2, and asymmetric diode-like in oxyhydrogen mixtures. The Pt/TiO_2/Ti structure supported a continuous oxidation of hydrogen to water, starting at room temperature in 160 Torr O_2, and it also worked as a chemical− electrical transducer. The reaction current signal recorded between the Pt and Ti terminals clearly showed the presence of a secondary, 1200 times slower mode of the reaction in addition to the usual (fast) oxidation of hydrogen over the nanodispersed Pt. Gas admission procedures to achieve the slow mode are described. The slow reaction leads to surprisingly high currents in the forward bias direction of the diode, disproportional to the reaction rate, when the latter is compared to the rate of the fast reaction. This phenomenon is explained by involvement of both Pt and TiO_2 surfaces in the slow reaction process accompanied by efficient charge transfer between the two phases. A proton spillover mechanism is proposed as a possible source of the observed electromotive force. In any case, basic properties of the slow mode current are incompatible with the known thermal and hot electron mechanisms of the reaction-driven currents. This stationary current is characterized with 0.04 electron yield, −0.32 V electromotive force (open circuit voltage), and 12 μA/cm^2 short-circuit current density, which is >100 times higher than the typical hot electron current density at room temperature. The electrical signal of such a magnitude can be reliably used for various

analytical purposes, including reaction paths and rate studies, in situ catalyst thermometry, and electrometry. Furthermore, the overall reaction current kinetics contains many autonomously formed features in the form of peaks and alterations of the charge flow direction to manifest transitions between various surface reaction regimes. This provides interesting possibilities for analysis and applications to smart chemical sensors enabling automatic release of regulatory chemicals. The observed chemical−electrical energy conversion efficiency of up to 0.03% on impedance-matched loads might also inspire novel micro-power applications.

CHAPTER 4

EFFECT OF TEMPERATURE ON THE PROPERTIES OF THE REACTION CURRENT INDUCED IN THE MESOPOROUS Pt/TiO_2

(Figures 4.1, 4.2, 4.3, 4.4, 4.6 and the related discussion were previously published as Hashemian, M.A., Palacios, E., Nedrygailov, I.I., Diesing, D., and Karpov, E.G. "Thermal Properties of the Stationary Current in Mesoporous Pt/TiO_2 Structures in an Oxyhydrogen Atmosphere". *Appl. Mater. Interfaces*, 2013, 5, 12375−12379)

4.1 Introduction

Investigation of the mechanisms of generation and transport of the electrical charge in nanomaterial-based catalysts (for example, nanodispersed Pt supported on a porous TiO_2 substrate) is a key to mastering heterogeneous catalysis, control of the surface chemical reactions flow, artificial photosynthesis, and the design of advanced chemical sensors and transducers. Tuning the activity and selectivity of the catalysts through charge transfer by electrons, holes, or ions induced by external means (such as light or electric field) is a well-known and intensively studied phenomenon (Zhang and Yates 2012; Gross and Somorjai 2013; Kim et al. 2013).

Recent studies of the exothermic chemical reactions at the surface of nanofilm multilayer structures clearly showed that the generation and transport of the electrical charge can also occur independently of the external physical stimuli (Schierbaum and Achhab 2011; Karpov et al. 2013; Schindler et al. 2013). For example, the current of chemically induced energetic electrons and holes (with >0.5 eV of excess energy), known as chemicurrent, in Ag/Si and Cu/Si nanostructures during adsorption of atomic gas

species was reported (Gergen et al. 2001; Nienhaus et al. 2002). Further experiments with different gases and various thicknesses of the top electrode have shown that the magnitude of the chemicurrent is proportional to the gas flux as well as the number of empty sites on the surface, available for gas adsorption. The lifetime of chemically induced energetic electrons was shown to be on the order of tens of femtoseconds. These observations point out on an essentially nonequilibrium character of the chemicurrent generation, which, in turn, unveils an opportunity for ultrafast chemical to electrical signal transducers. Steady-state currents induced by catalytic oxidation of CO and H_2 species on TiO_2, SiC, and GaN Schottky structures with a continuous Pd, Pt, or Au top film were also reported (Park et al. 2007; Karpov and Nedrygailov 2009). Metal-insulator-metal structures based on metal oxide layers with thicknesses of only a few nanometers have also been used in this context (Mildner et al. 2006; Schindler, et al. 2013).

Recently, a different type of structure for detection of the electric current induced by a surface chemical reaction was reported (Karpov et al. 2013). As mentioned in chapter 3, these structures are based on mesoporous TiO_2 films grown on a Ti substrate, where an electrically continuous array of Pt nanoparticles is deposited on the TiO_2 surface. It was shown that the mesoporous Pt/TiO_2 structures allow detection of the unusually strong stationary current at room temperature when the chemical reaction rate is very slow. The origin of this current is not fully understood. Such a current induced in the mesoporous Pt/TiO_2 structure by surface chemical reactions is called the reaction current. As shown in chapter 3, the quantum yield, the number of charge carriers detected per one H_2 molecule oxidized at the detector surface, for the mesoporous Pt/TiO_2

structures may reach 0.04 at room temperature, which is much higher than the values reported previously for the chemicurrents (Nienhaus et al. 1999; Hervier et al. 2009; Karpov et al. 2013). In addition to the reaction current, a significant electromotive force (open circuit voltage) of about −0.32 V was also detected during the surface chemical reaction. Large reaction currents of the reverse direction in a system with a Pt paste contact applied to the TiO_2 surface were also reported (Schierbaum and Achhab 2011). In order to explain such a strong effect in the mesoporous Pt/TiO_2 structure, several mechanisms have been proposed for the underlying electromotive force (chemi-EMF). In previous chapter we considered processes of proton formation at the Pt surface and their spillover into the mesoporous TiO_2 phase, where they can react with the adsorbed oxygen species to form water. The following surface reaction mechanism was suggested:

anode (Pt): $$2H^{(Pt)} \rightarrow 2H^{+(Pt)} + 2e^{-} \quad (4\text{-}1)$$

spillover: $$2H^{+(Pt)} \rightarrow 2H^{+(TiO_2)} \quad (4\text{-}2)$$

cathode (TiO_2) $$2H^{+} + \frac{1}{2}O_2 + 2e^{-} \rightarrow H_2O \quad (4\text{-}3)$$

Here, electrons arrive at the TiO_2 conductance band from the Pt electrode via an external electrical circuit. The observed chemi-EMF was also attributed to electrochemical processes similar to those observed in galvanostatic solid electrolyte hydrogen sensors (Schierbaum and Achhab 2011). However, the amount of experimental data available presently is insufficient either to confirm or to refute these hypotheses. This chapter unveils an effect of temperature on the properties of the reaction current induced in the mesoporous Pt/TiO_2 structure by oxyhydrogen reaction on its surface. We report on a

complex multiregime dependence of the reaction current magnitude on the sample surface temperature, suggesting an interplay of several distinct mechanisms involved in the process of the current generation. The effects discussed in this chapter can be instrumental in understanding the physical origin of the reaction current and the associated chemi-EMF.

4.2 Experimental Procedure

A mesoporous Pt/TiO_2 sample was fabricated in a two-step procedure, identical with the one described in section 3.2.1. First, a 10-μm-thick oxide layer was obtained on a 0.989 pure Ti metal substrate of 36 × 12 × 0.5 mm^3 dimensions using plasma electrolytic oxidation (Sul et al. 2002; Diamanti and Pedeferri 2007; Park 2008) in the 3 M sulfuric acid electrolyte. During the anodization process, the cell voltage gradually increased upon reaching 155 V, while the current was maintained constant at 0.85 A. We note that fabrication of mesoporous titania using plasma electrolytic oxidation is an established technique. The resultant porous structure is usually explained by a rapid motion of micro discharges along the Ti anode surface during the oxidation process (Park 2008).

Next, a 15 nm equivalent Pt layer was deposited through a 34 × 10 mm^2 mask on one side of the anodized sample at a rate 0.02 nm/s in a 10^{-6} Torr vacuum. Subsequent field-emission scanning electron microscopy (FESEM) scans of the Pt-coated TiO_2 surface did not reveal any changes in the surface structure, implying that Pt metal was deposited as a nanometer thickness blanket layer with multiple openings (holes) at the positions of the TiO_2 surface pores. We will refer to such a Pt nanophase as a

"nanomesh" hereafter. The sample was then annealed at 400 K for 10-20 min, leading to a stable nanomesh resistance of 340−350 Ω measured under ambient conditions between the two Ag conductive paste terminals applied to the opposite ends of the Pt nanomesh. The sample was mounted inside a 4.5 L vacuum/environmental chamber with a base pressure of $<10^{-7}$ Torr. A small resistive temperature sensor (Omega F2020-100) was placed in the middle of the Pt-coated area of the sample. Finally, two parallel-connected halogen bulbs were mounted at a distance of 18 mm to the Pt-coated side of the sample to perform as a radiative heater (Figure 4.1). The heater was operated at a power of less than 1.6 W per one bulb, and therefore the radiant temperatures were low enough to generate no detectable photocurrent in all experiments reported in this chapter.

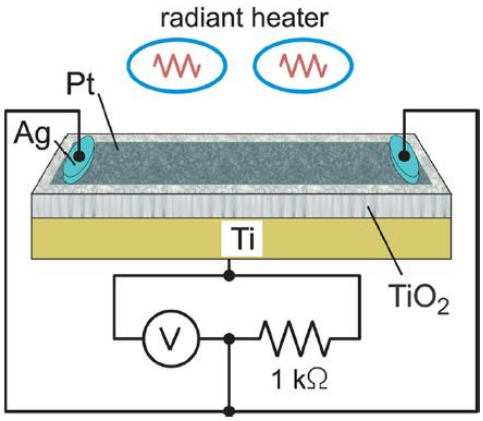

Figure 4.1. Overall sample structure, reaction current measurement circuit, and heating setup

4.3 Results and Discussion

As it was discussed in chapter 3, a procedure was developed that allows us a well-reproducible detection of the reaction current in the mesoporous Pt/TiO_2 structures at room temperature. First, we initiate the ignition of hydrogen on the Pt/TiO_2 surface by adding 16 Torr H_2 to an isolated chamber with the sample assembly in a 160 Torr pure O_2 atmosphere. As can be seen from Figure 4.2 data, this leads to sharp reaction current and temperature peaks, which are discussed in greater detail in pervious chapter. We will call this process an "activation" hereafter. Presently, it is not clear what exactly happens with the surface of a mesoporous Pt/TiO_2 structure during the activation. However, we can assume that, during the activation process, the fast catalytic reaction between hydrogen and oxygen can clean the Pt/TiO_2 surface from the adsorbed residual gas particles. A similar effect led to a significant increase of the catalytic activity of the Pt wire after ignition of the hydrogen and oxygen mixture occurred on its surface (Keck et al. 1983). Upon completion of the transient processes by the time 900 s (Figure 4.2), a small amount of H_2 about 1 Torr still remains in the chamber, the surface temperature returns to a room temperature value, and the reaction current acquires a stationary value of about 0.4 μA. This current is associated with a very slow hydrogen consumption rate, not higher than 5×10^{15} H_2 molecules per second. Interestingly, the further addition of H_2 gas to the chamber only increases the magnitude of the stationary reaction current, while the surface temperature remains unchanged. For example, admission of 5 Torr H_2 to the chamber at the time 1860 s increases the reaction current value from 0.4 to 5−9 μA during the next 2.5 h (see Figure 4.2). The initial resistance of the Pt nanomesh (340-350

Ω) did not change significantly in the end of such an experiment, proving the long-term stability of this Pt phase.

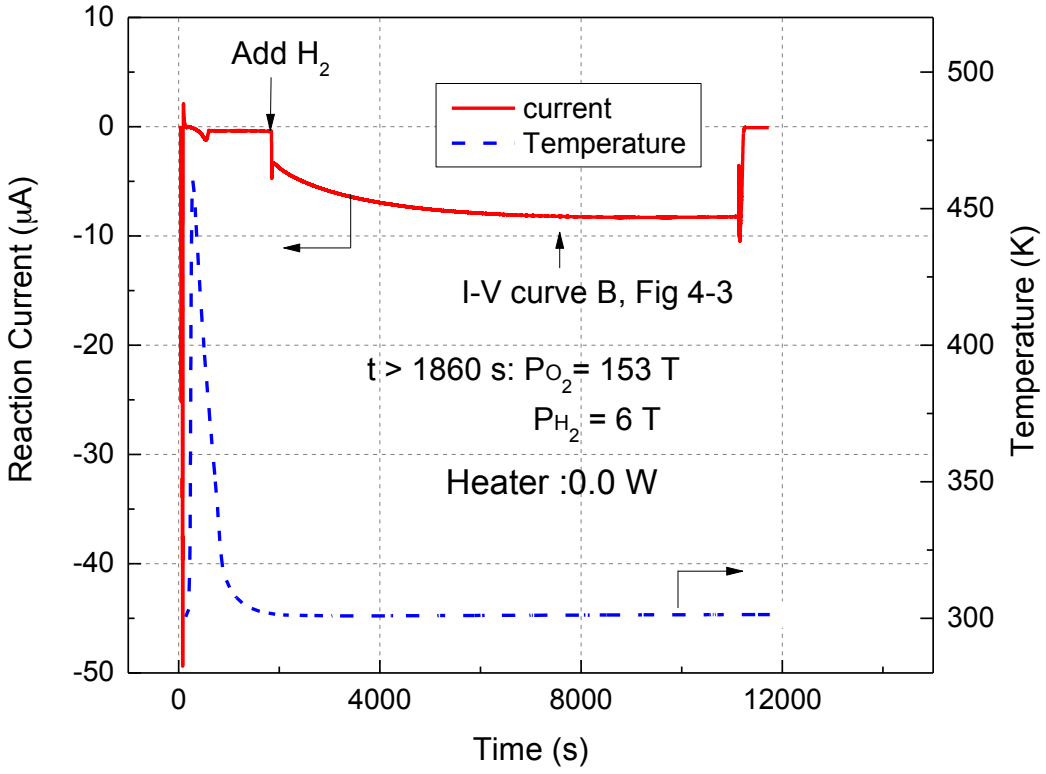

Figure 4.2. Long-term kinetics of the reaction current and the corresponding surface temperature reading with no external heating during the entire experiment

Figure 4.3 shows the I−V curves taken between the Ti and one of the Pt terminals, with a Keithley 2400 sourcemeter at room temperature conditions. Linear voltage sweeps programmed from −0.7 to 0.7 V and in the reverse direction at the rate 70 mV/min were used. Such a slow rate was selected to avoid capacitive charging currents in the catalytic structure. The I−V curves measured during the slow surface reaction of hydrogen and oxygen starting at the time 8000 s (see Figure 4.2a) differ significantly from that

measured in vacuum. As seen in Figure 4.3, such I−V curves have an asymmetric diode-like shape and intersect the I axis at the short-circuit reaction current value, I_{SC}. They also intersect the V axis at the point V_{OC}, representing the open-circuit voltage or chemical electromotive force of this structure. The values I_{SC} and V_{OC} and the overall shape of the I−V curves depend on a specific composition of the oxyhydrogen mixture.

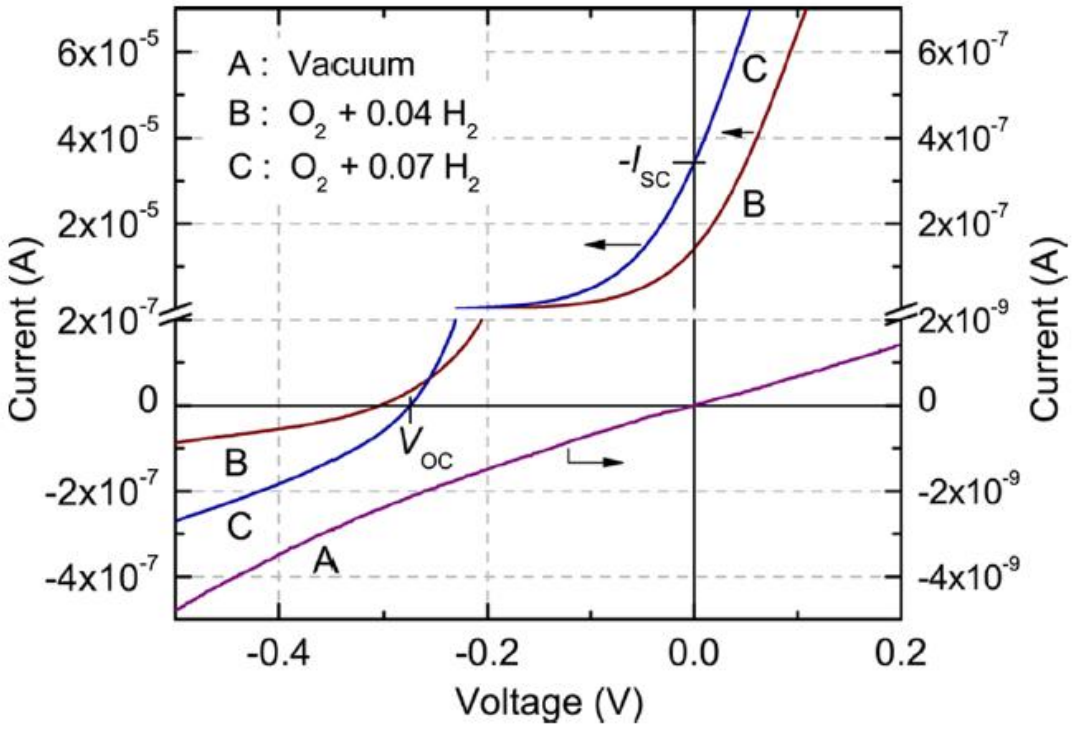

Figure 4.3. I−V curves of the mesoporous Pt/TiO_2/Ti structure measured between the Ti substrate and Pt layer (positive bias at Pt) in a vacuum (curve A), 1:0.04 oxyhydrogen mixture (curve B), and 1:0.07 oxyhydrogen mixture (curve C). The O_2 base pressure is 153 Torr in both mixtures. V_{OC} and I_{SC} are clearly defined

In order to study the effect of temperature on the stationary reaction current, the halogen bulb heater assembly was turned on at the time 3600 s, and a constant heater power was maintained during the time interval 3600−10800 s (Figure 4.4a-c).

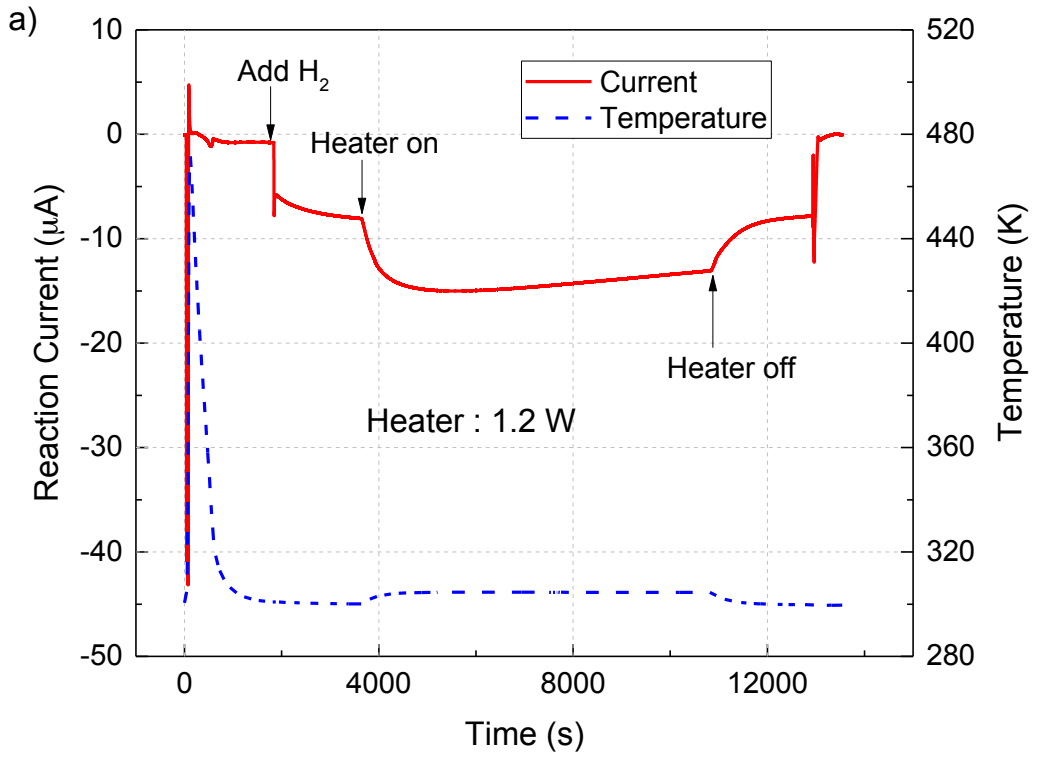

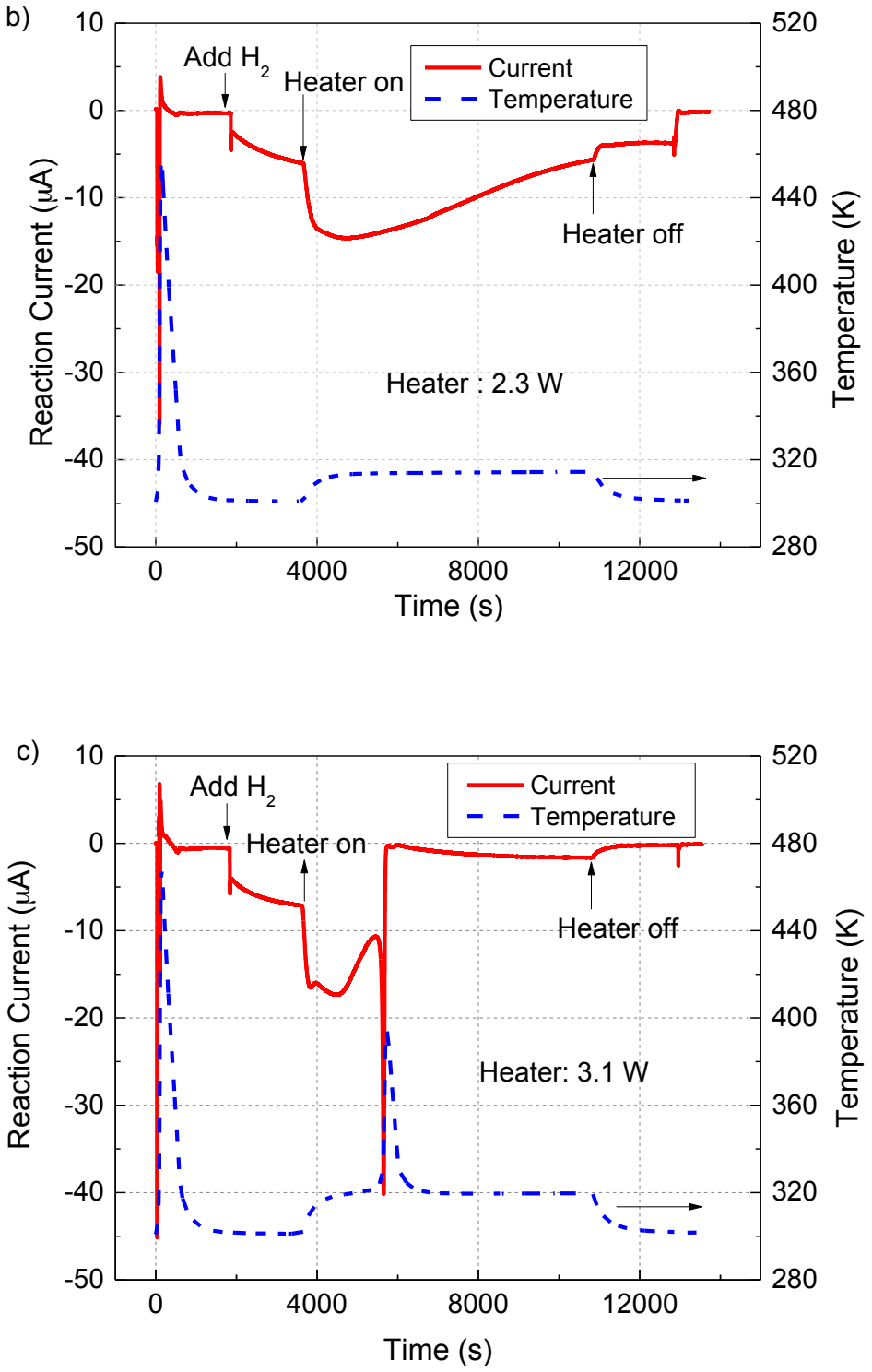

Figure 4.4. Long-term kinetics of the reaction current (in 153 Torr O_2 + 6 Torr H_2) and the corresponding surface temperature reading (a) 1.2 W, (b) 2.3 W, and (c) 3.1 W during the time interval 3600−10800 s

In additional experiments, which were made in vacuum and pure oxygen, it was found that such a method of heating does not lead to generation of a measurable photocurrent. As can be seen in Figure 4.4a and 4.4b, heating of the sample in the O_2 + 0.04 H_2 gas mixture with a low power leads only to a smooth increase of the reaction current. The current then reaches a new stationary or slowly changing value. However, when the sample is heated with a higher power (Figure 4.4c data), the reaction current passes through the several maxima at temperatures 314 and 321 K and then starts to decrease. Further heating initiates the ignition of hydrogen on the Pt/TiO_2 surface at a temperature of about 325 K, similar to the activation process described above. Figure 4.5 shows the effect of temperature on the reaction current during the second addition of hydrogen (153 Torr O_2+ 11 Torr H_2). Figure 4.5a shows the long term kinetics of the reaction current with no external heating. After the second addition of H_2, the heater was turned on and a constant power was maintained for 2 hours (Figure 4.5b-d). It can be seen that a lower power is needed to initiate the ignition of hydrogen in the O_2 + 0.07H_2 gas mixture compared to O_2 + 0.04H_2 (see Figure 4.4c and 4.5d). This can be explained as a result of larger hydrogen fraction in the mixture.

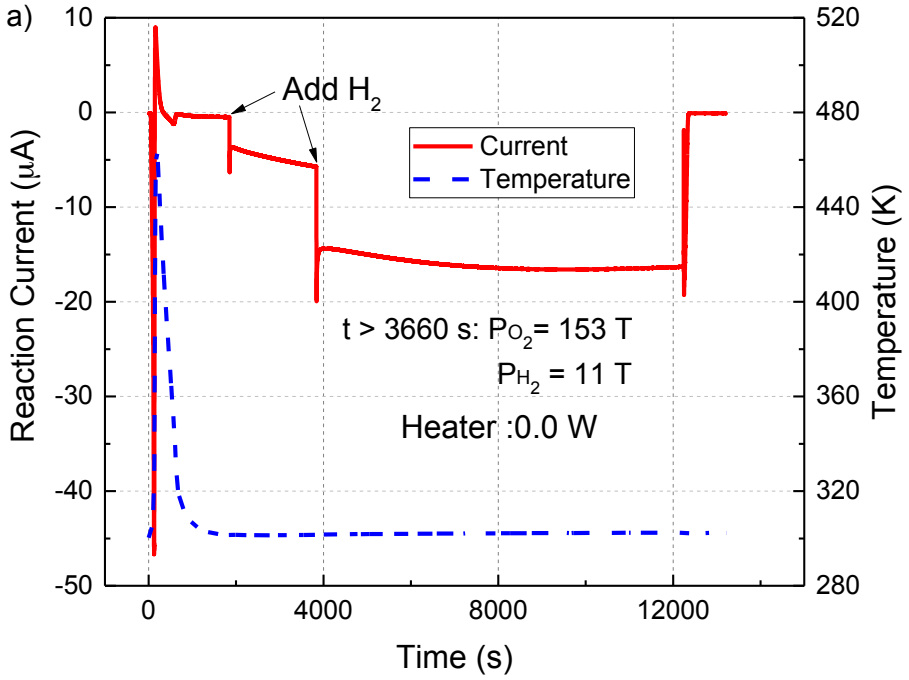
a)
Add H_2
Current
Temperature
t > 3660 s: P_{O_2}= 153 T
P_{H_2} = 11 T
Heater :0.0 W
Reaction Current (μA)
Temperature (K)
Time (s)
10
0
-10
-20
-30
-40
-50
520
480
440
400
360
320
280
0
4000
8000
12000

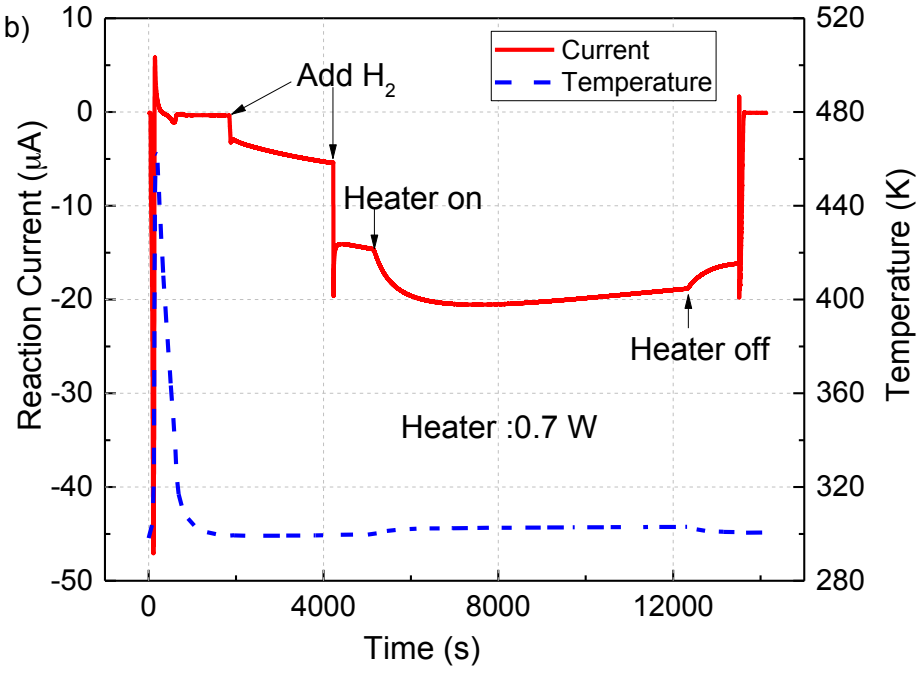
b)
Add H_2
Current
Temperature
Heater on
Heater off
Heater :0.7 W
Reaction Current (μA)
Temperature (K)
Time (s)
10
0
-10
-20
-30
-40
-50
520
480
440
400
360
320
280
0
4000
8000
12000

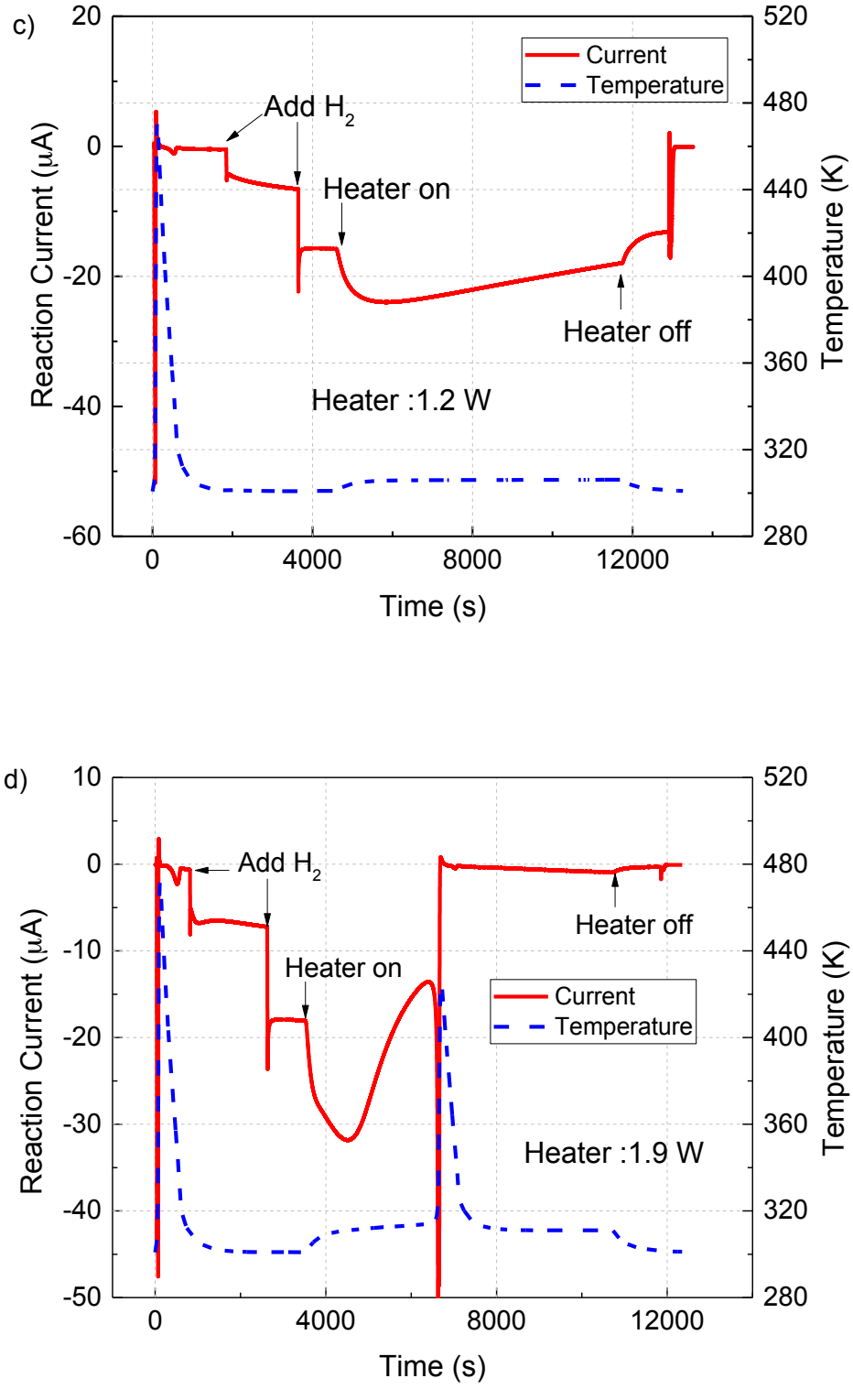

Figure 4.5. Long-term kinetics of the reaction current (in 153 Torr O_2 + 11 Torr H_2) and the corresponding surface temperature reading (a) 0.0, (b) 0.7, (c) 1.2, and (d) 1.9 W

The whole temperature dependence of the reaction current recorded in the O_2 + 0.04 H_2 gas mixture for the temperature of the mesoporous Pt/TiO_2 structure in the range of 300−325 K is shown in Figure 4.6. The same figure also gives data for the O_2 + 0.07 H_2 gas mixture consisting of 11 Torr H_2 in 153 Torr O_2. As can be seen, in both cases the temperature dependence of the reaction current has a "W" shape with the two maxima. However, for the gas mixture with a larger hydrogen fraction, the entire temperature dependence of the reaction current shifts to higher values, while the current maxima correspond to lower temperatures.

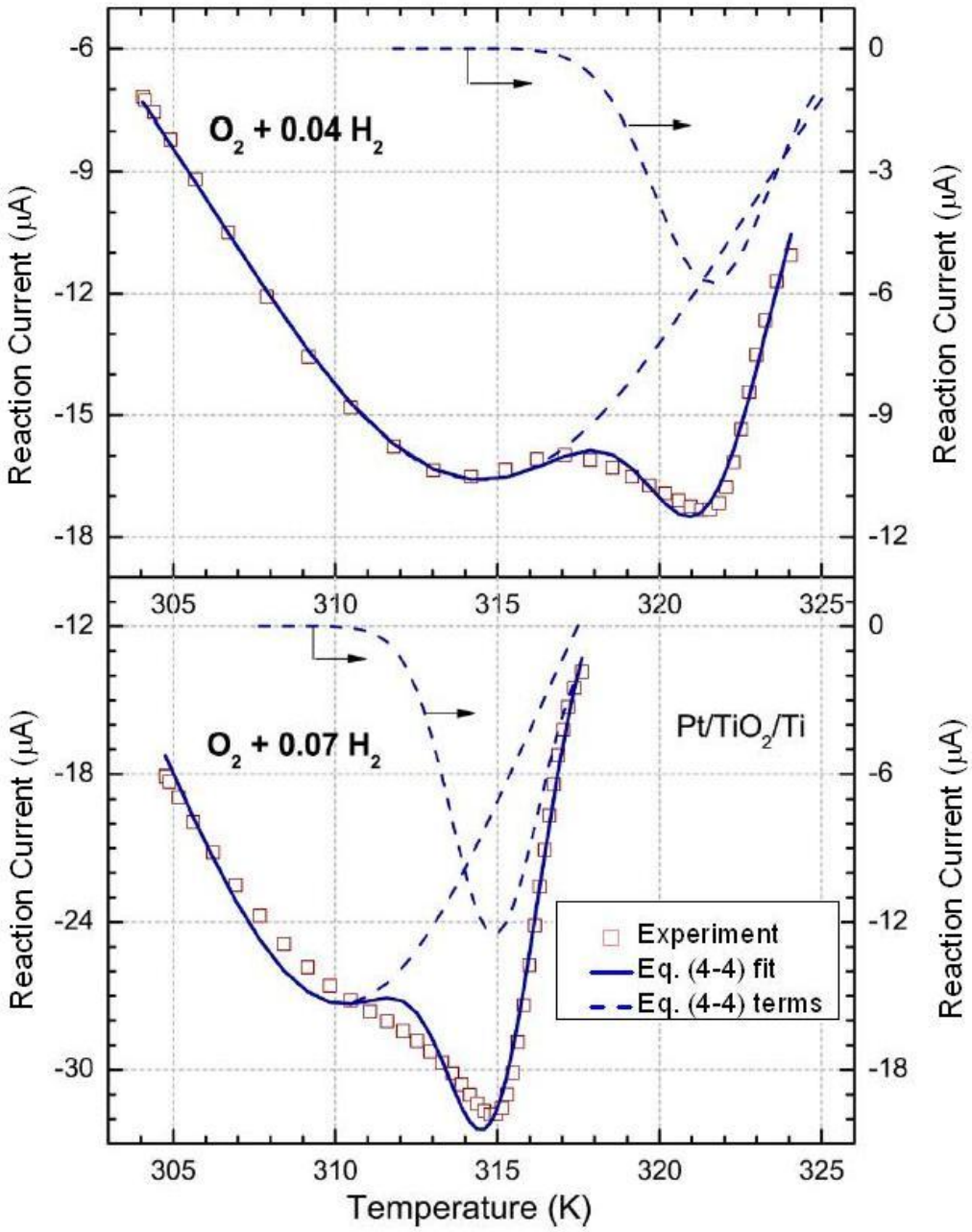

Figure 4.6. Temperature dependence of the stationary reaction current for the O_2 + $0.04H_2$ and O_2 + $0.07H_2$ mixtures at the base pressure of oxygen P_{O2} = 153 Torr: experimental data, eq 4-4 analytical fit, and the constituent Gaussian peaks

In order to determine the exact position of the maxima, the curves of the reaction current as a function of the temperature, shown in Figure 4.6, have been decomposed using multiple Gaussian functions:

$$I = \sum_{i=1}^{2} A_i \exp\left[-\frac{1}{2}\left(\frac{T - T_{max}^{(i)}}{\sigma_i}\right)^2\right] \quad (4\text{-}4)$$

The resulting fitting curves, as well as individual Gaussian components, are also shown in Figure 4.6 using thin black solid and dashed lines, respectively. Table IX gives the parameters obtained for the Gaussian components, where T_{max} is the Kelvin temperature at the peak maximum, σ_i is the width of the peak at half-height and A_i is the peak amplitude. As can be seen, Gaussian decomposition of the reaction current as a function of temperature yields two components with the parameters dependent on the hydrogen concentration.

Table IX. Decomposition parameters of the temperature dependence of an induced reaction current using multiple Gaussian functions

	$O_2 + 0.04H_2$		$O_2 + 0.07H_2$	
	peak 1	peak 2	peak 1	peak 2
A (μA)	-16.6	-5.74	-27.3	-12.5
T_{max} (K)	314.5	321.6	310.2	314.9
σ (K)	8.16	1.77	5.68	1.34

Such a complex temperature dependence of the reaction current in the mesoporous Pt/TiO_2 structure can be explained as a result of the competition of several chemical and electrical processes. On the one hand, the reaction current depends on the rate of charge carrier generation in the course of a surface chemical reaction. Therefore, the temperature rise should lead to an increase in the chemical reaction rate and, consequently, stronger current. It should also be noted that the maximum of the reaction current as a function of the temperature, reported in this article, is in the same temperature range as the peak of molecular water desorption from the TiO_2 surface, which was found to be in the range of 300-350 K for disordered (powder) TiO_2 surfaces (Henderson 1994). This process, in principle, could also increase the current because it leads to the cleaning of the surface from the reaction products. It could explain the first (wider) peak in the reaction temperature dependence (Figure 4.6), while the second peak is possibly related to the spillover process or cathode reaction activation. On the other hand, the reaction current value also depends on the properties of the charge carriers, such as lifetime and mobility, as well as the electrical properties of the Pt/TiO_2 interface. These parameters also depend on the temperature because of electron-phonon scattering processes and, as a rule, lead to a decrease in the efficiency of detection of the excited charge carriers in the diode-like structures at elevated temperatures. All of these competing factors could play a role in both Gaussian components of the reaction current.

It is interesting to note that both Gaussian components have similar behavior when the hydrogen concentration is varied: they narrow and shift toward lower temperatures with a higher amount of hydrogen in the gas mixture. Also, the last point on each of the two experimental curves of Figure 4.6 corresponds to a heater power already

sufficient to reinvoke the fast reaction process, i.e., such a mode switching occurs easier for a hydrogen-richer environment: at 315 K for the O_2 + 0.07 H_2 oxyhydrogen versus 321 K for the O_2 + 0.04 H_2 mixture. This behavior gives a hint that the system can be in a dynamic metastable state during the room temperature reaction. According to transition state theory (Wigner 1937; Vineyard 1957; Voter and Doll 1985), a greater collision frequency factor related to the higher H_2 gas pressure can lead to relaxation of the metastability at a lower temperature.

4.4 Conclusions

We conclude that the entire temperature dependence of the slow reaction current induced by an oxyhydrogen reaction on the mesoporous Pt/TiO_2 system has a "W" shape with two peaks. This behavior cannot be interpreted on the basis of a single mechanism of the chemi-EMF, such as hot electron transport, proton spillover, or thermoelectricity (Schierbaum and Achhab 2011; Karpov 2013). Two or more distinct processes contribute to this chemi-EMF, although further studies are required for their more detailed understanding. More generally, this reaction current represents an interplay of several chemical and electrical processes. Most notably this is evidenced (1) by the metastability of the room temperature process, which may switch to the fast mode by raising the surface temperature to only 10-20 K depending on the hydrogen fraction in the gas phase and (2) by the matching of the reaction current peak 1, Table IX, and the water desorption peak for the titania surface (Henderson 1994).

CHAPTER 5

EFFICIENT HYDROGEN SENSING PERFORMANCE OF THE MESOPOROUS Pt/TiO_2 SYSTEM AT ROOM TEMPERATURE

(Previously published as Hashemian, M.A., Karpov, E.G. "Hydrogen Sensing Behavior of Pt-coated Mesoporous Anodic Titania". *Materials Chemistry and Physics*, 2014, 148, 579−584)

5.1 Introduction

Due to volatility and flammability of hydrogen gas, a small leakage of hydrogen-containing gases could lead to disastrous consequences. In the recent years, many groups have reported hydrogen sensors with different mechanisms and structures (Maffei and Kuriakose 2004; Zalvidea et al. 2006; Nedrygailov and Karpov 2010; Hübert et al. 2011; Indacochea et al. 2008). The electrical and optical changes of thin palladium layer (40 nm) have been reported during the hydrogen adsorption (Fedtke et al. 2004). This sensor showed a good behavior up to 4% hydrogen in nitrogen. Many groups have reported that metal-semiconductor (MS) Schottky diodes work well as hydrogen sensors (Song et al. 2005; Huang et al. 2007; Zdansky and Yatskiv 2012). Platinum or palladium Schottky diodes based on *n*-type GaN semiconductor revealed significant changes in the electrical characteristic of the sensor upon exposure of hydrogen in Ar or air mixture at room (Yam and Hassan 2007) and elevated temperature (Luther et al. 1999). Metal–insulator–semiconductor (MIS) Schottky diodes, $Pt/SiO_2/GaN$, has been studied over a wide range of temperatures in the normal air atmosphere which demonstrated high sensitivity and a fast response time (Tsai 2008).

TiO_2 nanotubes and nanoporous structures have also been studied as hydrogen sensors, showing reversible responses in both air and N_2 atmospheres (Varghese et al. 2003; A. A. Haidry et al. 2012; Moon et al. 2012; Rahbarpour and Hosseini-Golgoo 2013). It has been shown that the hydrogen sensing performance of anodically oxidized TiO_2 sensors can be affected by several parameters such as film morphology, oxidation temperature, and electrode materials (Shimizu et al. 2007) . The influence of nanotube diameters on the resistance variation of the TiO_2 has been tested and a three order of magnitude resistance variation was observed with exposure of 100 ppm hydrogen to N_2 ambient (Şennik et al. 2010). For higher concentration of hydrogen (500 ppm), a four order of magnitude change has been reported. In the previous work, the sensitivity of TiO_2 sensor has been studied at various operating temperatures, ranging from 250ºC to 450 ºC (Haidry et al. 2011).

In this chapter, we discuss hydrogen sensing properties and mechanisms of a Pt/TiO_2 type device based on anodically grown mesoporous titania. The device is simple to fabricate and it demonstrates extreme changes in its electrical resistance due to hydrogen exposure at *room temperature*. Here, the Pt catalyst was finely dispersed as an electrically continuous nanometer thickness mesh supported by the TiO_2 layer, and the anodized Ti metal substrate served as a base support and back contact. Dependence of response characteristics on the source voltage is discussed. In order to understand basic mechanisms of the observed sensing performance, the experiments have been carried out in vacuum, oxygen and nitrogen gases at 160 Torr, and at bias reversal conditions. Hydrogen sensing behavior of this system is demonstrated, showing remarkable responses down to 0.003 Torr of H_2 partial pressure (20 ppm).

5.2 Experimental Procedure

The procedure of sample fabrication can be found in chapters 3 and 4. Prior to the hydrogen sensing measurements, the sample surface was activated by oxyhydrogen reactions. The activation procedure has been described in chapter 3. Upon completion of the activation process, a repeatable baseline for resistance reading was obtained by exposing the sample to 160 Torr atmosphere of pure O_2 during 65 h, while a constant source voltage was kept applied to the sample. The resistance data recording started after 41 h of the exposure. Such a long pre-exposure with the source voltage in the background atmosphere was employed to eliminate a slow memristor effect (Wu and McCreery 2009; Miller et al. 2010)**,** due to oxygen vacancy diffusion in the TiO_2 layer, which the system showed in hydrogen-free atmospheres. In the beginning of each cycle of the hydrogen sensing studies, a particular amount of H_2 gas was admitted to the chamber and retained in it during 6 h resulting in a sharp decrease of the sample resistance. During the next 30 min, the chamber was evacuated to a 10^{-6} Torr vacuum, followed by admission of 160 Torr oxygen retained in the chamber for 16 h to recover resistance of the sensor. All the measurements were performed at room temperature (26-28˚C). Sensor resistance was recorded continuously at a rate of 5 readings per minute with a Keithley 2400 sourcemeter in the voltage source mode.

In order to understand the effect of recovery gas on the sensor performance, oxygen gas was also replaced by nitrogen, which will be discussed below. The sensor tests were conducted at different hydrogen pressures and applied voltages in the range of 0.003−3 Torr and 0.5−2.0 V, respectively.

5.3 Results and Discussion

5.3.1 Sensitivity and Response Properties

The variation of the Pt/TiO_2/Ti structure resistance with time in different concentration of hydrogen in the presence of oxygen at room temperature were studied by applying different voltages at the Pt layer relative to the Ti substrate terminal (Figure 5.1).

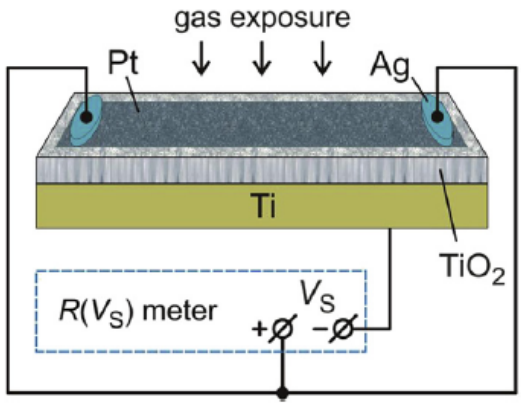

Figure 5.1. Sample wiring and the setup for resistance (R) measurements; V_S is a fixed source voltage

Response of the sensor to different partial pressures of H_2 gas under 0.5 V is shown in Figure 5.2(a). Upon admission of 3 Torr of hydrogen, the initial resistance of 4.5×10^8 Ohm jumped abruptly down within less than one minute, and then went more gradually down to the final value 7.5×10^5 Ohm within 6 hours. By removing H_2 from the chamber during the next 30 min and adding pure O_2 gas at 160 Torr, the sensor resistance rapidly increased to form an inverted peak; this recovery was completed by reaching into the high resistance close to the initial value within the following 16 h. It should be noticed that the somewhat smaller resistance in pure O_2 compared to the initial value is due to a shorter exposure of the sensor to the background atmosphere in between two successive

additions of hydrogen gas. According to Figure 5.2 (a), qualitative behavior of the sensor resistance is the same for three other partial pressures of hydrogen, 0.3, 0.03 and 0.003 T, although the lower peak value is different for each specific concentration.

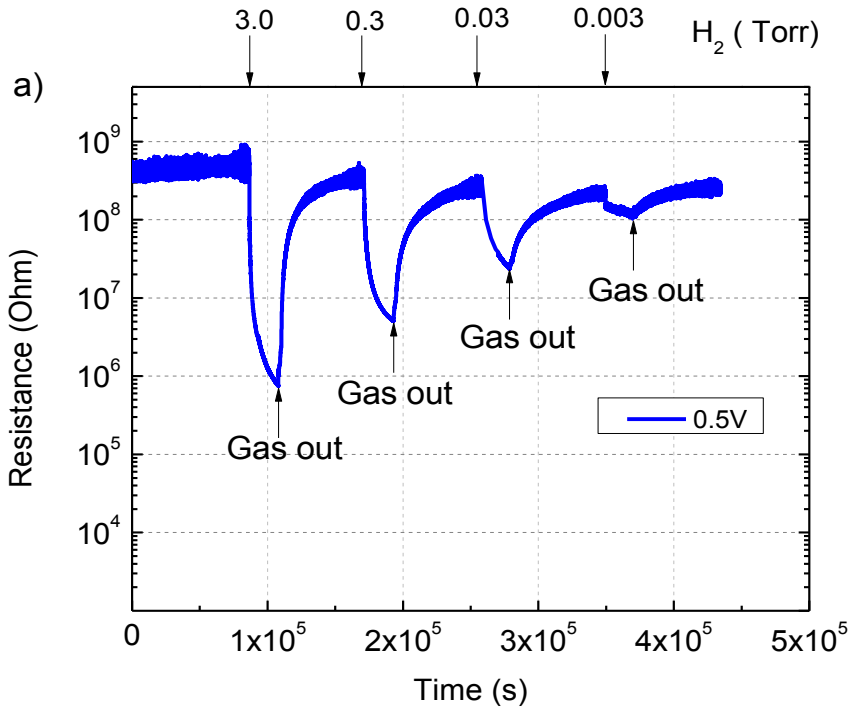

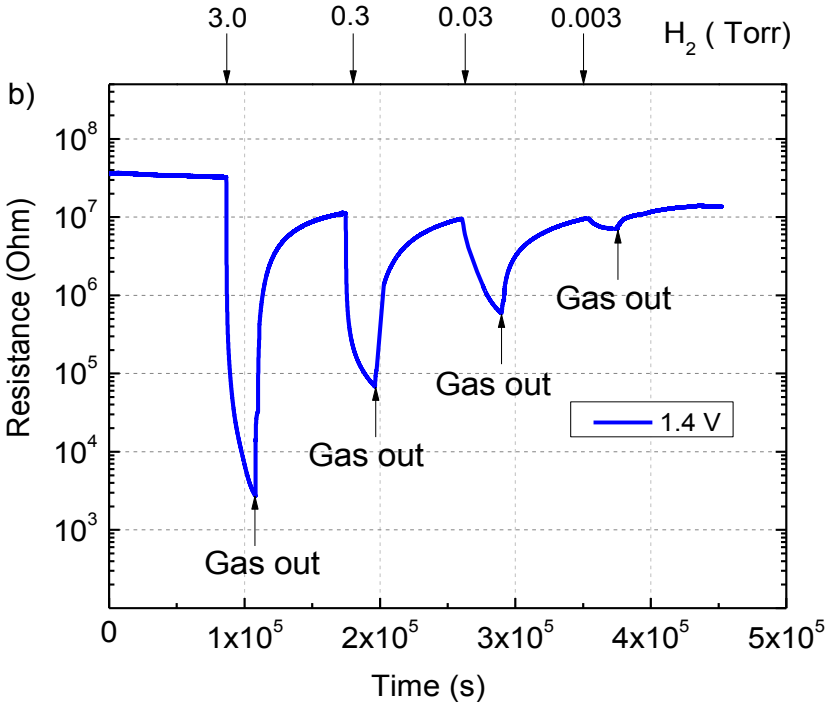

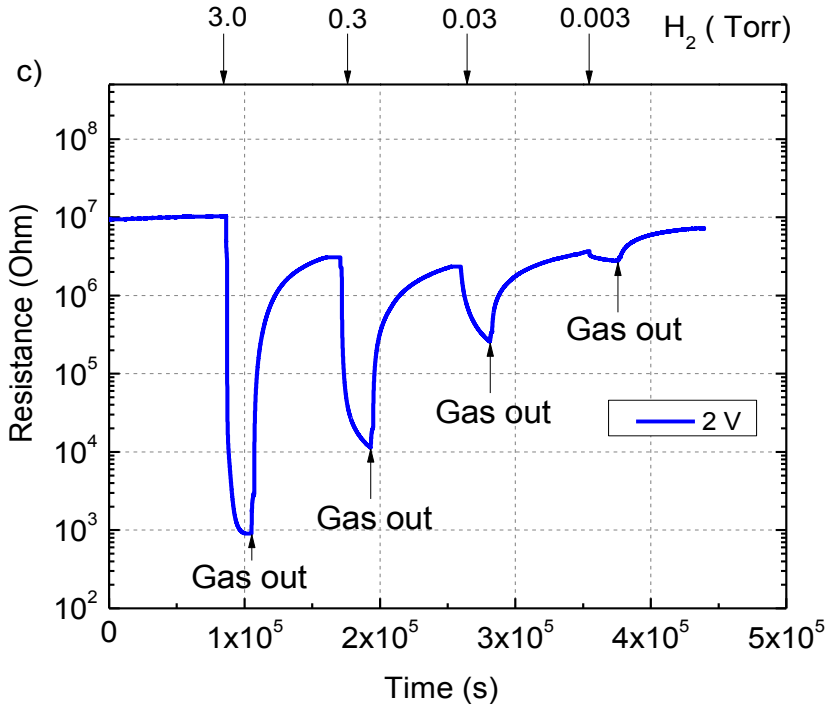

Figure 5.2. Response transients of the mesoporous Pt/TiO_2 hydrogen sensor in the background atmospheres of 160 Torr oxygen at various source voltages: (a) 0.5 V, (b) 1.4 V, and (c) 2 V

In addition, the sensor response was also measured under 1, 1.4 and 2 V for different concentration of H_2 by the same procedure as it is explained above for 0.5 V, see Figure 5.2. Increasing the applied voltage decreased the initial resistance of the sensor in pure oxygen. Otherwise, the sensor showed similar behaviors during the alternating exposure to hydrogen and oxygen gases. A four order of magnitude change in the resistance is typically seen due to exposure to 3 Torr of hydrogen. Also, the sensor resistance was notably decreased when it was exposed to only 0.003 Torr H_2, corresponding to a concentration of H_2 molecules of only 3.9 ppm in a normal atmosphere, or 20 ppm in the 160 Torr atmospheres used here. A solid-state sensor reacting to such small amounts of molecular hydrogen has not been reported earlier in literatures.

A formal *sensitivity measure* of the type

$$S = \frac{R_{O_2} - R_{H_2}}{R_{H_2}} \tag{5-1}$$

was investigated. Here, R_{O2} is the resistance of the sensor in the background (reference) atmosphere of pure O_2 at 160 Torr, and R_{H2} is the resistance in the end of the hydrogen exposure, represented by magnitudes of the inverted peaks in Figure 5.2 plots. Dependences of the value S on source voltage and H_2 partial pressure are shown in Figure 5.3.

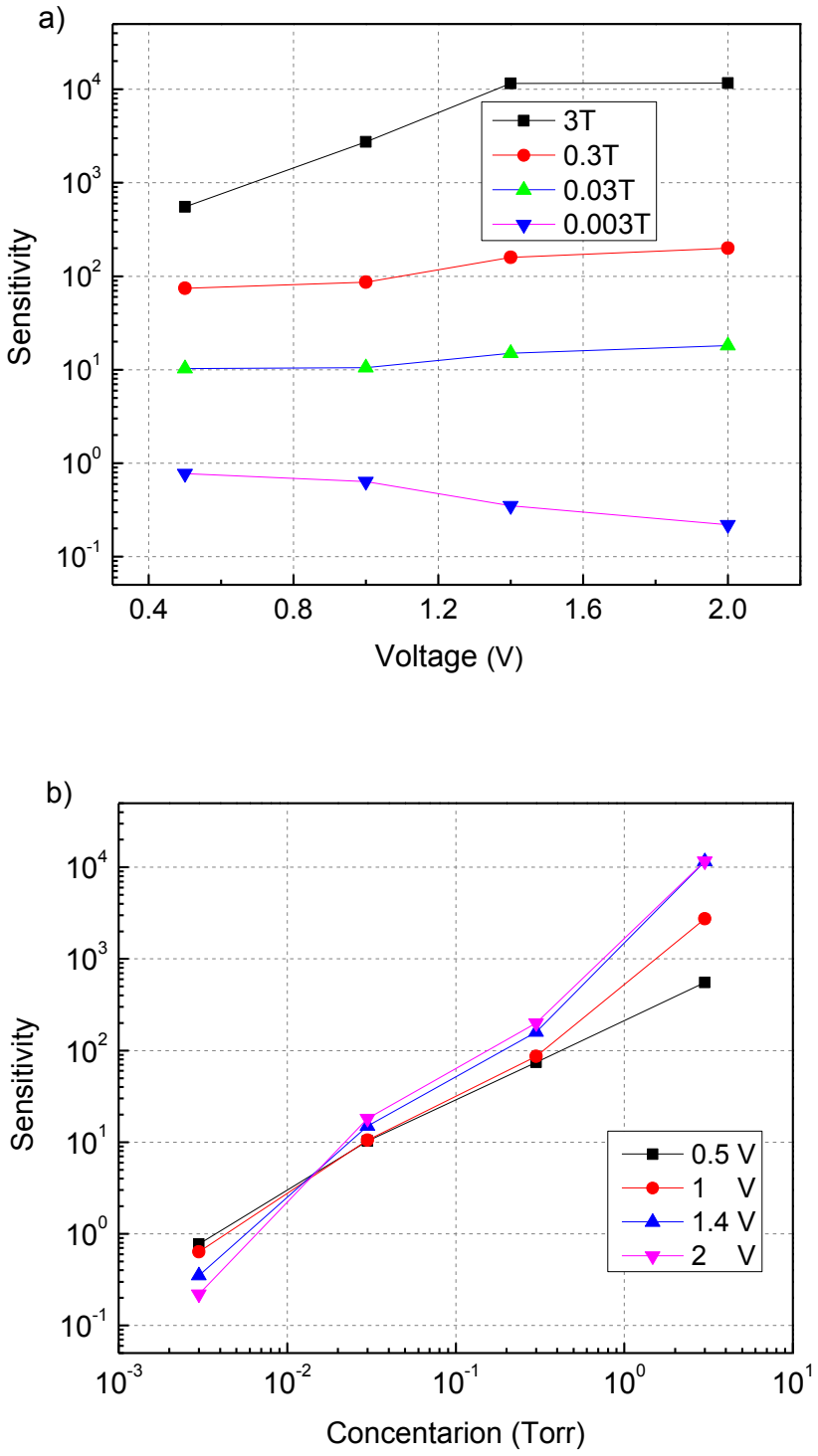

Figure 5.3. Sensitivity of the sensor versus voltage (a) and concentration of hydrogen (b) based on Figure 3 data

For a specific voltage, the sensitivity increases with the H_2 concentration. It also increases slightly with the source voltage, except for the lowest studied hydrogen pressure (0.003 Torr), for which better results were observed at smaller voltages. The highest values *S* were obtained for 3 Torr of H_2, varying from 550 at 0.5 V to 11670 at 2V. In Figure 5.3(a) it can be also noticed that the sensitivity saturates for the voltages above 1.4 V. A sharp sensitivity drop, not shown in the figure, was observed at all hydrogen concentrations for voltages higher than 2 V. A prolonged exposure of the sensor to such voltages may lead to an irreversible decrease of the sensitivity.

Peak resistance values on each of the Figure 5.2 curves can be fitted within a 20% or better accuracy with a power function of H_2 partial pressure, *p*,

$$R(p) = a \cdot p^b \tag{5-2}$$

where the parameter *b* varies from –0.73 to –1.18, depending on the source voltage, see Table X.

Table X. Value of the power function parameter *b* in Eq. (5-2) for different source voltages

Bias (V)	0.5	1.0	1.4	2.0
b-value	-0.73	-0.96	-1.12	-1.18

Thus, electrical conductance of the sample can be a *linear* response function of H_2 partial pressure for a properly selected source voltage in the range 1.0−1.4 V. This provides opportunities for practical utility of the present solid-state system in hydrogen-selective pressure gauges and transducers.

5.3.2 Response Time

In order to compare response time of the sensor under different voltages, the parameters t_{20}, t_{50} and t_{90} were defined to represent, respectively, periods of time during which the sensor resistance drops 20%, 50%, and 90% from its initial value, see Figure 5.2. These parameters are listed in Table XI for 3 Torr H_2 exposure at different source voltages. It can be mentioned that the response time has a notable dependence on the source voltage. Upon exposure to 3 Torr of hydrogen under 1.4 V, the sensor resistance dropped to 90% of initial value within about 4 minutes. Thus, in the view of both sensitivity (Figure 5.3) and response time (Table XI) data, a source voltage around 1.4 V is optimal for this device in hydrogen sensing applications.

Table XI. Response time for 3 Torr H_2 exposure at different source voltages

Voltage (V)	t_{20} (s)	t_{50} (s)	t_{90} (s)
0.5	12	38	546
1.4	19	47	223
2.0	31	49	385

The operating conditions (temperature, hydrogen concentration, and background atmosphere), sensitivity, and response time of this and typical earlier sensors based on TiO_2 are shown in Table XII. As can be seen, the present sensor device can be advantageous to the nanotube and sol-gel based sensors for its lower operating temperatures (26-28˚C) and a lower sensitivity threshold (20 ppm). It also provides response times better than in the nanotube sensors, and sensitivity comparable with the sol-gel type sensors.

Table XII. Comparison of operating conditions, sensitivity, and response time of current sensor and previous sensors

Sensor type	Temperature (˚C)	H_2 (ppm) / background gas	Sensitivity	t_{90} (s)
Mesoporous anodic TiO_2	26-28	20-20000 / O_2, N_2	0.35-11528 (1.4 V)	223-546
TiO_2 prepared by sol-gel method (Haidry et al. 2012)	100-350	300-10000 / air	10-10000	45-130
Highly ordered TiO_2 nanotubes (Şennik et al. 2010)	20-150	100-5000 / O_2, N_2	10-35	1800-3900

5.3.3 Sensing Mechanism

The mechanisms of hydrogen sensing in semiconducting catalytic systems remained unclear for a long time and different mechanisms have been introduced (Bates et al. 1979; Roy et al. 2003; Kim et al. 2006; Wang et al. 2010) . Some studies reveled that the presence of oxygen species on the surface is necessary for the sensitivity of TiO_2 based devices to hydrogen gas (Bates et al. 1979). It has been suggested that trapping of electrons from the conduction band of a metal oxide semiconductor by adsorbed oxygen molecules and return of these electrons to the conduction band by a reducing gas (H_2) are responsible for the hydrogen sensitivity (Wang et al. 2010). In a quest for information about the correct sensing mechanism, the effect of *background atmosphere type* and *source voltage polarity* on the performance of present hydrogen sensor was investigated. The response of the sensor to different concentrations of H_2 under 1 V in 160 Torr O_2 and N_2 backgrounds is shown in Figure 5.4. In contrast to the redox mechanism (Bates et al. 1979**;** Wang et al. 2010), by comparing the O_2 and N_2 curves shown in Figure 5.4, it can be concluded that the presence of oxygen molecules was *not* an essential factor for the hydrogen sensing measurements. On the contrary, the initial resistance, recovery values and flatness of the curves (at 0.3 and 3 Torr H_2) were higher for the O_2 atmosphere. This fact could be explained by partial blockage of the active sensor surface with products of a slow oxyhydrogen reaction (water and OH radicals). In chapters 3 and 4, we showed that the oxyhydrogen reaction can be initiated on a similar catalytic surface at 16 Torr H_2 even at room temperature. On the other hand, the order of magnitude variation in the sensor resistance in Figure 5.4 data was similar for the two background gases at all H_2 partial pressures.

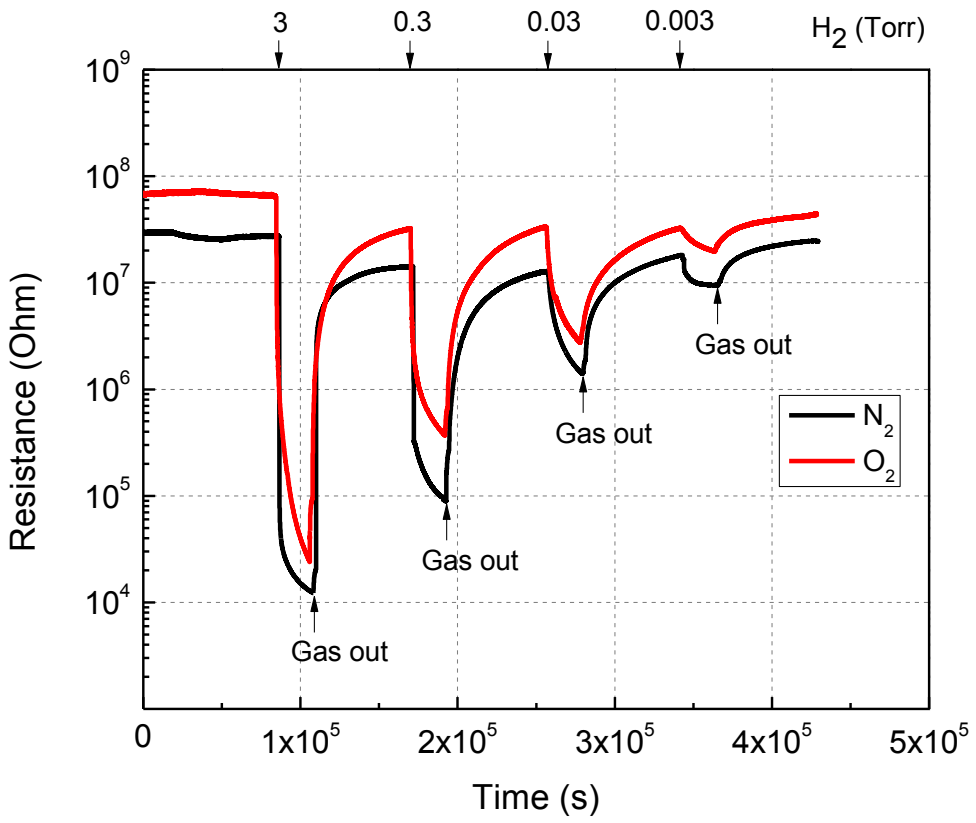

Figure 5.4. Comparative behavior of the sensor in the background atmospheres of 160 Torr oxygen and nitrogen under source voltage 1 V

Figure 5.5 shows variation of the sensor resistance versus time for a *high vacuum* background (10^{-7} Torr) under the voltage 1 V. It can be seen that the sensor responded to and recovered from all the different concentrations of H_2 approximately at the same order of magnitude variation. This result provides further evidence toward the slow oxyhydrogen reaction hypothesis of the previous paragraph, because in this experiment the sensor surface remains free of any compound molecules of radicals at all times. Thus, the background gas (O_2 or N_2) only diminishes the sensor response, especially at the lower H_2 concentrations. Furthermore, independence of the response on the gas type,

Figure 5.4, suggests that molecules of the background gas participate only in physisorption processes on the sensor surface.

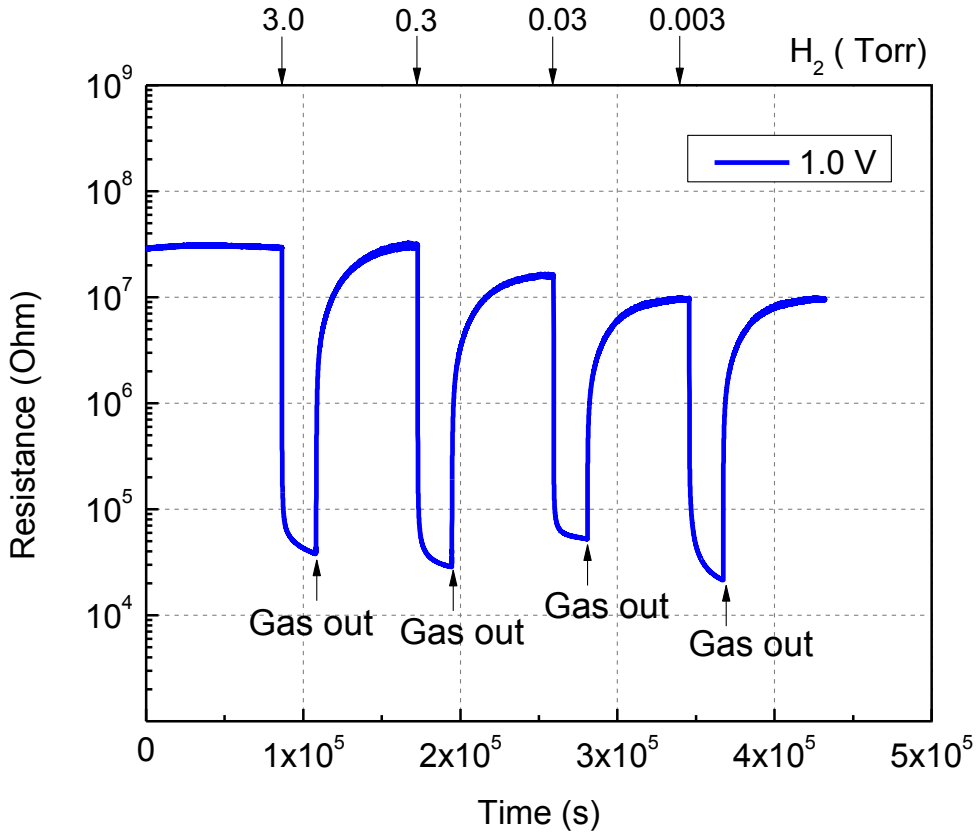

Figure 5.5. Sensor resistance variations in 10^{-7} Torr vacuum background for different concentrations of H_2 under source voltage 1 V

Recent studies show different mechanisms in which the hydrogen molecules dissociate and form atomic hydrogen on the metal surface. These hydrogen atoms will then diffuse through the metal and precipitate at the metal/semiconductor interface, decreasing the metal work function, and therefore reducing the Schottky barrier height (Roy et al. 2003; Shimizu et al. 2007). Figure 5.6 shows the sensor responses when it was

exposed to 3 Torr of hydrogen in high vacuum (10^{-7} Torr) under +1.4 and -1.4 V at room temperature.

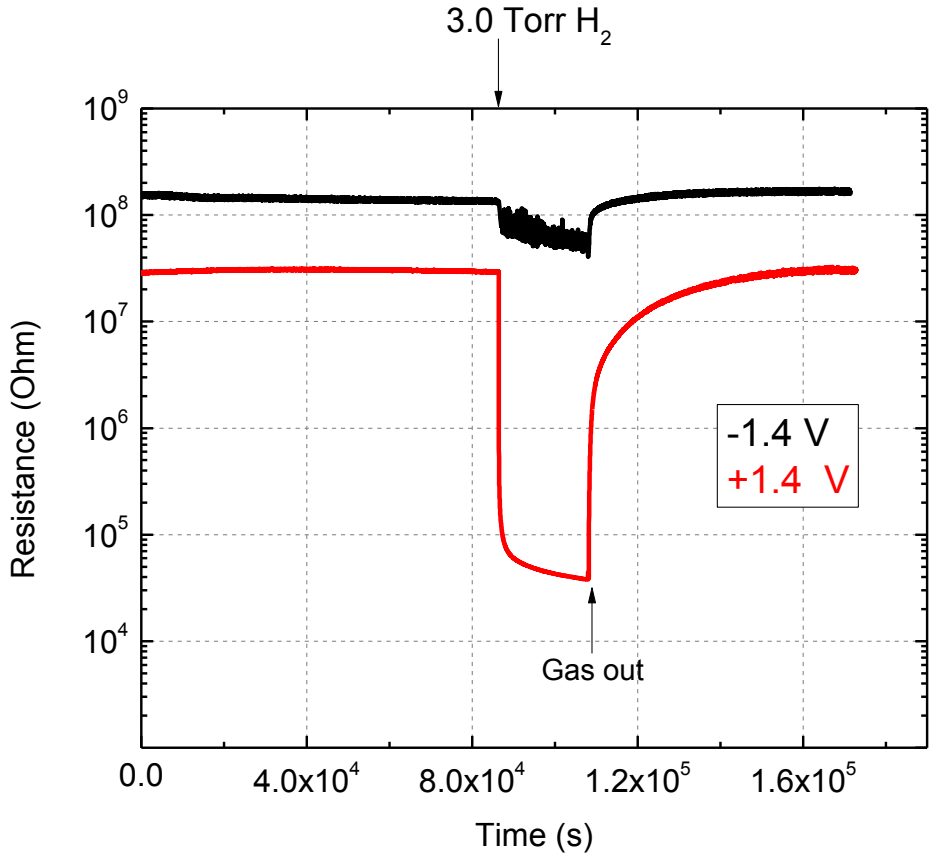

Figure 5.6. The variation of sensor resistance versus time in high vacuum (10^{-7} Torr) for 3 Torr of H_2 under source voltages +1.4 and −1.4 V

It can be seen that the order of magnitude variation in the sensor resistance under the positive source voltage is noticeably greater compared to the response at the negative voltage. This result indicates that the barrier reduction mechanisms based on electronic conductance is not fully applicable to the present sensor type. We suggest that *ionic*

transport in TiO_2 serving as a solid electrolyte, also plays an important role in the sensing performance reported here. In particular, hydrogen ions (H^+) generated on the Pt nanomesh under positive bias in the presence of hydrogen adsorbate species are drifting toward the back Ti contact of the sensor to recombine there with electrons arriving from the external circuit. A negatively biased catalytic electrode, on the contrary, cannot produce a significant amount of hydrogen ions, and therefore the sensor response was minute at the negative source voltage. It is also possible that the mechanism of oxygen vacancy (V_O) drift in TiO_{2-x} areas under electrical potential (Wu and McCreery 2009; Miller et al. 2010) is intertwined with the H^+ diffusion process in the present sensor type.

5.4 Conclusions

The transient response of a $Pt/TiO_2/Ti$ sensor based on anodically grown mesoporous titania was studied at room temperature for different hydrogen concentrations and applied source voltages, and in three different background (reference) atmospheres: 160 Torr O_2, 160 Torr N_2, and 10^{-7} Torr vacuum. Comparable results were obtained in these atmospheres to reveal that the response of the sensor is not influenced by adsorbed O^- species (Bates et al. 1979), and the background gas molecules are likely to participate only in physisorption processes on the sensor surface. The applied source voltage in the range of 0.5−2 V had a great effect on the sensor sensitivity with the highest sensitivity observed at 1.4 V. For the 0.03−3 Torr H_2 exposures, the sensitivity increased with the source voltage until 1.4 V and then saturated at about 2 V. Irreversible changes of the sensor behavior occurred for voltages higher than 2 V, at which the sensitivity decreased significantly. For a source voltage in the range 1.0−1.4 V, electrical conductance of the sensor can be a linear response function of the H_2 partial pressure. The obtained data suggests that ionic conductance and vacancy diffusion processes in the mesoporous titania contributes to the resistive response of the sensor during hydrogen exposure.

CHAPTER 6

CONCLUSIONS AND FUTURE WORK

6.1 Overall Conclusions

This study revealed two distinct modes of catalytic oxidation of hydrogen to water on a mesoporous Pt/TiO_2 structure with an electrically continuous 15 nm mesh-like Pt layer. The structure supported a continuous oxidation of hydrogen to water starting at room temperature in 160 Torr O_2 and also performed as a chemical-electrical transducer. Along with the usual fast reaction over the nanodispersed Pt, a 1200 times slower mode of the reaction is revealed by studying the reaction-induced currents. This slow mode leads to a surprisingly strong stationary chemicurrent at electron yield 0.04, electromotive force −0.32 V, and short-circuit current density $12\mu A/cm^2$ at room temperature. This phenomenon is explained by involvement of both Pt and TiO_2 phases in the slow reaction flow, where a proton spillover mechanism of the observed electromotive force is suggested. The overall reaction current kinetics contains many autonomously formed features including peaks and alterations of the charge flow direction to manifest competition between various surface reaction regimes. These studies provide interesting opportunities for smart chemical sensors, transducers, and novel analytical tools.

The effect of temperature on the electric current induced in the mesoporous Pt/TiO_2 structure was investigated by the room temperature surface chemical reaction of hydrogen and oxygen. This helped to unveil the physical origin of this current and the related electromotive force (chemi-EMF). It was observed that the temperature dependence of this reaction current has a clear multipeak structure, suggesting that at

least two distinct processes contribute to the current generation. The output current represents the interplay of both chemical and electrical processes, evidenced by the metastability of the room temperature reaction and by matching of the current peaks with the water desorption peak for TiO_2.

In order to study the hydrogen sensing properties of a $Pt/TiO_2/Ti$ system, the resistive sensor response between the Pt and Ti terminals of the structure was investigated at room temperature for different partial pressures of H_2 gas (0.003−3 Torr) and different source voltages (0.5−2.0 V). A maximum resistance effect, reaching four orders of the magnitude for 3 Torr H_2 in 160 Torr O_2 is obtained at the bias voltage 1.4 V, and a strong effect is detected for only 0.003 Torr, or 20 ppm H_2 concentration. For voltages in the range 1.0−1.4 V, electrical conductance of the sample is about a linear function of the H_2 partial pressure in the gas phase. Influence of the background atmosphere (O_2, N_2 and vacuum) and the effect of bias reversal were investigated also, leading to a conclusion that the sensing mechanism can be related to ionic transport in the TiO_2 layer.

6.2 Future work

In the present study, chemicurrent measurements were investigated on mesoporous TiO_2 systems while other types of TiO_2 such as nanotubes can also be considered to reveal the effect of porosity on the chemicurrent magnitudes. A proton spillover mechanism was introduced as a possible reason for the activity of Pt/TiO_2 system during the slow reaction mode. In order to validate this hypothesis, other

metal oxide nanostructures such as ZrO_2, NiO, WO_3 and other similar systems will be investigated in the future studies. All of these oxide layers can be grown by oxidizing their native metals to provide a base electrical contact and a mechanical support. Also, the chemicurrent measurements can be used to compare the catalytic activities of different metal-metal oxide nanostructures such as Pt/TiO_2, Pt/ZrO_2, Rh/TiO_2, Rh/ZrO_2, etc. In this research, the chemicurrent studies were carried out in the oxyhydrogen atmosphere. For the future studies, other fundamental industrial processes such as oxidation of CO and CH_4 can also be considered.

CITED LITERATURE

Abdullah, N., and Kamarudin, S.K. "Titanium Dioxide in Fuel Cell Technology: An Overview". *Journal of Power Sources,* 278 : 109–18, 2015.

Abuelnuor, A.A.A., Wahid, M.A., Hosseini, S.E., Saat, A., Saqr, K.M., Sait, H.H., and Osman, M. "Characteristics of Biomass in Flameless Combustion: A Review". *Renewable and Sustainable Energy Reviews,* 33: 363–70, 2014.

Ahonen, P.P., Kauppinen, E.I., Joubert, J.C., Deschanvres, J.L., and Tendeloo, G.V. "Preparation of Nanocrystalline Titania Powder via Aerosol Pyrolysis of Titanium Tetrabutoxide". *Journal of Materials Research,* 14 (10): 3938–3948, 1999.

Albert, M., Gao, Y-M., Toft, D., Dwight, K., and Wold, A. "Photoassisted Gold Deposition of Titanium Dioxide". *Materials Research Bulletin*, 27(8), 961–966, 1992.

Alfano, O.M., Bahnemann, D., Cassano, E., Dillert, R., and Goslich, R."Photocatalysis in Water Environments Using Artificial and Solar Light". *Catalysis Today*, 58: 199–230, 2000.

Artizzu, P., Garbowski, E., Primet, M., Brulle, Y., and Saint-Just, J. "Catalytic Combustion of Methane on Aluminate-Supported Copper Oxide" . *Catalysis Today,* 47: 83–93, 1999.

Aruna, S.T., Tirosh, S., and Zaban, A. "Nanosize Rutile Titania Particle Synthesis via a Hydrothermal Method without Mineralizers". *Journal of Materials Chemistry,* 10 (10): 2388–91, 2000.

Balat, M. "Potential Alternatives to Edible Oils for Biodiesel Production – A Review of Current Work". *Energy Conversion and Management,* 52 (2): 1479–92, 2011.

Balat, M., Balat, M., Kırtay, E., and Balat, H. "Main Routes for the Thermo-Conversion of Biomass into Fuels and Chemicals. Part 1: Pyrolysis Systems". *Energy Conversion and Management,* 50 (12): 3147–57, 2009.

Baldwin, T.R., and Burch, R."Catalytic Combustion of Methane over Supported Palladium Catalysts I . Alumina Supported Catalysts". *Applied Catalysis,* 66: 337– 358, 1990.

Baranowski, L. L.,Warren, E. L., and Toberer, E.S. "High-Temperature High-Efficiency Solar Thermoelectric Generators". *Journal of Electronic Materials,* 43(6): 2348–55, 2014.

Barth, J.V., Zambelli, T., Wintterlin, J., and Ertl, G. "Hot Precursors in The Adsorption of Molecular Oxygen on Ag(110)." *Chemical Physics Letters*, 270: 152–156, 1997.

Bates, J.B., Wang, J.C., and Perkins, R.A. “Mechanisms for Hydrogen Diffusion in TiO_2”. *Physical Review B,* 19: 4130−4139, 1979.

Berndes, G., Hoogwijk, M., and Broek, R.V. “The Contribution of Biomass in the Future Global Energy Supply: A Review of 17 Studies”. *Biomass and Bioenergy*, 25 (1): 1–28, 2003.

Bhaumik, A., Haque, A., Karnati, P., Taufique, M.F.N., Patel, R., and Ghosh, K. “Copper Oxide Based Nanostructures for Improved Solar Cell Efficiency”. *Thin Solid Films,* 572 : 126–33, 2014.

Böttcher, A., and Niehus, H. “Chemisorptive Electron Emission versus Sticking Probability”. *Physical Review B,* 64 (4): 045407, 2001.

Böttcher, A., Imbeck, R., Morgante, A., and Ertl, G. “Nonadiabatic Surface Reaction: Mechanism of Electron Emission in the Cs+ O_2 System”. *Phisical Review Letters,* 65 (16): 2035–37, 1990.

Bozo, C., Guilhaume, N., Garbowski, E., and Primet, M. “Combustion of Methane on CeO_2–ZrO_2 Based Catalysts”. *Catalysis Today,* 59: 33–45, 2000.

Brady, K., Sung, C., and T’ien, J. “Ignition Propensity of Hydrogen/air Mixtures Impinging on a Platinum Stagnation Surface”. *International Journal of Hydrogen Energy,* 35 (20): 11412–23, 2010.

Brennan, L., and Owende, P. “Biofuels from microalgae—A Review of Technologies for Production, Processing, and Extractions of Biofuels and Co-Products”. *Renewable and Sustainable Energy Reviews,* 14 (2): 557–77, 2010.

Buonomano, A., Calise, F., Ferruzzi, G., and Palombo, A. “Molten Carbonate Fuel Cell: An Experimental Analysis of a 1kW System Fed by Landfill Gas”. *Applied Energy,* 140: 146–60, 2015.

Burch, R., Loader, P.K., and Urbano, F.J. “Some Aspects of Hydrocarbon Activation on Platinum Group Metal Combustion Catalysts”. *Catalysis Today,* 27 (1-2): 243–48, 1996.

Carp, O. “Photoinduced Reactivity of Titanium Dioxide”. *Progress in Solid State Chemistry,* 32 (1-2): 33–177, 2004.

Carrette, L., Friedrich, K.A., and Stimming, U. “Fuel Cells - Fundamentals and Applications”. *Fuel Cells,* 1 (1): 5–39, 2001.

Chandan, A., Hattenberger, M., El-kharouf, A., Du, S., Dhir, A., Self, V., Pollet, B.G., Ingram, A., and Bujalski,. W. “High Temperature (HT) Polymer Electrolyte Membrane Fuel Cells (PEMFC) – A Review”. *Journal of Power Sources,* 231: 264–78, 2013.

Chapin, D. M., Fuller, C.S and Pearson, G.L. “A New Silicon P-N Junction Photocell for Converting Solar Radiation into Electrical Power”. *Journal of Applied Physics,* 25 (5): 676, 1954.

Charlier, R.H. “A ‘sleeper’ Awakes: Tidal Current Power”. *Renewable and Sustainable Energy Reviews,* 7 (6): 515–29, 2003.

Chen, K., Xie, K., Feng, X.,Wang, S., Hu, R., Gu, H., and Li, Y. “An Excellent Room-Temperature Hydrogen Sensor Based on Titania Nanotube-Arrays”. *International Journal of Hydrogen Energy,* 37 (18). Elsevier Ltd: 13602–9, 2012.

Chen, S., Zhang, P., Zhuang, D., and Zhu,W. “Investigation of Nitrogen Doped TiO_2 Photocatalytic Films Prepared by Reactive Magnetron Sputtering”. *Catalysis Communications,* 5 (11): 677–80, 2004.

Chhabra, V., Pillai,V., Mishra, B.K., and Morrone, A. “Synthesis, Characterization, and Properties of Microemulsion-Mediated Nanophase TiO_2 Particles”. *Langmuir,* 11(9): 3307–3311, 1995.

Chopra, K. L., Paulson, P.D., and Dutta, V. “Thin-Film Solar Cells: An Overview”. *Progress in Photovoltaics: Research and Applications,* 12 (23): 69–92, 2004.

Choudhary, T.V., Banerjee, S., and Choudhary, V.R. “Catalysts for Combustion of Methane and Lower Alkanes”. *Applied Catalysis A: General,* 234 (1-2): 1–23, 2002.

Christian, E., Lødeng, R., and Holmen, A. “A Review of Catalytic Partial Oxidation of Methane to Synthesis Gas with Emphasis on Reaction Mechanisms over Transition Metal Catalysts”. *Applied Catalysis A: General,* 346 (1-2): 1–27, 2008.

Chua, L.O. “Memristor-The Missing Circuit Element ”. *Transactions on Circuit Theory,* 18(5): 507–519, 1971.

Ciuparu, D., and Pfefferle, L. “Support and Water Effects on Palladium Based Methane Combustion Catalysts”. *Applied Catalysis A: General,* 209 (1-2): 415–28, 2001.

Conner, W. C., and Falconer, J.L.“Spillover in Heterogeneous Catalysis”. *Chemical Reviews,* 95 (3): 759–88, 1995.

Dasari, S.K., Hashemian, M.A., Mohan, J., and Karpov., E.G. “A Nonthermal Chemicurrent Effect of Hydrogen Adsorption on Pt/SiC Planar Nanostructures at Normal Ambient Conditions.” *Chemical Physics Letters,* 553: 47–50, 2012.

Dhankhar, M., Singh, O.P., and Singh,V.N. “Physical Principles of Losses in Thin Film Solar Cells and Efficiency Enhancement Methods”. *Renewable and Sustainable Energy Reviews,* 40: 214–23, 2014.

Diamanti, M.V., and Pedeferri, M.P. “Effect of Anodic Oxidation Parameters on the Titanium Oxides Formation”. *Corrosion Science,* 49 (2): 939–48, 2007.

Dicks, A.L. “Molten Carbonate Fuel Cells”. *Current Opinion in Solid State and Materials Science,* 8 (5): 379–83, 2004.

Diebold, U. “Structure and Properties of TiO_2 Surfaces: A Brief Review”. *Applied Physics A: Materials Science & Processing,* 76 (5): 681–87, 2003.

Duan, H., Yan, C., and Wang, F. “Growth Process of Plasma Electrolytic Oxidation Films Formed on Magnesium Alloy AZ91D in Silicate Solution”. *Electrochimica Acta,* 52 (15): 5002–9, 2007.

Dunn, S. “Hydrogen Futures: Toward a Sustainable Energy System”. *International Journal of Hydrogen Energy,* 27 (3): 235–64, 2002.

Eguchi, K., and Arai, H. “Low Temperature Oxidation of Methane over Pd-Based Catalysts–effect of Support Oxide on the Combustion Activity”. *Applied Catalysis A: General,* 222 (1-2): 359–67, 2001.

Elam, C.C, Padrã, C.E.G., Sandrock, G., Luzzi, A., Lindblad, P., and Fjermestad, E. “Realizing the Hydrogen Future: the International Energy Agency’s Efforts to Advance Hydrogen Energy Technologies”. *International Journal of Hydrogen Energy*, 28: 601–7, 2003.

Ellis, M.W., Spakovsky, M.R.V., and Nelson, D.J. “Fuel Cell Systems: Efficient, Flexible Energy Conversion for the 21st Century”. *Proceedings of the IEEE,* 89 (12): 1808–18, 2001.

Faaij, A. “Modern Biomass Conversion Technologies”. *Mitigation and Adaptation Strategies for Global Change*, 11: 343–375, 2006.

Fedtke, P., Wienecke, M., Bunescu, M.C., Pietrzak, M., Deistung, K., and Borchardt, E. “Hydrogen Sensor Based on Optical and Electrical Switching.” *Sensors and Actuators B: Chemical* 100 : 151–57, 2004.

Fernandes, N.E., Park, Y.K., and Vlachos, D.G. “The Autothermal Behavior of Platinum Catalyzed Hydrogen Oxidation: Experiments and Modeling”. *Combustion and Flame,* 118 (1-2): 164–78, 1999.

Fischer, G., and Schrattenholzer, L.“Global Bioenergy Potentials through 2050”. *Biomass and Bioenergy*, 20: 151–59, 2001.

Frese, K.W, and Chen, C. “Theoretical Models of Hot Carrier Effects at Metal-Semiconductor Electrodes” *Journal of Electrochemical Society,* 139 (11): 3234–43, 1992.

Gandhi, K., Dixit, B.K., and Dixit, D.K. “Effect of Addition of Zirconium Tungstate, Lead Tungstate and Titanium Dioxide on the Proton Conductivity of Polystyrene Porous Membrane”. *International Journal of Hydrogen Energy,* 37 (4): 3922–30, 2012.

Gebreegziabher, T., Oyedun, A.O., Luk, H.T., Lam, T.Y.G., Zhang, Y., and Hui, C.W. “Design and Optimization of Biomass Power Plant”. *Chemical Engineering Research and Design,* 92 (8): 1412–27, 2014.

Geeter, E.D., Geeter, E.D., Mangan, M., Spaepen, S., Stinissen, W., and Vennekens, G. “Alkaline Fuel Cells for Road Traction”. *Journal of Power Source,* 80: 207–12, 1999.

Gergen, B., Nienhaus, H., Weinberg, W. H., and McFarland, E. W. “Chemically Induced Electronic Excitations at Metal Surfaces”. *Science* 294: 2521−2523, 2001.

Gerischer, H., and Heller, A. “The Role of Oxygen in Photooxidation of Organic Molecules on Semiconductor Particles”. *The Journal of Physical Chemistry* 95 (13): 5261–67, 1991.

Ginley, D., Green, M.A., Collins, R. “Solar Energy Conversion Toward 1 Terawatt”. *Harnessing Materials for Energy,* 33: 355–73, 2008.

Greber, T. “Charge-Transfer Induced Particle Emission in Gas Surface Reactions”. *Surface Science Reports,* 28 (1-2): 1–64, 1997.

Green, M.A., Emery, K., Hishikawa, Y., Warta, W., and Dunlop, E.D. “Solar Cell Efficiency Tables (version 39)”. *Progress in Photovoltaics*, 20: 12–20, 2012.

Groppi, G., Cristiani, C., Beretta, A. and Forzatti, P. “Catalytic Combustion for the Production of Energy, in Catalysis for Sustainable Energy Production”. (eds P. Barbaro and C. Bianchini), Wiley-VCH Verlag GmbH & Co. KGaA, Weinheim, Germany, 2009.

Gross, E., and Somorjai, G.A. “The Impact of Electronic Charge on Catalytic Reactivity and Selectivity of Metal-Oxide Supported Metallic Nanoparticles.” *Topics in Catalysis* 56 (12): 1049–58, 2013.

Günes, S., and Sariciftci, N.S. “Hybrid Solar Cells”. *Inorganica Chimica Acta,* 361 (3): 581–88, 2008.

Hagemann, U., Timmer, M., Krix, D., Kratzer, P., and Nienhaus, H. “Electronic Excitations in Magnesium Epitaxy: Experiment and Theory”. *Physical Review B,* 82 (15): 155420, 2010.

Haidry, A.A, Puskelova, J., Plecenik, T., Durina, P., Gregus, J., Truchly, M., Roch, T., Zahoran, M., Vargova, M., Kus, P., Plecenik, A., and Plesch, G. “Characterization and Hydrogen Gas Sensing Properties of TiO_2 Thin Films Prepared by Sol–gel Method.” *Applied Surface Science* 259 : 270–75, 2012.

Haidry, A.A, Schlosser, P., Durina, P., Mikula, M., Tomasek, M., Plecenik, T., Roch, T., Pidik, A., Stefecka, M., Noskovic, J., Zahoran, M., Kus, P., and Plecenik, A. "Hydrogen Gas Sensors Based on Nanocrystalline TiO_2 Thin Films". *Central European Journal of Physics* 9 (5): 1351–56, 2011.

Harada, H., and Ueda, T. "Photocatalfshimiytic Activity of Ultra-fine Rutlle in Methanol-water Solution and Dependence of Activity on Particle Size". *Chemical Physics Letters*, 106 (3): 229–31, 1984.

Hashemian, M.A., Dasari, S.K., and Karpov, E.G. "Separation of Hot Electron Current Component Induced by Hydrogen Oxidation on Resistively Heated Pt/n-GaP Schottky Nanostructures". *Journal of Vacuum Science & Technology A: Vacuum, Surfaces, and Films,* 31 (2): 020603, 2013.

Hashimoto, K., Irie, H., and Fujishima, A. "TiO_2 Photocatalysis: A Historical Overview and Future Prospects". *Japanese Journal of Applied Physics,* 44 (12): 8269–85, 2005.

Henderson, M. A. "The Influence of Oxide Surface Structure on Adsorbate Chemistry: Desorption of Water from the Smooth , the Microfaceted and the Ion Sputtered Surfaces of TiO_2 (100)". *Surface Science,* 319: 315–328, 1994.

Herman, G.S., and Gao, Y. "Growth of Epitaxial Anatase (001) and (101) Films". *Thin Solid Films*, 397: 157–61, 2001.

Hervier, A., Renzas, J.R., and Park, J.Y. "Hydrogen Oxidation-Driven Hot Electron Flow Detected by Catalytic Nanodiodes". *Nano Letters*, 9(11): 3930–3933, 2009.

Hoffmann, M.R, Martin, S.T., Choi, W., and Bahnemannt, D.W. "Environmental Applications of Semiconductor Photocatalysis". *Chemical Reviews*, 95(1): 69–96, 1995.

Hu, X., Duan, S., Wang, L., and Liao, X. "Memristive Crossbar Array with Applications in Image Processing". *Science China Information Sciences,* 55 (2): 461–72, 2011.

Huang, J.R., Hsu, W.C., Chen, H.I, and Liu, W.C. "Comparative Study of Hydrogen Sensing Characteristics of a Pd/GaN Schottky Diode in Air and N_2 Atmospheres." *Sensors and Actuators B: Chemical* 123 : 1040–48, 2007.

Hübert, T., Boon-Brett, L., Black, G.,and Banach, U. "Hydrogen Sensors – A Review." *Sensors and Actuators B: Chemical* 157 : 329–52, 2011.

Humphrey, T.E., O'Dwyer, M.F., and Linke, H. "Power Optimization in Thermionic Devices". *Journal of Physics D: Applied Physics,* 38 (12): 2051–54, 2005.

Hyldgaard, P., and Mahan, G.D. "Phonon Superlattice Transport". *Physical Review B*, 56 (17): 754–57, 1997.

Ikeda, H., Sato, J., and Williams, F.A. “Surface Kinetics for Catalytic Combustion of Hydrogen-Air Mixtures on Platinum at Atmospheric Pressure in Stagnation Flows”. *Surface Science,* 326 (1-2): 11–26, 1995.

Iwahara, H. “Prospect of Hydrogen Technology Using Proton-Conducting Ceramics”. *Solid State Ionics,* 168 (3-4): 299–310, 2004.

Iwasaki, M., Hara, M., and Ito, S. “Facile Synthesis of Nanocrystalline Anatase Particles from Titanyl Sulfate”. *Journal of Materilas Science Letters*, 17: 1769–1771, 1998.

Jacobson, M.Z., Colella, W.G., and Golden, D.M. “Cleaning the Air and Improving Health with Hydrogen Fuel-Cell Vehicles”. *Science,* 308 (5730): 1901–5, 2005.

Tanguay, J.F., Suib, S.L., and Coughlin, R.W. “Dichloromethane Photodegradation Using Titanium Catalysts”. *Journal of Catalysis*, 117: 335–47, 1989.

Jana, A.K. “Solar Cells Based on Dyes”. *Journal of Photochemistry and Photobiology A: Chemistry,* 132 (1-2): 1–17, 2000.

Jeong, D.S., Schroeder, H., Breuer, U., and Waser, R. “Characteristic Electroforming Behavior in Pt/TiO_2/Pt Resistive Switching Cells Depending on Atmosphere”. *Journal of Applied Physics,* 104 (12): 123716, 2008.

Jo, S.H., Kim, K.H., and Lu, W. “Programmable Resistance Switching in Nanoscale Two-Terminal Devices”. *Nano Letters,* 9 (1): 496–500, 2009.

Jo, S.H., and Lu., W. “CMOS Compatible Nanoscale Nonvolatile Resistance Switching Memory”. *Nano Letters,* 8 (2): 392–97, 2008.

Jones, A.C., and Chalker, P.R. “Some Recent Developments in the Chemical Vapour Deposition of Electroceramic Oxides”. *Journal of Physics D: Applied Physics,* 36: 80–95, 2003.

Karpov, E.G., and Nedrygailov, I.I. “Solid-State Electric Generator Based on Chemically Induced Internal Electron Emission in Metal-Semiconductor Heterojunction Nanostructures”. *Applied Physics Letters,* 94 (21): 214101, 2009.

Keck, K. E., Kasemo, B., and Hogberg, T. H. “Studies of Combustion Related Surface Combined UHV-atm Pressure Equipment”. *Surface Science,* 126,469– 478, 1983.

Kerres, J.A. “Blended and Cross-Linked Ionomer Membranes for Application in Membrane Fuel Cells”. *Fuel Cells,* 5 (2): 230–47, 2005.

Kim, H., Sah, M.,Yang, C., Roska, T., and Chua, L.O. “Memristor Bridge Synapses”. *Proceedings of the IEEE,* 100 (6): 2061–70, 2012.

Kim, H.S, Moon, W.T., Jun, Y.K., and Hong, S.H. "High H_2 Sensing Performance in Hydrogen Trititanate-Derived TiO_2." *Sensors and Actuators B: Chemical* 120: 63–68, 2006.

Kim, S.M, Lee, S.J., Kim, S.H., Kwon, S., Yee, K.J., Song, H., Somorjai, G.A., and Park, J.Y. "Hot Carrier-Driven Catalytic Reactions on Pt-CdSe-Pt Nanodumbbells and Pt/GaN under Light Irradiation." *Nano Letters* 13 (3): 1352–58, 2013.

Knotek, M.L. "Characterization of Hydrogen Species TiO_2 by Electron-Stimulated Desorption". *Surface Science Letters*, 91: L17–L22, 1980.

Koutsoyiannis, D. "Scale of Water Resources Development and Sustainability: Small Is Beautiful, Large Is Great". *Hydrological Sciences Journal,* 56 (4): 553–75, 2011.

Krix, D., Nünthel, R., and Nienhaus, H. "Chemical Interaction of H and D Atoms with Ag / H:p–Si(111) Thin Film Diodes". *Journal of Vacuum Science & Technology A: Vacuum, Surfaces, and Films,* 25 (4): 1156, 2007.

Kucharczyk, B., Tylus, W., and Kpiński, L. "Pd-Based Monolithic Catalysts on Metal Supports for Catalytic Combustion of Methane". *Applied Catalysis B: Environmental,* 49 (1): 27–37, 2004.

Kul R.C., Ryoo, M.W., Ryu, I.S., and Kang, S.K. "Catalytic Combustion of Methane over Supported Bimetallic Pd Catalysts: Effects of Ru or Rh Addition". *Catalysis Today,* 47 (1-4): 141–47, 1999.

Lee, J.H., and Trimm, D.L. "Catalytic Combustion of Methane". *Fuel Processing Technology,* 42 (2-3): 339–59, 1995.

Legrini, O., Oliveros, E., and Braun, A.M. "Photochemical Processes for Water Treatment". *Chemical Reviews,* 93 (2): 671–98, 1993.

Levy, R. "The Kinetics and Mechanism of Spillover". *Journal of Catalysis* 32 (2): 304–14, 1974.

Li, G.H., Yang, L., Jin, Y.X., and Zhang, L.D. "Structural and Optical Properties of TiO_2 Thin Film and TiO_2 + 2 Wt .% $ZnFe_2O_4$ Composite Film Prepared by r.f. Sputtering". *Thin Solid Films*, 368: 163–67, 2000.

Litter, M. "Heterogeneous Photocatalysis Transition Metal Ions in Photocatalytic Systems". *Applied Catalysis B: Environmental,* 23 (2-3): 89–114, 1999.

Liu, S.X., Qu, Z.P., Han, X.W., and Sun, C.L. "A Mechanism for Enhanced Photocatalytic Activity of Silver-Loaded Titanium Dioxide". *Catalysis Today,* 93-95: 877–84, 2004.

Lough, B., Lee, S.P., Lewis, R.A., and Zhang, C. “Electronic Thermal Transport and Thermionic Cooling in Semiconductor Multi-Quantum-Well Structures”. *Computer Physics Communications,* 142 (1-3): 274–80, 2001.

Lucia, U. “Overview on Fuel Cells”. *Renewable and Sustainable Energy Reviews,* 30: 164–69, 2014.

Ludin, N.A., Al-Alwani Mahmoud, A.M., Mohamad, A.B., Kadhum, A.A.H., Sopian, K., and Karim, N.S.A. “Review on the Development of Natural Dye Photosensitizer for Dye-Sensitized Solar Cells”. *Renewable and Sustainable Energy Reviews,* 31: 386–96, 2014.

Lund, H. “Renewable Energy Strategies for Sustainable Development”. *Energy*, 32 (6): 912–19, 2007.

Lund, J.W., Freeston, D.H., and Boyd, T.L. “Direct Application of Geothermal Energy: 2005 Worldwide Review”. *Geothermics,* 34 (6): 691–727, 2005.

Luther, B.P, Wolter, S.D., and Mohney, S.E. “High Temperature Pt Schottky Diode Gas Sensors on n-Type GaN.” *Sensors and Actuators B: Chemical* 56 : 164–168, 1999.

Ma, Y., Nie, X., Northwood, D.O., and Hu, H. “Systematic Study of the Electrolytic Plasma Oxidation Process on a Mg Alloy for Corrosion Protection”. *Thin Solid Films,* 494 (1-2): 296–301, 2006.

Maffei, N., and Kuriakose, A.K. “A Solid-State Potentiometric Sensor for Hydrogen Detection in Air.” *Sensors and Actuators B: Chemical* 98 : 73–76, 2004.

Mahan, G. D., Sofo, J.O., and Bartkowiak, M. “Multilayer Thermionic Refrigerator and Generator”. *Journal of Applied Physics,* 83 (9): 4683, 1998.

Makki, A., Omer, S., and Sabir, H. “Advancements in Hybrid Photovoltaic Systems for Enhanced Solar Cells Performance”. *Renewable and Sustainable Energy Reviews,* 41: 658–84, 2015.

Matsumoto, Y., Ishikawa, Y., Nishida, M., and Ii, S. “A New Electrochemical Method to Prepare Mesoporous Titanium(IV) Oxide Photocatalyst Fixed on Alumite Substrate”. *The Journal of Physical Chemistry B,* 104: 4204–9, 2000.

Matthews, R.W. “Kinetics of Photocatalytic Oxidation of Organic Titanium Dioxide Solutes over”. *Journal of Ctalysis,* 111: 264–72, 1988.

Mildner, B., Hasselbrink, E., and Diesing, D. “Electronic Excitations Induced by Surface Reactions of H and D on Gold”. *Chemical Physics Letters,* 432 (1-3): 133–38. 2006.

Miller, J.A, and Bowman, C.T. “Mechanism and Modeling of Nitrogen Chemistry in Combustion”. *Progress in Energy and Combustion Science*, 15(4): 4287–338, 1989.

Miller, K., Nalwa, K.S., Bergerud, A., Neihart, N.M., and Chaudhary, S. “Memristive Behavior in Thin Anodic Titania”. *IEEE Electron Device Letters,* 31 (7): 737–39, 2010.

Minh, N.Q. “Technological Status of Nickel Oxide Cathodes in Molten Carbonate Fuel Cells - A Review”. *Journal of Power Sources*, 24: 1–19, 1988.

Moon, J., Kemell, M., Kukkola, J., Punkkinen, R., Hedman, H.P., Suominen, A., Mäkilä, E., Tenho, M., Tuominen, A., and Kim, H. “Gas Sensor Using Anodic TiO_2 Thin Film for Monitoring Hydrogen.” *Procedia Engineering* 47: 791–94, 2012.

Mouaddib, N., Feumi-Jantou, C., Garbowski, E. and Primet, M. “Catalytic Oxidation of Methane over Palladium Supported on Alumina: Influence of the Oxygen-to Methane Ratio”. *Applied Catalysis A*, 87: 129–144, 1992.

Muggli, D.S., and Ding, L. “Photocatalytic Performance of Sulfated TiO_2 and Degussa P-25 TiO_2 during Oxidation of Organics”. *Applied Catalysis B: Environmental,* 32: 181–94, 2001.

Murakami, M., Matsumoto, Y., Nakajima, K., Makino, T., Segawa, Y., Chikyow, T., Ahmet, P., Kawasaki, M., and Koinuma, H. “Anatase TiO_2 Thin Films Grown on Lattice-Matched $LaAlO_3$ Substrate by Laser Molecular-Beam Epitaxy”. *Applied Physics Letter,s* 78 (18): 2664, 2001.

Nedrygailov, I.I., Hasselbrink, E., Diesing, D., Dasari, S.K., Hashemian, M.A., and Karpov, E.G. “Noninvasive Measurement and Control of the Temperature of Pt Nanofilms on Si Supports”. *Journal of Vacuum Science & Technology A: Vacuum, Surfaces, and Films,* 30 (3): 030601, 2012.

Nedrygailov., I.I., and Karpov, E.G. “Pd/n-SiC Nanofilm Sensor for Molecular Hydrogen Detection in Oxygen Atmosphere.” *Sensors and Actuators B: Chemical* 148 : 388–91, 2010.

Ni, M., Leung, M.K.H., Leung, D.Y.C., and Sumathy, K. “A Review and Recent Developments in Photocatalytic Water-Splitting Using TiO_2 for Hydrogen Production”. *Renewable and Sustainable Energy Reviews,* 11 (3): 401–25, 2007.

Nian, Y., Strozier, J., Wu, N., Chen, X., and Ignatiev, A. “Evidence for an Oxygen Diffusion Model for the Electric Pulse Induced Resistance Change Effect in Transition-Metal Oxides”. *Physical Review Letters,* 98 (14): 146403, 2007.

Nienhaus, H., Gergen, B., Weinberg, W.H., and McFarland, E.W. “Detection of Chemically Induced Hot Charge Carriers with Ultrathin Metal Film Schottky Contacts”. *Surface Science,* 514 (1-3): 172–81, 2002.

Nienhaus, H. “Electronic Excitations by Chemical Reactions on Metal Surfaces”. *Surface Science Reports,* 45 (1-2): 1–78, 2002.

Nienhaus, H., Bergh, H.S., Gergen, B., Majumdar, A., Weinberg, W.H., and McFarland, E.W. “Selective H Atom Sensors Using Ultrathin Ag/Si Schottky Diodes.” *Applied Physics Letters* 74 (26): 4046, 1999.

Oh, S.H., Mitchell, P.J, and Siewert, R.M. “Methane Oxidation over Noble Metal Catalysts as Related to Controlling Natural Gas Vehicle Exhaust Emissions”. *Catalytic Control of Air Pollution: Mobile and Stationary Sources,* Silver, R.G, Sawyer, J.E and Summers, J.C., Eds.; Vol. 495, pp. 12–25, 1992.

Ohno, T., Sarukawa, K., Tokieda, K., and Matsumura, M. “Morphology of a TiO_2 Photocatalyst (Degussa, P-25) Consisting of Anatase and Rutile Crystalline Phases”. *Journal of Catalysis,* 203 (1): 82–86, 2001.

Ong, C.K., and Wang, S.J. “In Situ RHEED Monitor of the Growth of Epitaxial Anatase TiO_2 Thin Films”. *Applies Surface Science,* 185: 47–51, 2001.

Ormerod, R.M. “Solid Oxide Fuel Cells”. *Chemical Society Reviews,* 32 (1): 17–28, 2003.

Pala, R.A., White, J., Barnard, E., Liu, J., and Brongersma, M.L. “Design of Plasmonic Thin-Film Solar Cells with Broadband Absorption Enhancements”. *Advanced Materials,* 21 (34): 3504–9, 2009.

Pan, Z., Zhao, K., Wang, J., Zhang, H., Feng, Y., and Zhong, X. “Near Infrared Absorption of $CdSe_xTe_{1-x}$ Alloyed Quantum Dot Sensitized Solar Cells with More than 6% Efficiency and High Stability”. *ACS Nano,* 6: 5215–22, 2013.

Park, J.Y., Renzas, J.R., Hsu, B.B., and Somorjai, G.A. “Interfacial and Chemical Properties of Pt/TiO_2 , Pd/TiO_2 , and Pt/GaN Catalytic Nanodiodes Influencing Hot Electron Flow”. *Journal of Physical Chemistry C,* 111: 15331–36, 2007.

Park, J.Y., and Somorjai, G.A. “The Catalytic Nanodiode: Detecting Continuous Electron Flow at Oxide-Metal Interfaces Generated by a Gas-Phase Exothermic Reaction”. *A European Journal of Chemical Physics and Physical Chemistry*, 7 (7): 1409–13, 2006.

Park, S.J. “Chemical Observation of Anodic TiO_2 for Biomaterial Application.” *Metals and Materials International* 14 (4): 449–55, 2008.

Park, Y.K, Bui, P., and Vlachos, D.G. “Operation Regimes in Catalytic Combustion: H_2/Air Mixtures near Pt”. *AIChE Journal,* 44 (9): 2035–43, 1998.

Pavlov, B.V., and Qiao, L. “Catalytic Oxidation of Methanol on Platinum Nanoparticles”. *Spring Technical Meeting of the Central States Section of the Combustion Institute April 22–24*, 2012.

Pazheri, F.R., Othman, M.F., and Malik, N.H. “A Review on Global Renewable Electricity Scenario”, *Renewable and Sustainable Energy Reviews,* 31: 835–45, 2014.

Pedraza, F., and Vazquez, A. “Obtention of TiO_2 Rutile at Room Temperature through Direct Oxidation of $TiCl_3$”. *Journal of Physics and Chemistry of Solids,* 60: 445–48, 1999.

Persson, K., Ersson, A., Colussi, S., Trovarelli, A., and Järås, S.G. “Catalytic Combustion of Methane over Bimetallic Pd–Pt Catalysts: The Influence of Support Materials”. *Applied Catalysis B: Environmental,* 66 (3-4): 175–85, 2006.

Poznyak, S.K., Kokorin, A.I., and Kulak, A.I. “Effect of Electron and Hole Acceptors on the Photoelectrochemical Behaviour of Nanocrystalline Microporous TiO_2 Electrodes”. *Journal of Electroanalytical Chemistry,* 442: 99–105, 1998.

Rahbarpour, S., and Hosseini-Golgoo, S.M. “Diode Type Ag–TiO_2 Hydrogen Sensors.” *Sensors and Actuators B: Chemical* 187 : 262–66, 2013.

Rinnemo, M., Deutschmann, O., Behrendt, F., and Kasemo, B. “Experimental and Numerical Investigation of the Catalytic Ignition of Mixtures of Hydrogen and Oxygen on Platinum”. *Combustion and Flame,* 111 (4): 312–26, 1997.

Robinett, W., Pickett, M., Borghetti, J., Xia, Q., Snider, G.S., Medeiros-Ribeiro, G., and Williams, R.S. “A Memristor-Based Nonvolatile Latch Circuit”. *Nanotechnology,* 21 (23): 235203, 2010.

Roland, U., Braunschweig, T., and Roessner, F. “On the Nature of Spilt-over Hydrogen”. *Journal of Molecular Catalysis A: Chemical,* 127 (1–3): 61–84, 1997.

Roy, S., Jacob, C., and Basu, S. “Studies on Pd/3C-SiC Schottky Junction Hydrogen Sensors at High Temperature.” *Sensors and Actuators B: Chemical* 94 : 298–303, 2003.

Rumiche, F., Wang, H.H., Hu, W.S., Indacochea, J.E., Wang, M.L. "Anodized Aluminum Oxide (AAO) Nanowall Sensors for Hydrogen Detection". *Sensors and Actuators B* 134: 869-878, 2008.

Sammes, N., Phillips, R., and Smirnova, A. “Proton Conductivity in Stoichiometric and Sub-Stoichiometric Yittrium Doped $SrCeO_3$ Ceramic Electrolytes”. *Journal of Power Sources,* 134 (2): 153–59, 2004.

Scaccia, S. “Investigation on NiO Solubility in Binary and Ternary Molten Alkali Metal Carbonates Containing Additives”. *Journal of Molecular Liquids,* 116 (2): 67–71, 2005.

Schierbaum, K., and Achhab, M.E. “Generation of an Electromotive Force by Hydrogen-to–Water Oxidation with Pt–Coated Oxidized Titanium Foils”. *Physica Status Solidi A* 208 (12): 2796–2802, 2011.

Schindler, B., Diesing, D., and Hasselbrink, E. “Electronic Excitations in the Course of the Reaction of H with Coinage and Noble Metal Surfaces: A Comparison”. *The Journal of Physical Chemistry C,* 117: 6337−6345, 2013.

Sclafani, A., Palmisano, L., and Schiavello, M. “Influence of the Preparation Methods of TiO_2 on the Photocatalytic Degradation of Phenol in Aqueous Dispersion”. *Journal of Physics and Chemistry*, 94: 829–32, 1990.

Sedona, F., Rizzi, G.A., Agnoli, S., Llabres i Xamena, F.X., Papageoriou, A., Ostermann, D., Sambi, M., Finetti, P., Schierbaum, K., Granozzi, G. “Ultrathin TiO_2 Films on Pt(111): A LEED, XPS, and STM Investigation”. *The Journal of Physical Chemistry B,* 109(51): 24411–26, 2005.

Şennik, E., Çolak, Z., Kılınç, N., and Öztürk, Z.Z. “Synthesis of Highly-Ordered TiO_2 Nanotubes for a Hydrogen Sensor.” *International Journal of Hydrogen Energy* 35 : 4420–27, 2010.

Shah, A.V., Schade, H., Vanecek, M., Meier, J., Vallat-Sauvain, E., Wyrsch, N., Kroll, U., Droz, C., and Bailat, J. “Thin-Film Silicon Solar Cell Technology”. *Progress in Photovoltaics: Research and Applications,* 12 (23): 113–42, 2004.

Shalav, A., Richards, B.S., and Green, M.A. “Luminescent Layers for Enhanced Silicon Solar Cell Performance: Up-Conversion”. *Solar Energy Materials and Solar Cells,* 91 (9): 829–42, 2007.

Shimizu, Y., Hyodo, T., and Egashira, M. “H_2 Sensing Performance of Anodically Oxidized TiO_2 Thin Films Equipped with Pd Electrode”. *Sensors and Actuators B: Chemical*,121 (1): 219–30, 2007.

Sikora, M.D.S., Rosario, A.V., Pereira, E.C., and Paiva-Santos, C. “Influence of the Morphology and Microstructure on the Photocatalytic Properties of Titanium Oxide Films Obtained by Sparking Anodization in H_3PO_4”. *Electrochimica Acta,* 56 (9): 3122–27, 2011.

Snaith, H.J. “Perovskites: The Emergence of a New Era for Low-Cost , High Efficiency Solar Cells”. *The Journal of Physical Chemistry Letters,* 4: 3623–3630, 2013.

Snizhko, L.O., Yerokhin, A.L., Pilkington, A., Gurevina, N.L., Misnyankin, D.O., Leyland, A., and Matthews, A. “Anodic Processes in Plasma Electrolytic Oxidation of Aluminium in Alkaline Solutions”. *Electrochimica Acta,* 49 (13): 2085–95, 2004.

Snyder, G.J. “Small Thermoelectric Generators,”. *The Electrochemical Society Interface*, 54–56, 2008.

Snyder, G.J., and Toberer, E.S. “Complex Thermoelectric Materials”. *Nature Materials,* 7: 105–14, 2008.

Sofo, J.O; Mahan, G. “Optimum Band”. *Physical Review B,* 49 (7): 4565–4570, 1994.

Song, J., Lu, W., Flynn, J.S., and Brandes, G.R. “AlGaN/GaN Schottky Diode Hydrogen Sensor Performance at High Temperatures with Different Catalytic Metals.” *Solid-State Electronics* 49 : 1330–34, 2005.

Stella, K., Kovacs, D.A., Diesing, D., Brezna, W., and Smoliner, J. “Charge Transport Through Thin Amorphous Titanium and Tantalum Oxide Layers”. *Journal of The Electrochemical Society,* 158 (5): P65, 2011.

Stewart, D.R., Ohlberg, D.A.A., Beck, P.A., Chen, Y., and Williams, R.S. “Molecule-Independent Electrical Switching in Pt/Organic Monolayer/Ti Devices”. *Nano Letters*, 4(1): 133–136, 2004.

Strukov, D.B., Snider, G.S., Stewart, D.R., and Williams, R.S. “The Missing Memristor Found”. *Nature,* 453 (7191): 80–83, 2008.

Subramanian, V., Wolf, E., and Kamat, P.V. “Semiconductor - Metal Composite Nanostructures . To What Extent Do Metal Nanoparticles Improve the Photocatalytic Activity of TiO_2 Films?”. *Journal of Physical Chemistry B,* 105: 11439–46, 2001.

Sul, Y.T., Johansson, C.B., Petronis, S., Krozer, A., Wennerberg, A., and Albrektsson, T. “Characteristics of the Surface Oxides on Turned and Electrochemically Oxidized Pure Titanium Implants up to Dielectric Breakdown: The Oxide Thickness , Micropore Configurations , Surface Roughness , Crystal Structure and Chemical Composition”. *Biomaterials*, 23: 491–501, 2002.

Takeuchi, M., Yamashita, H., Matsuoka, M., Anpo, M., Hirao, T., and Itoh, N. “Photocatalytic Decomposition of NO under Visible Light Irradiation on the Cr-Ion-Implanted TiO_2 Thin Film Photocatalyst”. *Catalysis Letters,* 67: 135–37, 2000.

Tanaka, K., Capule, M.F.V., and Hisanaga, T. “Effect of Crystallinity of TiO_2 on its Photocatalytic Action”. *Chemical Physics Letters,* 187 (1-2): 73-76, 1991.

Thevenin, P. “Catalytic Combustion of Methane over Cerium-Doped Palladium Catalysts”, *Journal of Catalysis,* 215 (1): 78–86, 2003.

Thiruvenkatachari, R., Vigneswaran, S., and Moon, I.S. “A Review on UV/TiO_2 Photocatalytic Oxidation Process”. *The Korean Journal of Chemical Engineering,* 25 (1): 64–72, 2008.

Thompson, T.L., and Yates, J.T. “Surface Science Studies of the Photoactivation of TiO_2 New Photochemical Processes”. *Chemical Reviews,* 106: 4428–53, 2006.

Tomczyk, P. “MCFC versus Other Fuel Cells–characteristics, Technologies and Prospects”. *Journal of Power Sources*, 160 (2): 858–62, 2006.

Trimm, D.L. “Catalytic Combustion (Review)”. *Applied Catalysis,* 7: 249–82, 1983.

Trimm, D.L, and Lam, C.-W. “The Combustion of Methane on Platinum-alumina Fibre Catalysts–I”. *Chemical Engineering Science*, 35: 1405–1413, 1980.

Tsai, T.H., Huang, J.R., Lin, K.W., Hsu, W.C., Chen, H.I.,and Liu, W.C. “Hydrogen Sensors with Double Dipole Layers Using a Pd-Mixture-Pd Triple-Layer Sensing Structure.” *Sensors and Actuators B: Chemical* 141 : 532–37, 2008.

Varghese, O.K., Gong, D., Paulose, M., Ong, K.G., Dickey, E.C., and Grimes, C.A. “Extreme Changes in the Electrical Resistance of Titania Nanotubes with Hydrogen Exposure”. *Advanced Materials,* 15 (78): 624–27, 2003.

Vineyard, G.H. “Frequency Factors and Isotope Effects in Solid State Rate Processes”. *Journal of Physics and Chemistry of Solids* 3: 121−27, 1957.

Vlachos, D.G., and Bui, P.A. “Catalytic Ignition and Extinction of Hydrogen: Comparison of Simulations and Experiments”. Surface Science, 364: 625–630, 1996.

Voter, A. F., and Doll, J.D. “Dynamical Corrections to Transition State Theory for Multistate Systems: Surface Self-Diffusion in the Rare-Event Regime.” *The Journal of Chemical Physics* 82: 80−92, 1985.

Wang, C., Yin, L., Zhang, L., Xiang, D., and Gao, R. “Metal Oxide Gas Sensors: Sensitivity and Influencing Factors.” *Sensors* 10: 2088–2106, 2010.

Wang, T., Luan, W., Wang, W., and Tu, S.T. “Waste Heat Recovery through Plate Heat Exchanger Based Thermoelectric Generator System”. *Applied Energy,* 136: 860–65, 2014.

Wang, Y., Chen, K.S., Mishler, J., Cho, S.H., and Adroher, X.C. “A Review of Polymer Electrolyte Membrane Fuel Cells: Technology, Applications, and Needs on Fundamental Research”. *Applied Energy,* 88 (4): 981–1007, 2011.

Waser, R., and Aono, M. “Nanoionics-Based Resistive Switching Memories”. *Nature Materials,* 6 (11): 833–40, 2007.

Whitlow, L.W., and Hirano, T. “Superlattice Applications to Thermoelectricity”. *Journal of Applied Physics,* 78 (9): 5460, 1995.

Wigner, E. “The Transition State Method ”. *Transactions of the Faraday Society*, 34: 29−41, 1938.

Wilke, K., and Breuer, H.D. “The Influence of Transition Metal Doping on the Physical and Photocatalytic Properties of Titania”. *Journal of Photochemistry and Photobiology A: Chemistry,* 121: 49–53, 1999.

Williams, W. R., Marks, M., and Schmidt, D.L. “Steps in the Reaction $H_2 + O_2 = H_2O$ on Pt: OH Desorption at High Temperatures”. *Journal of Physical Chemistry,* 96: 5922–31, 1992.

Winter, M., and Brodd, R.J. “What Are Batteries , Fuel Cells , and Supercapacitors?”. *Chemical Reviews,* 104: 4245–4269, 2004.

Wintterlin, J., Trost, J., Renisch, S., Schuster, R., Zambelli, T., and Ertl, G. “Real-Time STM Observations of Atomic Equilibrium Fluctuations in an Adsorbate System: O/Ru(0001).” *Surface Science* 394 (1–3): 159–69, 1997.

Wold, A. “Photocatalytic Properties of TiO_2”. *Chemistry of Materials,* 5 (3): 280–283, 1993.

Wu, J., and McCreery, R.L. “Solid-State Electrochemistry in Molecule/TiO_2 Molecular Heterojunctions as the Basis of the TiO_2‘Memristor’”. *Journal of The Electrochemical Society* 156 : 29−37, 2009.

Xuan, X.C., and Li, D. “Optimization of a Combined Thermionic–thermoelectric Generator”. *Journal of Power Sources,* 115 (1): 167–70, 2003.

Y, L., Wu, G.S., Yuan, X.Y., Xie, T., and Zhang, L.D. 2003. “Fabrication and Optical Properties of TiO_2 Nanowire Arrays Made by Sol – Gel Electrophoresis Deposition into Anodic Alumina Membranes”. *Journal of Physics: Condensed Matter,*15: 2917–22, 2003.

Yam, F.K., and Hassan, Z. “Schottky Diode Based on Porous GaN for Hydrogen Gas Sensing Application.” *Applied Surface Science* 253 : 9525–28, 2007.

Yamashita, H., Harada, M., Misaka, J., Takeuchi, M., Ikeue, K., and Anpo, M. “Degradation of Propanol Diluted in Water under Visible Light Irradiation Using Metal Ion-Implanted Titanium Dioxide Photocatalysts”. *Journal of Photochemistry and Photobiology A: Chemistry,* 148 (1-3): 257–61, 2002.

Yang, J.J., Pickett, M.D., Li, X., Ohlberg, D.A.A., Stewart, D.R., and Williams, R.S. “Memristive Switching Mechanism for Metal/oxide/metal Nanodevices”. *Nature Nanotechnology*, 3 (7): 429–33, 2008.

Yang, S., Nair, A.S., and Ramakrishna, S. “Conversion Efficiency Enhancement of CdS Quantum Dot-Sensitized Electrospun Nanostructured TiO_2 Solar Cells by Organic Dipole Treatment”. *Materials Letters,* 116: 345–48, 2014.

Yang, S., Maroto-valiente, A., Benito-gonzalez, M., and Rodriguez-ramos, I. “Methane Combustion over Supported Palladium Catalysts I . Reactivity and Active Phase”. *Applied Catalysis B: Environmental,* 28: 223–33, 2000.

Yerokhin, A.L., Nie, X., Leyland, A., Matthews, A., and Dowey, S.J. “Plasma Electrolysis for Surface Engineering”. *Surface and Coatings Technology,* 122 (2-3): 73–93, 1999.

Zalvidea, D., Díez, A., Cruz, J.L., and Andrés, M.V. “Hydrogen Sensor Based on a Palladium-Coated Fibre-Taper with Improved Time-Response.” *Sensors and Actuators B: Chemical* 114 : 268–74, 2006.

Zdansky, K., and Yatskiv, R. “Schottky Barriers on InP and GaN Made by Deposition of Colloidal Graphite and Pd, Pt or Bimetal Pd/Pt Nanoparticles for H_2-Gas Detection.” *Sensors and Actuators B: Chemical* 165 : 104–109, 2012.

Zeng, G., Bowers, J.E., Zide, J.M.O., Gossard, A.C., Kim, W., Singer, S., Majumdar, A., Singh, R., Bian, Z., Zhang, Y., and Shakouri, A. “ErAs: InGaAs/InGaAlAs Superlattice Thin-Film Power Generator Array”. *Applied Physics Letters,* 88 (11): 113502, 2006.

Zhang, Z., and Yates, J.T. “Band Bending in Semiconductors: Chemical and Physical Consequences at Surfaces and Interfaces.” *Chemical Reviews* 112 (10): 5520–51, 2012.

APPENDIX

Title:	Chemistry-Driven Signal Transduction in a Mesoporous Pt/TiO2 System
Author:	Eduard G. Karpov, Mohammad A. Hashemian, Suhas K. Dasari
Publication:	The Journal of Physical Chemistry C
Publisher:	American Chemical Society
Date:	Aug 1, 2013

PERMISSION/LICENSE IS GRANTED FOR YOUR ORDER AT NO CHARGE

This type of permission/license, instead of the standard Terms & Conditions, is sent to you because no fee is being charged for your order. Please note the following:

- Permission is granted for your request in both print and electronic formats, and translations.
- If figures and/or tables were requested, they may be adapted or used in part.
- Please print this page for your records and send a copy of it to your publisher/graduate school.
- Appropriate credit for the requested material should be given as follows: "Reprinted (adapted) with permission from (COMPLETE REFERENCE CITATION). Copyright (YEAR) American Chemical Society." Insert appropriate information in place of the capitalized words.
- One-time permission is granted only for the use specified in your request. No additional uses are granted (such as derivative works or other editions). For any other uses, please submit a new request.

ELSEVIER LICENSE
TERMS AND CONDITIONS

Jun 18, 2015

This is an Agreement between Mohammad Amin Hashemian ("You") and Elsevier ("Elsevier"). It consists of your order details, the terms and conditions provided by Elsevier, and the payment terms and conditions.

All payments must be made in full to CCC. For payment instructions, please see information listed at the bottom of this form.

Supplier	Elsevier Limited The Boulevard,Langford Lane Kidlington,Oxford,OX5 1GB,UK
Registered Company Number	1982084
Customer name	Mohammad Amin Hashemian
Customer address	4250 N marine dr CHICAGO, IL 60613
License number	3652030622261
License date	Jun 18, 2015
Licensed content publisher	Elsevier
Licensed content publication	Materials Chemistry and Physics
Licensed content title	Hydrogen sensing behavior of Pt-coated mesoporous anodic titania
Licensed content author	Mohammad A. Hashemian,Eduard G. Karpov
Licensed content date	15 December 2014
Licensed content volume number	148
Licensed content issue number	3
Number of pages	6
Start Page	579
End Page	584
Type of Use	reuse in a thesis/dissertation
Portion	full article
Format	both print and electronic
Are you the author of this Elsevier article?	Yes
Will you be translating?	No
Title of your thesis/dissertation	Reaction Current Phenomenon in Bifunctional Catalytic Metal-Semiconductor Nanostructures
Expected completion date	Nov 2015
Estimated size (number of pages)	200
Elsevier VAT number	GB 494 6272 12
Price	0.00 USD
VAT/Local Sales Tax	0.00 USD / 0.00 GBP

Total **0.00 USD**

Terms and Conditions

INTRODUCTION

1. The publisher for this copyrighted material is Elsevier. By clicking "accept" in connection with completing this licensing transaction, you agree that the following terms and conditions apply to this transaction (along with the Billing and Payment terms and conditions established by Copyright Clearance Center, Inc. ("CCC"), at the time that you opened your Rightslink account and that are available at any time at http://myaccount.copyright.com).

GENERAL TERMS

2. Elsevier hereby grants you permission to reproduce the aforementioned material subject to the terms and conditions indicated.

3. Acknowledgement: If any part of the material to be used (for example, figures) has appeared in our publication with credit or acknowledgement to another source, permission must also be sought from that source. If such permission is not obtained then that material may not be included in your publication/copies. Suitable acknowledgement to the source must be made, either as a footnote or in a reference list at the end of your publication, as follows:
"Reprinted from Publication title, Vol /edition number, Author(s), Title of article / title of chapter, Pages No., Copyright (Year), with permission from Elsevier [OR APPLICABLE SOCIETY COPYRIGHT OWNER]." Also Lancet special credit - "Reprinted from The Lancet, Vol. number, Author(s), Title of article, Pages No., Copyright (Year), with permission from Elsevier."

4. Reproduction of this material is confined to the purpose and/or media for which permission is hereby given.

5. Altering/Modifying Material: Not Permitted. However figures and illustrations may be altered/adapted minimally to serve your work. Any other abbreviations, additions, deletions and/or any other alterations shall be made only with prior written authorization of Elsevier Ltd. (Please contact Elsevier at permissions@elsevier.com)

6. If the permission fee for the requested use of our material is waived in this instance, please be advised that your future requests for Elsevier materials may attract a fee.

7. Reservation of Rights: Publisher reserves all rights not specifically granted in the combination of (i) the license details provided by you and accepted in the course of this licensing transaction, (ii) these terms and conditions and (iii) CCC's Billing and Payment terms and conditions.

8. License Contingent Upon Payment: While you may exercise the rights licensed immediately upon issuance of the license at the end of the licensing process for the transaction, provided that you have disclosed complete and accurate details of your proposed use, no license is finally effective unless and until full payment is received from you (either by publisher or by CCC) as provided in CCC's Billing and Payment terms and conditions. If full payment is not received on a timely basis, then any license preliminarily granted shall be deemed automatically revoked and shall be void as if never granted. Further, in the event that you breach any of these terms and conditions or any of CCC's Billing and Payment terms and conditions, the license is automatically revoked and shall be void as if never granted. Use of materials as described in a revoked license, as well as any use of the materials beyond the scope of an unrevoked license, may constitute copyright infringement and publisher reserves the right to take any and all action to protect its copyright in the materials.

9. Warranties: Publisher makes no representations or warranties with respect to the licensed material.

10. Indemnity: You hereby indemnify and agree to hold harmless publisher and CCC, and their respective officers, directors, employees and agents, from and against any and all claims arising out of your use of the licensed material other than as specifically authorized pursuant to this license.

11. No Transfer of License: This license is personal to you and may not be sublicensed, assigned, or transferred by you to any other person without publisher's written permission.

12. No Amendment Except in Writing: This license may not be amended except in a writing signed by both parties (or, in the case of publisher, by CCC on publisher's behalf).

13. Objection to Contrary Terms: Publisher hereby objects to any terms contained in any purchase order, acknowledgment, check endorsement or other writing prepared by you, which terms are inconsistent with these terms and conditions or CCC's Billing and Payment terms and conditions. These terms and conditions, together with CCC's Billing and Payment terms and conditions (which are incorporated herein), comprise the entire agreement between you and publisher (and CCC) concerning this licensing transaction. In the event of any conflict between your obligations established by these terms and conditions and those established by CCC's Billing and Payment terms and conditions, these terms and conditions shall control.

14. Revocation: Elsevier or Copyright Clearance Center may deny the permissions described in this License at their sole discretion, for any reason or no reason, with a full refund payable to you. Notice of such denial will be made using the contact information provided by you. Failure to receive such notice will not alter or invalidate the denial. In no event will Elsevier or Copyright Clearance Center be responsible or liable for any costs, expenses or damage incurred by you as a

result of a denial of your permission request, other than a refund of the amount(s) paid by you to Elsevier and/or Copyright Clearance Center for denied permissions.

LIMITED LICENSE

The following terms and conditions apply only to specific license types:

15. **Translation**: This permission is granted for non-exclusive world **English** rights only unless your license was granted for translation rights. If you licensed translation rights you may only translate this content into the languages you requested. A professional translator must perform all translations and reproduce the content word for word preserving the integrity of the article. If this license is to re-use 1 or 2 figures then permission is granted for non-exclusive world rights in all languages.

16. **Posting licensed content on any Website**: The following terms and conditions apply as follows: Licensing material from an Elsevier journal: All content posted to the web site must maintain the copyright information line on the bottom of each image; A hyper-text must be included to the Homepage of the journal from which you are licensing at http://www.sciencedirect.com/science/journal/xxxxx or the Elsevier homepage for books at http://www.elsevier.com; Central Storage: This license does not include permission for a scanned version of the material to be stored in a central repository such as that provided by Heron/XanEdu.

Licensing material from an Elsevier book: A hyper-text link must be included to the Elsevier homepage at http://www.elsevier.com . All content posted to the web site must maintain the copyright information line on the bottom of each image.

Posting licensed content on Electronic reserve: In addition to the above the following clauses are applicable: The web site must be password-protected and made available only to bona fide students registered on a relevant course. This permission is granted for 1 year only. You may obtain a new license for future website posting.

17. **For journal authors**: the following clauses are applicable in addition to the above:

Preprints:

A preprint is an author's own write-up of research results and analysis, it has not been peer-reviewed, nor has it had any other value added to it by a publisher (such as formatting, copyright, technical enhancement etc.).

Authors can share their preprints anywhere at any time. Preprints should not be added to or enhanced in any way in order to appear more like, or to substitute for, the final versions of articles however authors can update their preprints on arXiv or RePEc with their Accepted Author Manuscript (see below).

If accepted for publication, we encourage authors to link from the preprint to their formal publication via its DOI. Millions of researchers have access to the formal publications on ScienceDirect, and so links will help users to find, access, cite and use the best available version. Please note that Cell Press, The Lancet and some society-owned have different preprint policies. Information on these policies is available on the journal homepage.

Accepted Author Manuscripts: An accepted author manuscript is the manuscript of an article that has been accepted for publication and which typically includes author-incorporated changes suggested during submission, peer review and editor-author communications.

Authors can share their accepted author manuscript:

- immediately
  - via their non-commercial person homepage or blog
  - by updating a preprint in arXiv or RePEc with the accepted manuscript
  - via their research institute or institutional repository for internal institutional uses or as part of an invitation-only research collaboration work-group
  - directly by providing copies to their students or to research collaborators for their personal use
  - for private scholarly sharing as part of an invitation-only work group on commercial sites with which Elsevier has an agreement
- after the embargo period
  - via non-commercial hosting platforms such as their institutional repository
  - via commercial sites with which Elsevier has an agreement

In all cases accepted manuscripts should:

- link to the formal publication via its DOI
- bear a CC-BY-NC-ND license - this is easy to do
- if aggregated with other manuscripts, for example in a repository or other site, be shared in alignment with our hosting policy not be added to or enhanced in any way to appear more like, or to substitute for, the published journal article.

VITA

NAME: Mohammad Amin Hashemian

EDUCATION:

Ph.D., Materials Engineering, University of Illinois at Chicago, Chicago, Illinois, 2015.

B.S., Chemical Engineering, Sharif University of Technology, Tehran, Iran, 2009.

HONOR: Graduate Research Assistant, University of Illinois at Chicago, Chicago, Illinois, 2011-2015.

TEACHING EXPERIENCE:

Teaching assistant, Spring 2011- Fall 2015

- Statics
- Materials for Manufacturing
- Properties of Materials
- Finite Element Analysis
- Strength of Materials

JOURNAL PUBLICATIONS:

Nedrygailov, I.I., Diesing, D., Hasselbrink, E., Dasari, S.K., **Hashemian, M.A.**, and Karpov, E.G. "Non-invasive measurement and control of the temperature of Pt nanofilms on Si supports". *Journal of Vacuum Science & Technology A*, 30(3): 030601, 2012.

Dasari, S.K., **Hashemian, M.A.**, Mohan, J., and Karpov, E.G. "A Nonthermal Chemicurrent Effect of Hydrogen Adsorption on Pt/SiC Planar Nanostructures at Normal Ambient Conditions". *Chemical Physics Letters*, 553: 47-50, 2012.

Hashemian, M.A., Dasari, S.K., and Karpov, E.G. "Separation of Hot Electron Current Component Induced by Hydrogen Oxidation on Resistively Heated Pt/n-GaP Planar Schottky Nanostructures". *Journal of Vacuum Science and Technology A*, 31(2): 020603, 2013.

Karpov, E.G., **Hashemian, M.A.**, and Dasari, S.K. "Chemistry-Driven Signal Transduction in a Mesoporous Pt/TiO2 System". *Journal of Physical Chemistry C*, 117 (30): 15632–15638, 2013.

Hashemian, M.A., Palacios, E., Nedrygailov, I.I., Diesing, D., and Karpov, E.G. "Thermal Properties of the Stationary Current in Mesoporous Pt/TiO_2 Structures in an Oxyhydrogen Atmosphere". *ACS Applied Materials & Interfaces*, 5 (23): 12375–12379, 2013.

Hashemian, M.A., and Karpov, E.G. "Hydrogen Sensing Behavior of Pt-coated Mesoporous Anodic Titania". *Materials Chemistry and Physics*, 148(3): 579-584, 2014.

Ray N.J, **Hashemian M.A**, and Karpov E.G. "Stationary Chemicurrent Effect in Mesoporous Pt/ZrO_2 System Under H_2/O_2 Environment: Influence of Substrate Morphology". *ACS Applied Materials and Interfaces,* 2015 (under review).

CONFERENCE PUBLICATIONS AND PRESENTATIONS:

Hashemian, M.A., Karpov, E.G. Energy Conversion Processes in Catalytic Electrolyte-Free Metal-Oxide Nanostructures. *Proceedings of The 227th ECS Meeting*, May 24-28, 2015, Chicago, IL.

Hashemian, M.A., Ray, N., Karpov, E.G. Thermal Properties of Stationary Reaction Currents in Mesoporous Pt/TiO2 Structures in an Oxyhydrogen Atmosphere. *Proceedings of the ASME 2014 International Mechanical Engineering Congress & Exposition*, November 14-20, 2014, Montreal, Canada

Hashemian, M.A., Ray, N., Karpov, E.G. Chemical Signal Transduction in Pt/TiO2 and Rh/TiO2 Barrier-Layer Nanostructures Based on Mesoporous Titania. *Proceedings of the ASME 2014 International Mechanical Engineering Congress & Exposition*, November 14-20, 2014, Montreal, Canada

Hashemian, M.A., Karpov, E.G. Hydrogen Sensing Behavior of Pt-coated Mesoporous Titania: Effect of Voltage Bias and Reference Atmosphere. *ASM Chicago Regional Chapter Meeting,* April 8, 2014, Chicago, IL

Karpov, E.G, **Hashemian, M.A.,** Plakhotnyuk, M.M. Chemovoltaic Effect in Catalytic Metal-Semiconductor Nanostructures. *Proceedings of the ASME 2013 International Mechanical Engineering Congress & Exposition*, November 15-22, 2013, San Diego, CA

Hashemian, M.A., Karpov, E.G., Plakhotnyuk, M.M. Nanometer Thickness Planar Schottky Contacts for Ultra-Fast Sensing and Energy Conversion Applications. *Proceedings of the ASME 2013 International Mechanical Engineering Congress & Exposition*, November 15-22, 2013, San Diego, CA

Plakhotnyuk, M.M., **Hashemian, M.A.,** Karpov, E.G. Surface Morphology And Electrical Characterization Of Metal-Semiconductor Pt-TiO2 Nanostructures. *Proceedings of the ASME 2013 International Mechanical Engineering Congress & Exposition*, November 15-22, 2013, San Diego, CA

Karpov, E.G., **Hashemian, M.A.,** Plakhotnyuk, M.M. Enhanced Chemicurrent Effect of H2 Oxidation on Pt/TiO2/Ti Micro-Nanostructure Surface. *Proceedings of the ASME 2013 International Mechanical Engineering Congress & Exposition*, November 15-22, 2013, San Diego, CA

Hashemian, M.A., Karpov, E.G, Plakhotnyuk, M.M. Micro-Nanostructured Pt/TiO2/Ti System as a Chemical-Electrical Transducer. *Proceedings of the ASME 2013 International Mechanical Engineering Congress & Exposition*, November 15-22, 2013, San Diego, CA

Dasari, S.K., Ariyan, M., **Hashemian, M.A,** Karpov, E.G. Structure-to-Function Relationship in Porous Pt/TiO2/Ti Planar Nanostructures with a Potential Barrier for Chemicurrent Related Applications, Book of Abstracts of *American Vacuum Society 59th International Symposium & Exhibition*, Oct 28 – Nov 2, 2012, Tampa, FL

Hashemian, M.A., Dasari, S.K., Karpov, E.G. Basic Regimes and Reaction Mechanisms of Chemicurrent Generation during H2 Oxidation on Catalytic MIM Nanostructures with Porous TiO2 Support, Book of Abstracts of *American Vacuum Society 59th International Symposium & Exhibition*, Oct 28 – Nov 2, 2012, Tampa, FL

Dasari, S.K, **Hashemian, M.A,** Karpov, E.G. Analysis of Chemicurrent Components Induced by Hydrogen Oxidation on Pt/n-GaP and Pt/n-SiC Planar Schottky Nanostructures, Book of Abstracts of *American Vacuum Society 59th International Symposium & Exhibition*, Oct 28 – Nov 2, 2012, Tampa, FL

Karpov, E.G, **Hashemian, M.A,** Dasari, S.K. Enhanced Chemicurrent Effect of H2 Oxidation on Porous MIM Nanostructures, Book of Abstracts of *American Vacuum Society 59th International Symposium & Exhibition*, Oct 28 – Nov 2, 2012, Tampa, FL

Hashemian, M.A, Dasari, S.K, Karpov, E.G. Electrochemical and Hot-Electron Mechanisms of Current Generation in Porous Pt-Coated Oxidized Metal Foils, Proceedings of *ASME 6th International Conference on Energy Sustainability*, Jul 23-26, 2012, San Diego, CA.

Dasari, S.K, **Hashemian, M.A.,** Karpov, E.G. A Voltaic Effect of Hydrogen to Water Oxidation in Resistively Heated Planar Schottky Nanostructures, Proceedings of *ASME 6th International Conference on Energy Sustainability*, Jul 23-26, 2012, San Diego, CA.

Hashemian, M.A, Dasari, S.K, Karpov, E.G. Low-Temperature Chemovoltaic Effect in Catalytic Metal-Semiconductor Nanostructures, Proceedings of *2012 MRS Spring Meeting*, Apr 9-13, 2012, San Francisco, CA.

Dasari, S.K, **Hashemian, M.A,** Karpov, E.G. Nanometer Thickness Planar Schottky Contacts for Ultra-fast Sensing and Energy Conversion Applications, Proceedings of *2012 MRS Spring Meeting*, Apr 9-13, 2012, San Francisco, CA.

Karpov, E.G., Dasari, S.K., **Hashemian, M.A**. Charge Transfer and Diabatic Dissipation of Surface Released Chemical Energy in GaP/Pt Schottky Nanostructures with a Resistively Heated Nanocathode Layer, Proceedings of *American Vacuum Society 58th International Symposium & Exposition*, Nashville, TN, Oct 30 – Nov 4, 2011.